SPECIFIC ENERGY AND ENERGY DENSITY ANALYSIS OF CONVENTIONAL AND NONCONVENTIONAL FLYWHEELS

A Thesis

by

RUBEN REYNA JR.

Submitted to the Office of Graduate and Professional Studies of
Texas A&M University
in partial fulfillment of the requirements for the degree of

MASTER OF SCIENCE

Chair of Committee,	Alan B. Palazzolo
Co-Chair of Committee,	Shehab Ahmed
Committee Member,	Terry S. Creasy
Head of Department,	Andreas Polycarpou

December 2013

Major Subject: Mechanical Engineering

ABSTRACT

Flywheels are widely used as a means of energy storage throughout different applications such as hybrid electric vehicles, spacecraft, and electrical grids. The research presented here investigates various steel flywheel constructions. The purpose of this research was to increase the energy density of a flywheel by reducing the centrifugal stresses that occur during operation. Various configurations were attempted, with some consisting of metal, composite, or both. This thesis documents the steps taken in determining and analyzing the proposed designs. Increase of the energy storage in metal flywheels is accomplished most efficiently through optimization of the flywheel geometry. Energy storage of the hybrid and composite flywheels shows large room for improvement.

Modeling and simulation of the various systems were conducted with the Finite Element Analysis (FEA) software ANSYS Classic v 13.0. A combination of input files and the GUI was used for the analysis. The results are verified with analytical solutions where applicable. Novel flywheel designs are converged to ensure accurate results.

DEDICATION

To my family and friends.

ACKNOWLEDGEMENTS

I would like to thank my committee chair, Dr. Palazzolo, and my committee members, Dr. Ahmed and Dr. Creasy, for their guidance and support throughout the course of this research. Thanks also go to my friends and colleagues and the department faculty and staff for making my time at Texas A&M University a great experience. I would also like to thank TAMU Quatar and the Department of Energy for funding this research.

Finally, thanks to my mother, father, brothers, and rest of my family for their encouragement and support.

NOMENCLATURE

AISI	American Iron and Steel Institute
DOD	Depth of Discharge
DOF	Degree of Freedom
E	Elastic Modulus
FEA	Finite Element Analysis
KE	Kinetic Energy
I	Moment of Inertia
P	Pressure
R	Stress Ratio
RPM	Revolutions per Minute
UTS	Ultimate Tensile Strength
V	Volume
W	Watt
m	Mass
r	Radius
u	Displacement
δ	Interference
σ	Stress
υ	Poisson's Ratio
ω	Angular Velocity

TABLE OF CONTENTS

LIST OF FIGURES

Page

LIST OF TABLES

Page

1. INTRODUCTION

1.1 Preface

A flywheel is a rotating mechanical device used to store kinetic energy. Flywheels have been in use for various applications throughout human history for thousands of years. Initially they were used as a means to provide stability, such as a potters wheel. During the Industrial Revolution, they were primarily integrated in steam engines. However, it was not until the late 1960s/early 1970s, with the advent of composite materials and an increased interest in renewable energy sources, that research into the potential for flywheels as a viable alternative to chemical batteries was conducted. The creation of magnetic bearings in the 1980s also exacerbated interest and research. Flywheels can be separated into two categories: conventional and high-performance (superflywheels). Conventional flywheels are constructed from standard materials, most often steel, while superflywheels are composed of composite materials. The present work includes analysis on both types of flywheels, but with the primary focus placed on conventional flywheels. A standard flywheel is shown in Fig. 1-1. Flywheels have been proposed as a replacement or supplement to traditional chemical batteries throughout various areas. These include mobile applications, such as the automotive and aerospace industry, or power regulation in electricity generating plants.

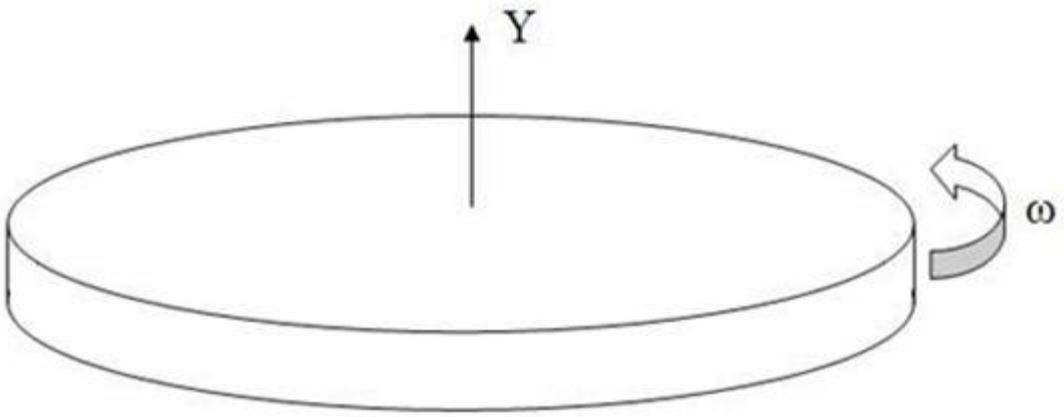

Figure 1-1. Basic flywheel diagram

1.1.1 Energy Storage

With the increasing demand for oil around the world and dwindling non-renewable resources, interest in energy storage has had an uptick in recent decades. The current world energy storage capacity is 90GW from a total production of 3400 GW (i.e. only 2.6% of total electrical energy in the world is capable of being stored) [1]. Energy storage devices add stability and reliability to electrical grids. This in turn improves efficiency and reduces consumption of resources. Instabilities in electrical grids are caused by load variations due to various factors, such as fluctuating input loads from renewable resources (wind and solar), frequency deviations, and discrepancies between peak and average electricity demand. The various methods of energy storage include mechanical, electro-chemical, thermal, electro-magnetic, and chemical systems. Each of these different systems is used depending on efficiency, charge/discharge rate, discharge time, storage capacity, cycling capacity, self-discharge, environmental effects, and costs. Depending on their application, the systems can be divided into four categories [2]:

1. Low-power application in isolated areas, essentially to feed transducers and emergency terminals.

2. Medium-power application in isolated areas (individual electrical systems, town supply).

3. Network connection application with peak leveling.

4. Power-quality control applications.

Large-scale systems, which are primarily used in power plants, include pumped storage hydropower reservoirs and compressed air energy storage. Small scale systems primary function is to provide reliability to the grid and include batteries, fuel cells, super-conducting magnetic energy storage (SMES), super-capacitors, and flywheels. Figure 1-2 shows the power output vs energy stored for the previously stated storage systems. Also included in the figure is the time span of storage capability for each system. As the figure shows, the storage systems that have longer storage capacity, such as pumped hydro storage (PHS), are used for large scale operations for this particular reason. Table 1-1 shows the attached annual costs with some of the previously mentioned storage systems. Flywheel energy storage shows to have the lowest power capacity costs while its energy capacity costs are the second highest from the selected energy storage systems. This means that while it is relatively inexpensive for the output capacity that flywheels provide, storing energy in them for extended periods of time will lead to higher costs relative to other storage options.

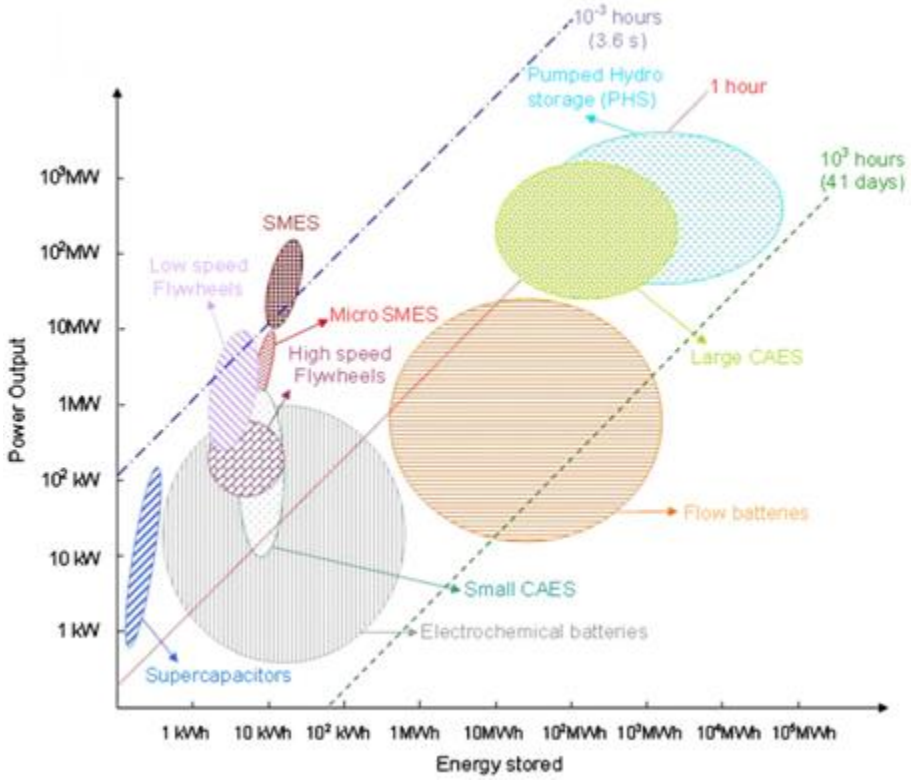

Figure 1-2. Power output vs energy stored [2]

Table 1-1. Estimates of power capacity cost and energy capacity cost for different storage systems. Annual costs assume a discount rate of 9% and a 10-year life cycle. [3]

Electricity storage system	Power capacity costs [US$/kW/year]	Energy capacity costs [US$/kWh/year]
Compressed air energy storage in tanks	120	100-1500
Underground compressed air energy storage	90	5-100
Large scale batteries	70	10-700
Pumped storage hydropower	50	3-90
Super-conducting magnetic energy storage	40	9-150
Flywheel energy storage	30	80-1200

Table 1-2 lists the energy densities of various storage media. As the table shows, energy density of chemical storage is up to three orders of magnitude greater than the next system, although the disadvantages that exist are the resulting pollution and large structures needed to contain the media. Flywheels are shown to be in between in terms of energy density.

Table 1-2. Energy densities of storage media. [3]

Media	Wh/kg^3
Hydrogen	38000
Gasoline	13000
Flywheel, fused silica	870
Flywheel, carbon fiber	215
Flywheel, steel	48
Lead-acid battery	25

1.2 Objectives

The primary objective of the current research is:

1. Design a flywheel configuration that will reduce stresses and increase the maximum specific energy and energy density.

2. Simulate and analyze proposed designs using ANSYS.

3. Reconfigure previous and new flywheels utilizing simulation results.

1.3 Literature Review

The rotating isotropic disk has been studied extensively during the past century by many such as Grubler, Donath, and Stodola [4–6]. However it was not until Genta [7] that analysis of orthotropic materials in rotating disks was formulated. With the introduction of composite materials, the construction and research of composite flywheels increased.

Much research has been conducted concerning the geometry of flywheels. In a rotating disk of constant thickness with no bore, the maximum stress, which in this case is the hoop stress, occurs at the central axis. By changing the shape of the flywheel, the stress can be distributed more evenly throughout causing the radial and hoop stress to be nearly identical [8].

Composite materials are interesting materials because of their high theoretical energy storage limit. The theoretical limit for a particular material is determined by the ratio of its Ultimate Tensile Strength to its density ρ. Table 1-2 lists the theoretical specific energies for certain materials. From the table it is evident there is large difference between the isotropic and composite materials. For the composites the upper bound is not realistic since the material is weaker in the radial direction.

Table 1-3. Strength-to-density ratios of some materials. These values present an upper bound of the specific energy for rotors constructed from these materials. For fiber-composites a unidirectional layup is assumed and UTS represents the tensile strength along the fiber direction. [9]

Material	$(\frac{\text{UTS}}{\rho})$ [Wh/kg]
Isotropic	
Aluminum	61.7
Steel	70.6
Titanium	80.0
Fiber-composite	
S-glass/Epoxy	250
HM-graphite/Epoxy	187
HS-graphite/Epoxy	371
Kevlar/Epoxy	403

Composite flywheel design is separated into three categories: (1) preloaded, (2) growth matching, and (3) mass loaded. The primary method of construction is through filament winding. The resin covered fiber is wound around a mandrel. The result is a cohesive flywheel. The intertial stresses during operation are primarily in the tangential direction. These flywheels have little resistance to stresses in the radial direction which leads to radial delamination. It is a common occurrence and the most likely failure mode as opposed to fiber breakage [10]. A more recent configuration consists of concentric rings. Most often hoop wound rims are constructed with interference between the rims. This creates a preload on the previous rims lowering the net stresses during operation, which leads to a higher operational speed and higher energy storage capacity. While most of the rings are in compression, the final ring in

the flywheel is in tension. Since the outer ring is initially in tension, failure is most likely to occur through fiber breakage, also known as burst criterion. One manner in which this particular problem is addressed is through the construction of a flywheel with rims composed of multiple composite materials as demonstrated by Ha [11]. In his research, hybrid multi-rim rotors of glass/Epoxy and carbon/Epoxy are tested at the failure speed of 30,000 rpm. The lower modulus material, glass/Epoxy, was used at the inner core of the rotor in order to reduce to tensile stresses in the outer carbon/Epoxy. This is the method that is most often used in the industry where the stiffness of the rims is increased throughout the radius.

Pardoen [12] researched achieving desirable stress states in thick rims by varying the mass density and stiffness. A thick rim has the capacity for high energy storage while eliminating the necessity for multiple components present in a multi-rim concept. The problem that is often encountered in thick rims that occur during operation. Pardoen modeled a thick rim with a quadratic variation of mass density and an exponential variation of stiffness. This results in the thick rim behaving like a thin rim, in which r 0, allowing the rim operate at higher speeds and higher energy storage.

Another interesting example for reducing the tensile stress caused by interference on the successive rim is shown by Danfelt [13]. The proposed design contains rubber between the composite rims in order to reduce the stresses. This design has been expanded upon by Portnov [14] but does not appear to have been applied in practical applications in the industry.

1.4 Contribution

This present thesis work provides analyses of novel flywheel geometries using compression on the inner radius of the flywheel in order to increase the mass based

energy density. The main contribution of the present work is as follows:

- Develop and analyzed flywheel concepts to increase specific energy and energy densities in flywheels
- Parametric studies on energy and flywheel geometry for proposed designs.

1.5 Significance

Conventional flywheels made from metals are supplanted by composite due to the vast difference in their tensile strengths. The novelty of this research is the introduction of compression in conventional flywheels to increase their operational limit speed. This can lead to higher energy storage capabilities due to the higher densities of metals compared to composites. Simulation of rotating flywheels has been done using finite element analysis with ANSYS.

1.6 Features and Advantages of Flywheels

The following are advantages of flywheels over other storage systems [15]:

- High power density.
- High energy density.
- No capacity degradation, the lifetime of the flywheel is almost independent of the depth of the charge and discharge cycle. It can operate equally well on shallow or deep discharges.
- The state of the charge can be easily measured, since it is given by rotational velocity.
- No periodic maintenance is required.
- Short recharge time.

- Scalable technology and universal localization.
- Environmental friendly materials, low environmental impact.
- Ability to handle high power levels.

2. THEORY

2.1 Stored Energy

The energy in a flywheel is stored in the form of kinetic energy. This is achieved by applying a torque on the flywheel and reaching a desired angular velocity. It is retrieved by transmitting the torque back into the system sometimes through a shaft attached to the flywheel or electromagnetic bearings. In order to determine the kinetic energy stored in a rotating disk the following formula is used:

$$KE = \frac{1}{2} I \omega^2 \tag{2.1}$$

where I is the moment of inertia and ω is the angular velocity. The moment of inertia itself is found using:

$$I = \frac{1}{2} m r^2 \tag{2.2}$$

In Eq. (2.1) m is the mass and r is the radius. When comparing flywheels as well as other methods of energy storage, the storage potential of the system is often presented on a mass or volume basis, also known as specific energy and energy density respectively. Substituting Eq. (2.2) into Eq. (2.1) and dividing by m the following equation for specific energy is obtained:

$$\frac{KE}{m} = \frac{1}{4} r^2 w^2 \tag{2.3}$$

The energy density can similarly be determined by dividing the energy by the volume, V, and multiplying by the density, ρ:

$$\frac{KE}{V} = \frac{1}{4}\rho r^2 w^2 \tag{2.4}$$

2.2 Multi-Rim Concept

The multi-rim concept consists of a flywheel constructed out of n amount of concentric disks with interference between each rim as shown in Fig. 2-1. An interference fit, or press fit, is a method of joining two parts through friction. This is achieved by overlapping dimensions of the geometries. Interference induces a contact pressure, P_f, on the inner rim, with each successive rim compounding the effect. Figure 2-2 shows the diagram for a 2 disk configuration where r_i is the inner radius of the inner disk, r_o is the outer radius of the outer disk, and r_f is the nominal radius between the outer radius of the inner rim and inner radius of the outer rim after assembly.

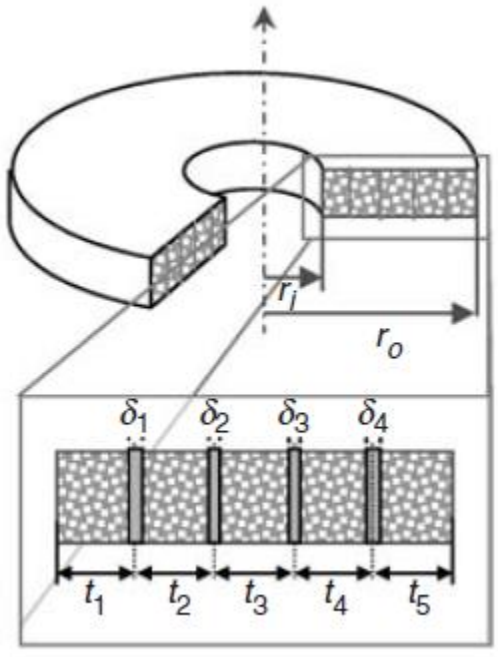

Figure 2-1. Multi-rim press fit rotor. [11]

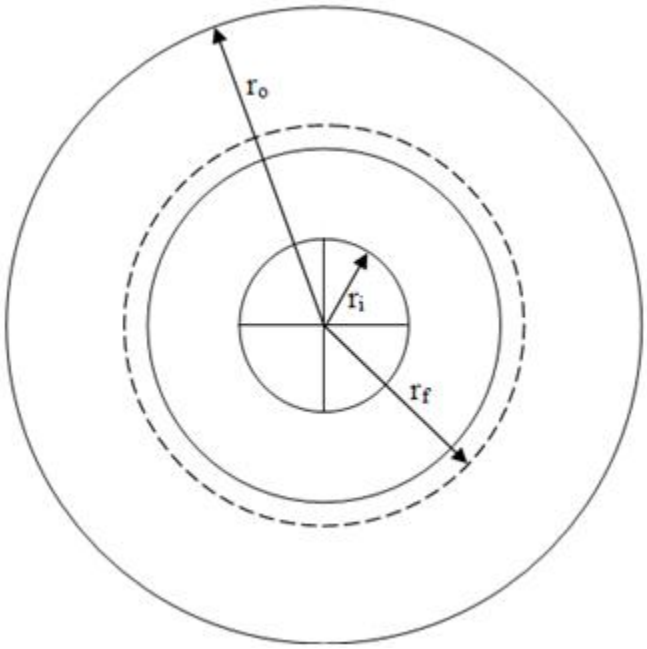

Figure 2-2. Interference fit diagram

The radial interference, δ_r, between the 2 rims can be found using the following equation [16]:

$$\delta_r = r_f P_f \left[\frac{r_o^2 + r_f^2}{E_o^2(r_o^2 - r_f^2)} + \frac{\nu_o}{E_o} + \frac{r_f^2 + r_i^2}{E_o^2(r_f^2 - r_i^2)} - \frac{\nu_i}{E_i} \right] \tag{2.5}$$

where E_i is the modulus of elasticity of the inner rim; E_o is the modulus of elasticity of the outer rim; ν_i is the Poissons ratio of the inner rim with ν_o as the Poissons ratio of the outer rim. The contact pressure can be calculated by [17],

$$P_f = \left[\frac{1}{K_o + K_i} \right] \frac{\delta_r}{r_f} \tag{2.6}$$

where K_o is

$$K_o = \frac{1}{E_o}[\frac{r_o^2 + r_f^2}{r_o^2 - r_f^2} + \nu_o] \tag{2.7}$$

and K_i is

$$K_o = \frac{1}{E_i}[\frac{r_f^2 + r_i^2}{r_f^2 - r_i^2} - \nu_i] \tag{2.8}$$

In order to determine the total stresses in one disk, the problem is further reduced. The result is shown in Fig. 2-3 in which the disk is treated as a pressure vessel. The total stresses on a press-fit rotating disk can then be found by summing the rotational stresses and the interference stresses; however, since the properties of composites are directionally dependant, the formulas for isotropic disks do not apply. Both the isotropic and orthotropic formulas are discussed in the following sections.

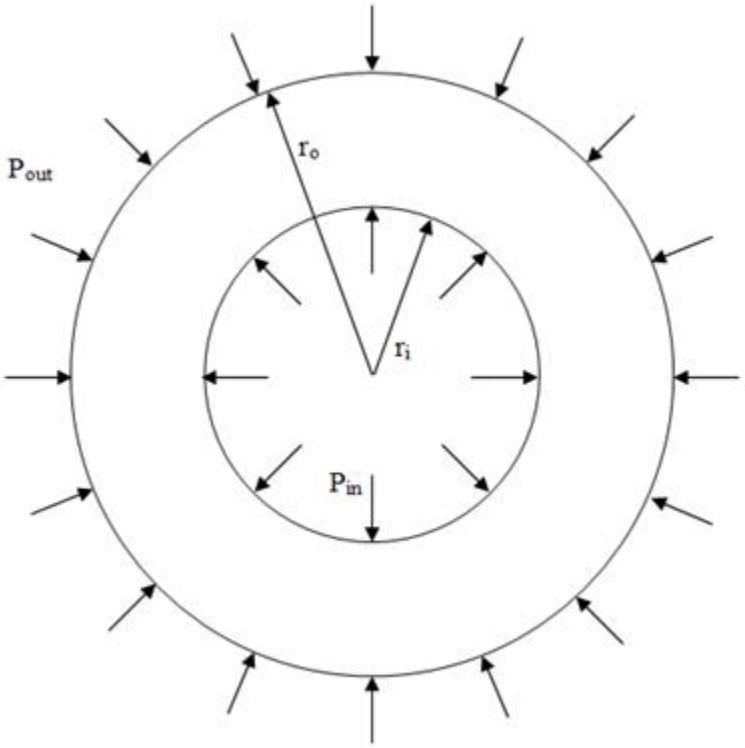

Figure 2-3. Pressure vessel diagram

2.2.1 Isotropic disks

Isotropy refers to the uniformity of material properties in all directions. The steel and Aermet rotors are analyzed under these assumptions. For a rotating annular disk, the formulas for radial stress, σ_r, tangential stress, σ_t, and displacement, u, are [16]:

$$\sigma_r = \rho\omega^2 \frac{3+\nu}{8}(r_o^2 + r_i^2 - \frac{r_o^2 r_i^2}{r^2} - r^2) \tag{2.9}$$

$$\sigma_t = \rho\omega^2 \frac{3+\nu}{8}(r_o^2 + r_i^2 + \frac{r_o^2 r_i^2}{r^2} - \frac{1+3\nu}{3+\nu} r^2) \tag{2.10}$$

and

$$u = \rho\omega^2 \frac{r}{E} \frac{(3+\nu)(1-\nu)}{8} \left(r_o^2 + r_i^2 + \frac{1+\nu}{1-\nu} \frac{r_o^2 r_i^2}{r^2} - \frac{1+\nu}{3+\nu} r^2 \right) \tag{2.11}$$

In the case of a solid disk, $r_i = 0$, reducing Eqs. (2.9) to (2.11) to:

$$\sigma_r = \rho\omega^2 \frac{3+\nu}{8} (r_o^2 - r^2) \tag{2.12}$$

$$\sigma_t = \rho\omega^2 \frac{3+\nu}{8} \left(r_o^2 - \frac{1+3\nu}{3+\nu} r^2 \right) \tag{2.13}$$

and

$$u = \rho r\omega^2 \frac{(3+\nu)(1-\nu)}{8E} \left(r_o^2 - \frac{1+\nu}{3+\nu} r^2 \right) \tag{2.14}$$

For a press-fit disk, the contact pressure must be accounted for, which leads to the following expressions:

$$\sigma_r = -\frac{3+\nu}{8} \rho\omega^2 r^2 + \frac{EC_1}{1-\nu} - \frac{EC_2}{(1+\nu)r^2} \tag{2.15}$$

$$\sigma_t = -\frac{1+3\nu}{8} \rho\omega^2 r^2 + \frac{EC_1}{1-\nu} - \frac{EC_2}{(1+\nu)r^2} \tag{2.16}$$

and

$$u = -(1-\nu^2) \frac{\rho\omega^2}{8E} r^3 + C_1 r + \frac{C_2}{r} \tag{2.17}$$

where C_1 and C_2 are constants that are determined from boundary conditions.

For a rotating disk, the maximum Von Mises stress is:

$$\sigma_{VM} = \sqrt{\sigma_r^2 + \sigma_t^2 - \sigma_r \sigma_t} \tag{2.18}$$

When performing SN life analysis, the stress ratio, R, must first be determined. It depends on the minimum and maximum stress and is defined by:

$$R = \frac{\sigma_{min}}{\sigma_{max}} \tag{2.19}$$

In this particular case, the R is always positive and can be used to measure the depth of discharge (DOD), and their relationship is given as [18]:

$$Depth of Discharge(DOD) = (1 - R) * 100\% \tag{2.20}$$

Figure 2-4 shows the expected life cycles for 4340 steel at various R values.

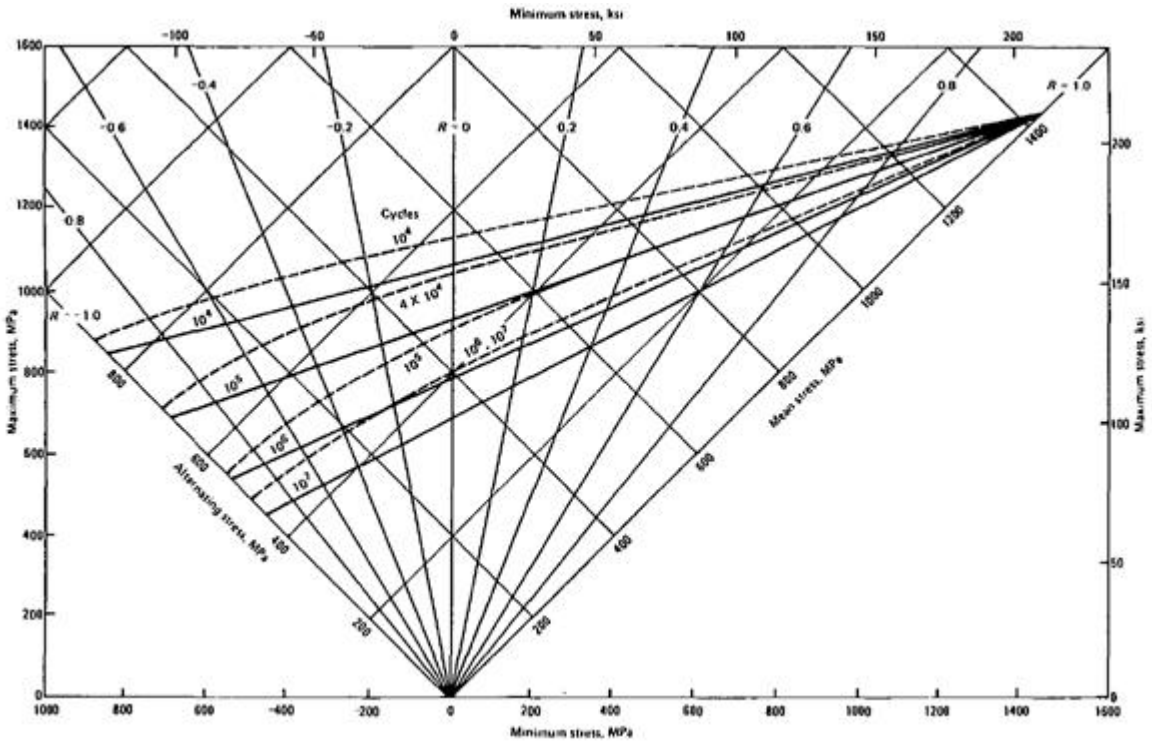

Figure 2-4. S/N curves for unnotched AISI 4340 alloy steel at different R values. [18]

2.2.2 Composite disks

The following formulas were derived to determine the stresses and displacements for a quasi-static, transversely isotropic, rotating disk under thermal and mechanical loads [19]:

$$\sigma_r = C_1 r^{m_1} + C_2 r^{m_2} + Q_1(r) - Q_2(r) \tag{2.21}$$

$$\sigma_\theta = C_1(m_1+1)r^{m_1} + C_2(m_2+1)r^{m_2} + (m_1+1)Q_1(r) - (m_2+1)Q_2(r) + \rho\omega^2 r^2 \tag{2.22}$$

and the displacement is

$$u_r = r\left[\frac{\sigma_t}{E_L} - \frac{\nu_L \sigma_r}{E_L} + \alpha_L(T_{r_i} - T_o) + \frac{T_{r_o} - T_{r_i}}{r_o - r_i}(r - r_i)\right] \tag{2.23}$$

where E_T is the transverse modulus, E_L is the longitudinal modulus, and L is the longitudinal Poissons ratio.

Q_1 and Q_2 are:

$$Q_1(r) = \frac{r^{m_1}}{m_1 - m_2}\int r^{-(m_1+1)} Q(r)dr \tag{2.24}$$

$$Q_2(r) = \frac{r^{m_1}}{m_1 - m_2}\int r^{-(m_w+1)} Q(r)dr \tag{2.25}$$

with

m_1=-1+Σ $\quad$ m_2=-1-Σ $\quad$ $\Sigma=\sqrt{\frac{1}{\beta}}$ $\quad$ $\beta=\frac{E_T}{E_L}$

and

$$
\begin{aligned}
Q(r) = \frac{1}{r_o - r_i}[&rE_L(T_{r_i} - T_{r_o})(2\alpha_L - \alpha_T) \\
&+ r_i\{E_L(T_{r_o} - T_{r_i}) \times (\alpha_L - \alpha_T) + r\rho\omega^2(3 + \nu_L)\} \\
&- r_o\{E_L(T_{r_i} - T_{r_i}) \times (\alpha_L - \alpha_T) + r^2\rho\omega^2(3 + \nu_L)\}]
\end{aligned}
\tag{2.26}
$$

C_1 and C_2 are constants determined from the boundary conditions at the inner and outer radius of the annular disk

$$
(\sigma_r)_{r=r_i} = -P_{in}, (\sigma_r)_{r=r_o} = -P_{out} \tag{2.27}
$$

which in this case are the inner and external pressures on the disk. The resulting equations are:

$$
C_1 = \frac{r_i^{1+\sqrt{\frac{1}{\beta}}}(P_{in} + Q_2(r_i) - Q_1(r_i)) - r_o^{1+\sqrt{\frac{1}{\beta}}}(P_{out} + Q_2(r_o) - Q_1(r_o))}{r_i^{2\sqrt{\frac{1}{\beta}}} - r_o^{2\sqrt{\frac{1}{\beta}}}} \tag{2.28}
$$

$$
C_2 = \frac{r_i^{1+\sqrt{\frac{1}{\beta}}}(P_{in} + Q_2(r_i) - Q_1(r_i)) - r_o^{1+\sqrt{\frac{1}{\beta}}}(P_{out} + Q_2(r_o) - Q_1(r_o))}{r_i^{2\sqrt{\frac{1}{\beta}}} - r_o^{2\sqrt{\frac{1}{\beta}}}} \tag{2.29}
$$

It is possible to use the superposition principle to separate the thermal and rotational terms as show in Eqs. (2.30) and (2.31).

$$
Q_1(r) = Q_1^T(r) + Q_1^R(r) \tag{2.30}
$$

and

$$Q_2(r) = Q_2^T(r) + Q_2^R(r) \tag{2.31}$$

For the present research, thermal effects are neglected and thus have no resultant effect on the stress and displacement

$$T_o = T_{r_i} = T_{r_o} = Q_1^T(r) = Q_2^T(r) = 0 \tag{2.32}$$

reducing Eqs. (2.30) and (2.31)

$$Q_1(r) = Q_1^R(r) \tag{2.33}$$

$$Q_2(r) = Q_2^R(r) \tag{2.34}$$

and the displacement to

$$u_r = r[\frac{\sigma_\theta}{E_L} - \frac{\nu_L \sigma_r}{E_L}] \tag{2.35}$$

The rotational effects are determined by,

$$Q_1^R(r) = \frac{r^2 \rho \omega^2 (3 + \nu_L)}{2\sqrt{\frac{1}{\beta}}[-3 + \sqrt{\frac{1}{\beta}}]} \tag{2.36}$$

and

$$Q_2^R(r) = \frac{r^2 \rho \omega^2 (3 + \nu_L)}{2\sqrt{\frac{1}{\beta}}[-3 - \sqrt{\frac{1}{\beta}}]} \tag{2.37}$$

Various failure criterion exist for composite materials. The Tsai Wu failure criterion is used in the modeling software to determine points of failure through the various strengths of the composite. The failure modes determined by the criterion

consist of fiber-dominated or matrix-dominated failure. Fiber-dominated failure is given as

$$\frac{\sigma_1^f}{F_{1t}} + \frac{-\sigma_1^f}{F_{1c}} = 1 \tag{2.38}$$

and the matrix-dominated failure is

$$f_{22}(\sigma_2^f)^2 + f_{44}(\sigma_4^f)^2 + f_{55}(\sigma_5^f)^2 + f_{66}(\sigma_6^f)^2 + f_2\sigma_2^f = 1 \tag{2.39}$$

with

$$f_2 = \frac{1}{F_{2t}} - \frac{1}{F_{2c}} \tag{2.40}$$

$$f_{22} = \frac{1}{F_{2t}F_{2c}} \tag{2.41}$$

$$f_{44} = \frac{1}{(F_4)^2} \tag{2.42}$$

$$f_{55} = \frac{1}{(F_5)^2} \tag{2.43}$$

$$f_{66} = \frac{1}{(F_6)^2} \tag{2.44}$$

The failure criterion does not indicate the magnitude of safety/failure in the design like isotropic materials. Equations (2.38) to (2.44) are rewritten to obtain a strength ratio R.The fiber-dominated strength ratio R_1 is

$$R_1 = \frac{F_{1t}}{\sigma_1} + \frac{-F_{1c}}{\sigma_1} \tag{2.45}$$

and the matrix-dominated strength ratio is determined by

$$(f_{22}(\sigma_2)^2 + f_{44}(\sigma_4)^2 + f_{55}(\sigma_5)^2 + f_{66}(\sigma_6)^2)R_2^2 + (f_2\sigma_2^f)R_2 - 1 = 0 \tag{2.46}$$

which can be written as

$$aR_2^2 + bR_2 - 1 = 0 \tag{2.47}$$

where the strength ratio is the smallest positive value from the following solution

$$R_2 = \frac{-b \pm \sqrt{b^2 + 4a}}{2a} \tag{2.48}$$

2.3 Novel Concepts

Several new concepts that induce compression on a conventional rotor were designed and analyzed and are presented throughout this section. The intent is to replicate the behavior that occurs with a multi-rim interference fit rotor without the tensile stress that often results in the outer rim. They are shown in the chronological order in which they were designed and implemented. Some designs utilize ideas from prior concepts. Table 2-1 lists the designs and a description of their mechanism.

Table 2-1. Concepts and description.

Concept 1	Steel flywheel with steel rims
Concept 2	Steel flywheel with composite rims
Concept 3	Flywheel with pressurized internal cavity
Concept 4	Welded flywheel
Concept 5	Flywheel with internal press fit
Concept 6	Stepped flywheel
Concept 7	Rotor-collar flywheel

2.3.1 Flywheel with Pressurized Internal Cavity

Figure 2-5 shows the flywheel designed with an internal cavity. A pressure is applied on the boundaries of the cavity. It is expected to result in compression of the inner section without the high stresses that tend to occur near the outer radius of multi-rim rotors. This in turn will lead to higher allowable operating speeds and energy densities.

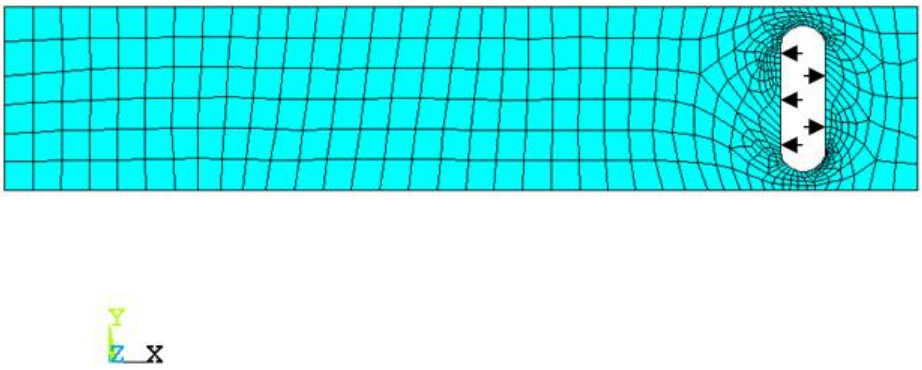

Figure 2-5. Flywheel with internal cavity

2.3.2 Welded Flywheel

Welding is a method of joining materials by melting the pieces and using a filler material for the joint. Stress concentrations and discontinuities are not expected or should be minimal if the welding is performed correctly. Figure 2-6 shows the model of a welded flywheel. The flywheel consists of 2 components: a solid disk and outer

ring. Sliding is not permitted and it is essentially linear contact.

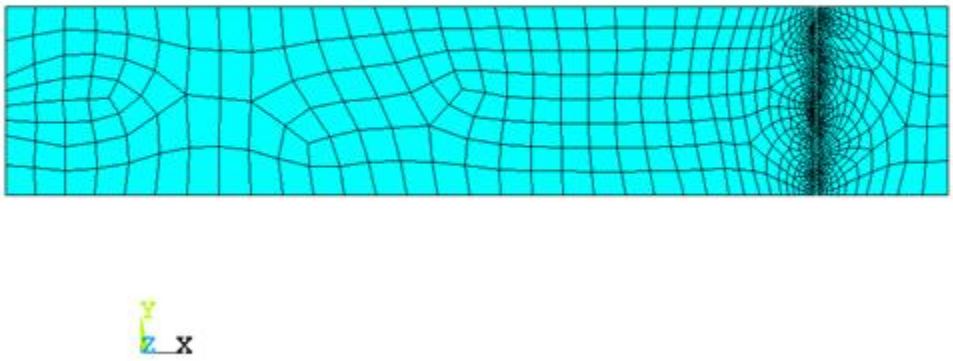

Figure 2-6. Welded flywheel

2.3.3 Welded Flywheel with Internal Press Fit

Figure 2-7 represents a flywheel that incorporates both welding and interference in its design. As stated previously, welding of objects should result in very small or no stress concentrations at the interface and no discontinuities across the joint. It is reasonable to assume that by applying these conditions the stress will be distributed more evenly across the rotor and lead to lower stresses in the outer section.

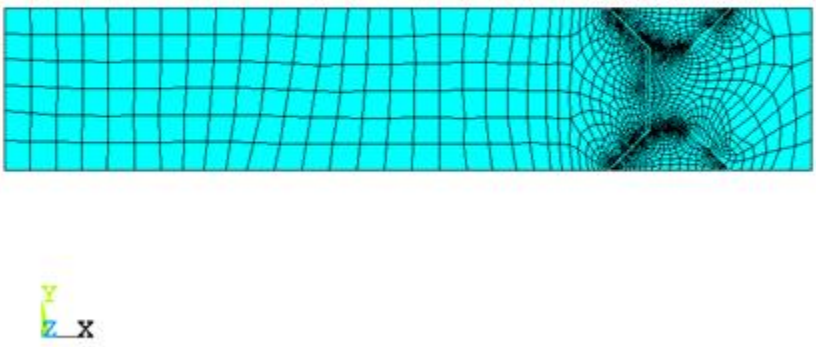

Figure 2-7. Welded flywheel with internal press fit

The trapezoidal sections in the model represent welding pools. Welding pools are the areas where the bonding material and target area interact. A contact pair with the bonded (always) option is created for each edge adjacent to the rotor components. An interference fit of varying depth applies the necessary contact pressure on the inner section. Fine mesh size is applied at all the contact areas to obtain accurate results.

2.3.4 Stepped Flywheel

The model in Fig. 2-8 is designed to implement the pressure directly at the area of interest. Due to its proximity to the center of the rotor, the applied pressure is expected to greatly reduce the stresses during high-speed operation relative to the previous designs. Transition location is manipulated to obtain the greatest stress reduction while limiting stress concentrations.

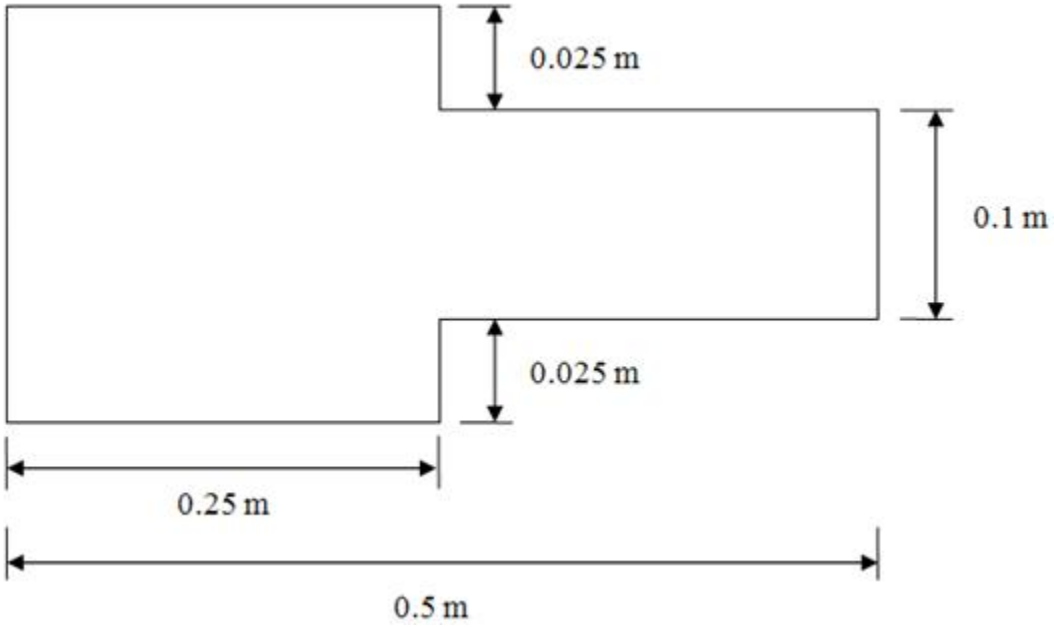

Figure 2-8. Flanged rotor diagram

The stepped rotor design is symmetric across the center of its geometry. By modeling using symmetry, the analysis is simplified and reduces computation time. Figure 2-9 is the symmetric model used for the analysis.

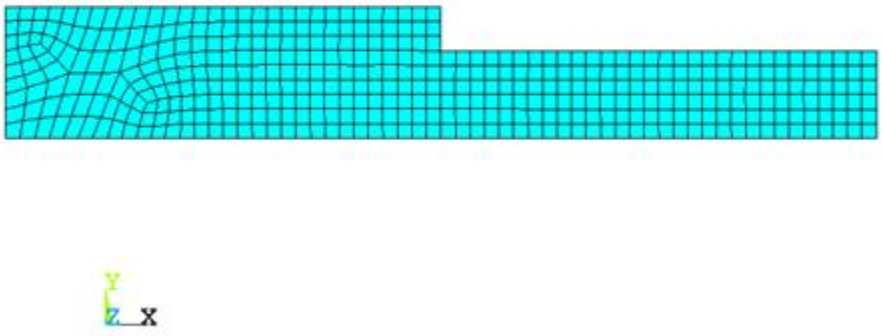

Figure 2-9. Symmetric flanged rotor model

2.3.5 Rotor-Collar Flywheel

Implementation of the side pressure concept is achieved through applying interference between a collar, seen in Fig. 2-10, and the rotor, shown in Fig. 2-11, at the transition area. A slope is applied to both the collar and the rotor in order to affect the resulting contact pressure and stress concentrations that occur near this section, where θ is taken relative to the vertical axis. Figure 2-12 shows the resulting simulated model. Fine mesh density is applied to the intersecting and contacting surfaces to obtain accurate results.

Figure 2-13 shows a diagram of the various parameters used to determine the slope, interference, and transition point that provide the optimum contact pressure. In this case, x is the location of the transition point, L is the total length of the

Figure 2-10. Collar diagram

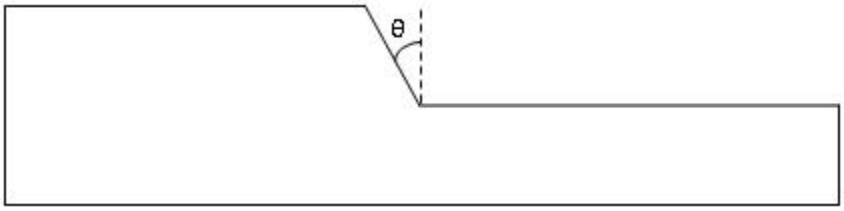

Figure 2-11. Rotor diagram

flange section, D_1 the distance between the top of the rotor flange and slope of the collar, and δ the interference.

The following equations are used to determine the geometric dimensions for the rotor and collar. First the desired taper angle of the rotor, θ_R, is specified and the length of the taper is determined by:

$$M_r = tan(\theta_R) \tag{2.49}$$

A transition point and rotor-collar gap is chosen. Then the slope of the collar, interference, and angle of the collar are determined by using the following equations:

$$-M_D x - D_I = -M_R x \tag{2.50}$$

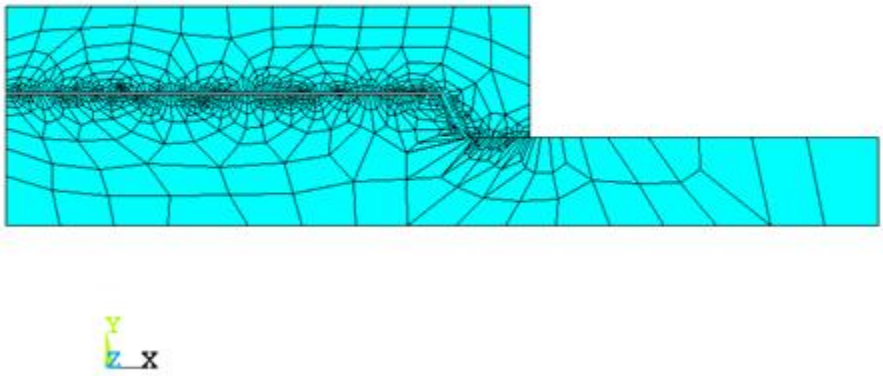

Figure 2-12. Rotor with collar model

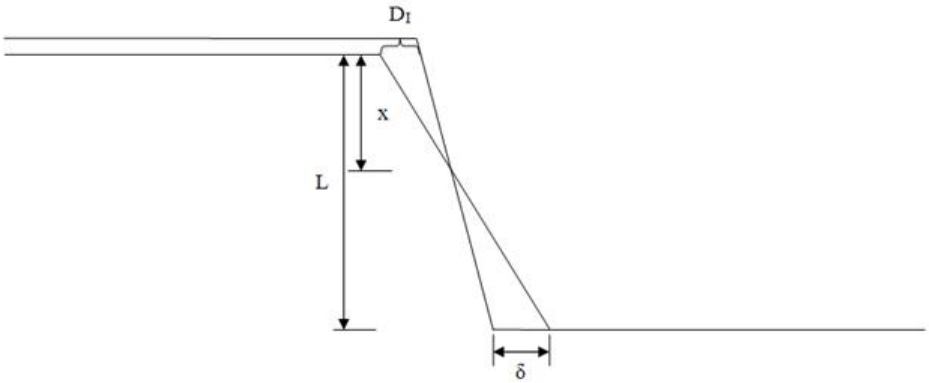

Figure 2-13. Parameterization rotor-collar interference diagram

$$M_D + D_I = M_R L - \delta \tag{2.51}$$

$$\theta_D = tan^{-1}(M_D) \tag{2.52}$$

During high speed operation, radial growth is expected to occur. Bending may also be present in the collar. This will lead to loss in contact pressure and an increase in stresses in the rotor. With the use of the previous formulas, the optimum combination of the parameters for a favorable contact pressure profile can be determined. It is expected that by performing a study using the parameterized variables determining the factor with the highest impact on the rotor-collar flyhweel design will allow for maximum compression on the rotor which in turn will lead to higher energy storage values.

3. ANSYS MODELING

Finite Element Analysis (FEA) is a method of discretizing a problem and utilizing the resulting elements to solve for the desired outputs. Its use in analyzing the proposed flywheels is primarily for determining the stress profile and displacements. The program used in the analysis is ANSYS 13.0. A combination of the Mechanical APDL GUI and command files is used.

3.1 Axisymmetry

The flywheels modeled are assumed be axisymmetric due to their symmetry around their central axis. This reduces the dimensions of the problem and decreases computation time. A PLANE182, shown in Fig. 3-1 is used for 2-D modeling of solid structures with the axisymmetric option selected. It is defined by four nodes having 2 degrees of freedom at each node: translations in the nodal x and y directions.

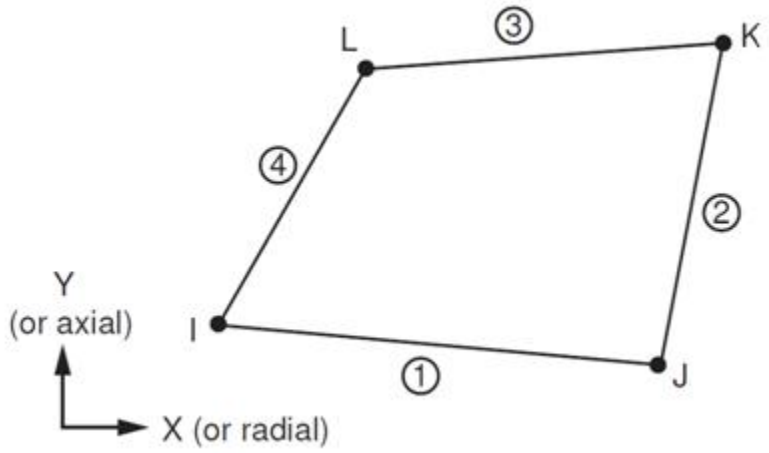

Figure 3-1. PLANE182 geometry

Figure 3-2 shows the cross section of the standard flywheel used in the simulations. In addition to specifying axisymmetry, it is also important to restrict the displacement of 1 node in the y-direction to prevent rigid body movement. Failure to do so may lead to errors or termination of the analysis.

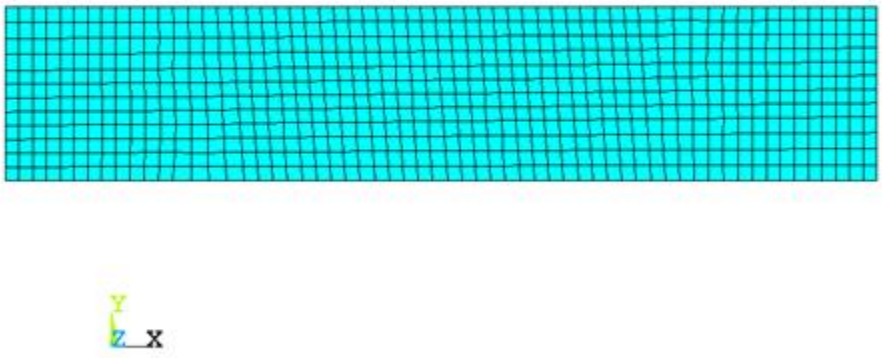

Figure 3-2. Axisymmetric cross-section

3.2 Material Properties

Figure 3-3 shows the inputs for a linear isotropic material. In isotropic materials the properties are equal in every direction and only one input for each property is required. EX is the modulus of elasticity and PRXY is the Poissons ratio. It is also necessary to input the density of the material.

Composite materials are applied to the models in certain simulations. The properties of composites are orthotropic (i.e. properties are directionally dependant).

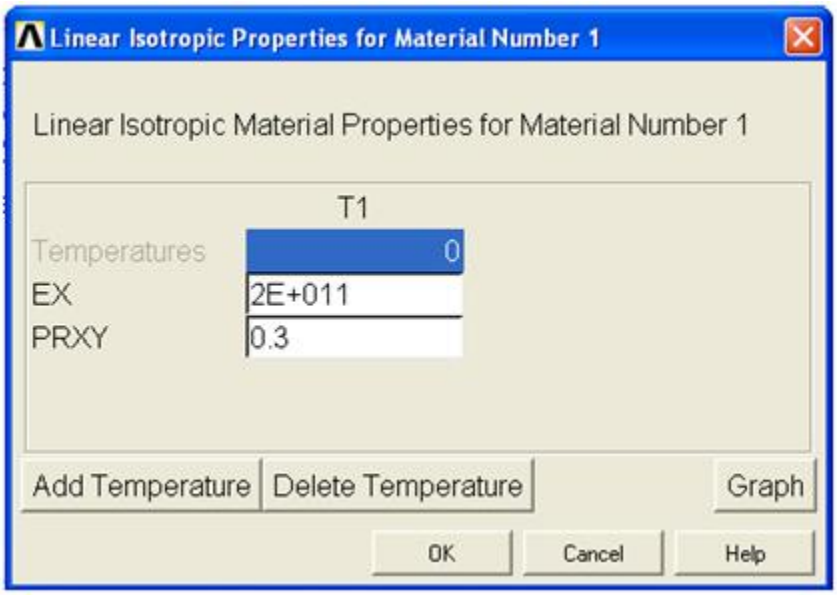

Figure 3-3. Linear isotropic options

However, the composite material used in the simulations is transversely isotropic in which the properties in the transverse direction are equal and differ in the longitudinal direction. When creating the material model, the corresponding elastic modulus, E, modulus of rigidity, G, and Poissons ratio, ν, must be defined for the three different axis as seen in Fig. 3-4. For the simulation models, the element z-direction is analogous to the tangent direction, element y-direction is axial and element x-direction is radial. This element coordinate system (or material coordinate system) is important for applying the correct material property in the correct direction. The properties given are applied in the element coordinate system. The fiber is in element z-direction, transverse direction of lamina is in element y-direction and thickness is in element x-direction. The Young's modulus should be as $E_{zz} = E_1$, E_{xx}=E_{yy}= E_{22}, ν_{zy}= ν_{zx} = ν_1, ν_{yx}=ν_2, G_{zy} = G_{12}, G_{yx}= G_{23} and G_{zx}= G_{13}. Since Poisson's ration is not symmetric and can only be input in ANSYS in the form of ν_{xy}, ν_{yz} and ν_{xz}, it is necessary to determine the corresponding values using the following expressions:

$$\frac{\nu_{yx}}{E_y} = \frac{\nu_{xy}}{E_x} \tag{3.1}$$

$$\frac{\nu_{zx}}{E_z} = \frac{\nu_{xz}}{E_x} \tag{3.2}$$

$$\frac{\nu_{yz}}{E_y} = \frac{\nu_{zy}}{E_z} \tag{3.3}$$

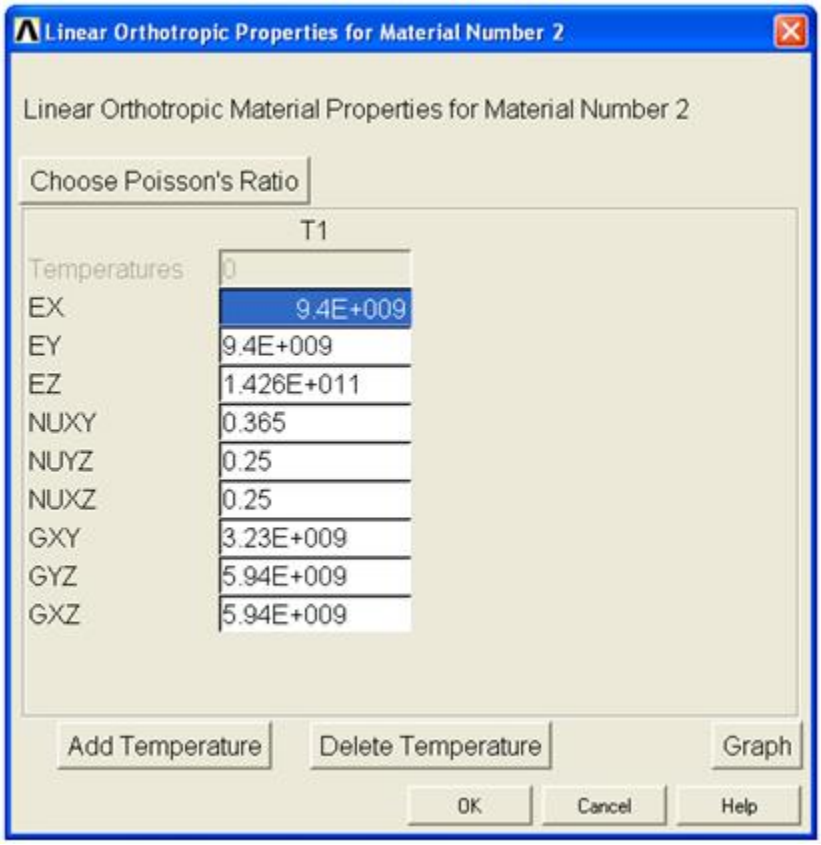

Figure 3-4. Linear orthotropic options

Poissons ratios can be input as either major or minor values. From Eq. (3.3), if yz $<$ zy it will input as a minor Poisson's ratio. Similarly, the other Poissons ratio values may be calculated.

3.2.1 Failure Criteria

Determining failure in a design becomes difficult when modeling orthotropic materials due to the nonuniformity of the properties. ANSYS allows the user input the strengths of the composite in order to use failure criteria specific to the material. Figure 3-5 shows the option window for the failure criteria. It is neceesary for all 9 directional properties of the material to be input as strains or stresses. Combining either stresses or strains for the purpose of the failure criteria will result in an error. Tensile strengths and strains have a positive value and compressive stresses and strains are input as negative values. Figure 3-6 shows the available failure criteria for the material. Further information of the various failure criteria is available in chapter 2 section 2.4 in the theory reference of the Mechanical APDL Structural Analysis Guide.

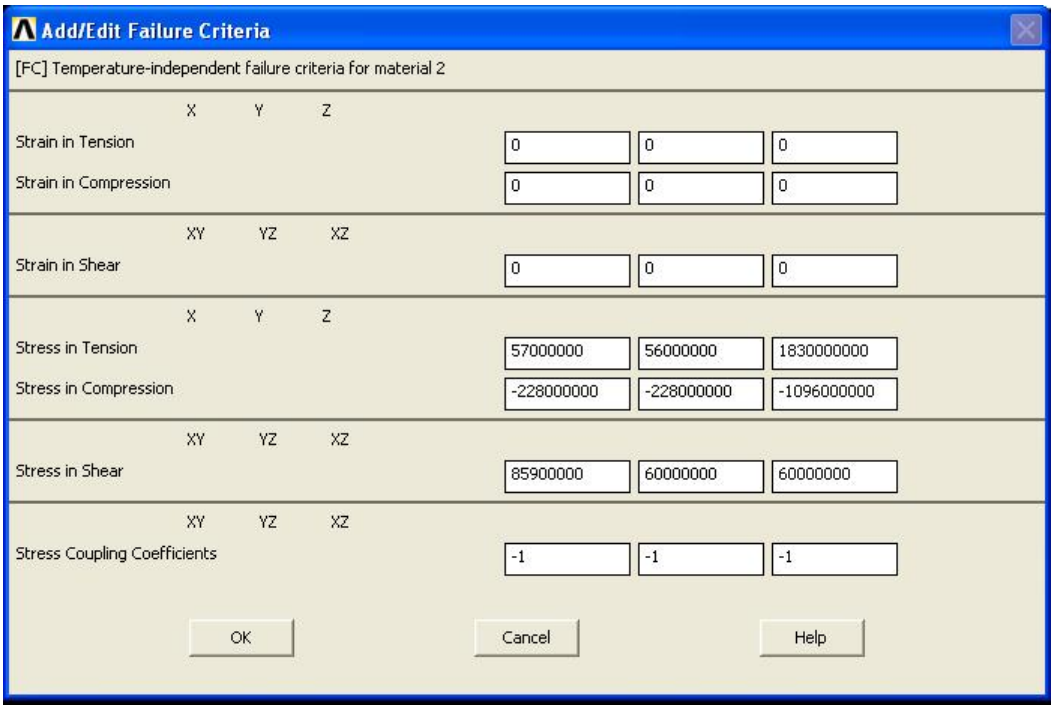

Figure 3-5. Failure criteria properties

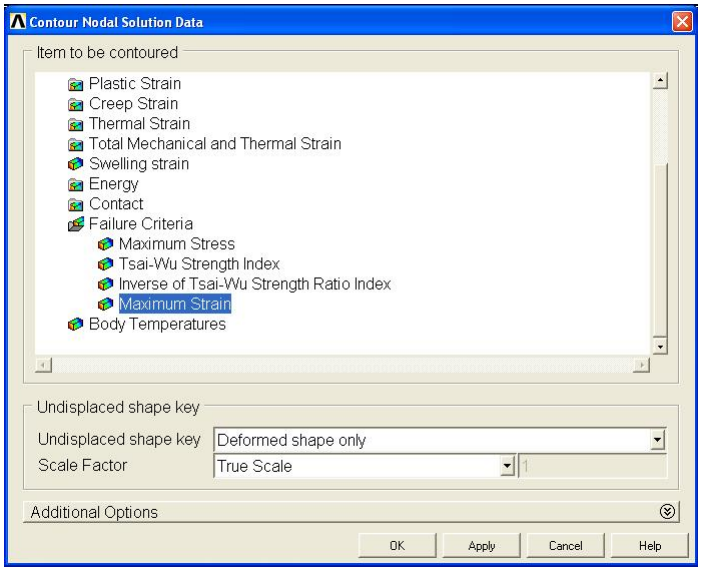

Figure 3-6. Failure criteria outputs

3.3 Contact Elements

Contact elements are used to model both interference and welded joints. A contact pair is created between the 2 interfering surfaces using the TARGE169 and CONTA171 elements. Fine meshing is applied on contact surfaces in order to obtain accurate results. The contact surface and target surface are then defined. When applying the contact and target element, the inner surface is treated as the contact and the outer as the target element. It is possible to define the contact as symmetric or unsymmetric. The symmetric option designates one surface as the target and the other as the contact. Unsymmetric contact applies target and contact elements to both surfaces which can lead to increased computation time and errors in the results. 2D interference and welded joints are modeled accurately as symmetric contacts. In order to model an interference fit the behavior of the contact surface must be set to standard. The bonded(always) option is set when modeling a welded joint as seen in Fig. 3-9.

TARGE169 is an element used for 2D target surface-to-surface contact. Figure 3-7 shows the element geometry. There are no real constants or key options that require definition for simulation of interfering or welded contacts.

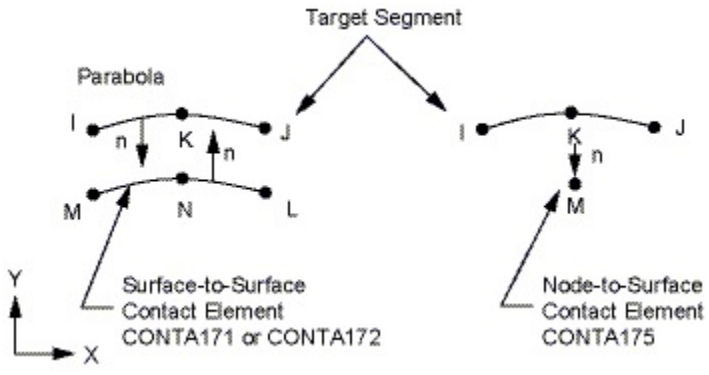

Figure 3-7. TARGE169 geometry

CONTA171 elements represent contact and sliding between 2D target surfaces and a surface defined with this element and its geometry is shown in Fig. 3-8. The real constant necessary to define is the pinball region. A constant value greater than the interference must be applied to provide accurate results. Values lower than the interference will result in inaccurate results or termination of the simulation.

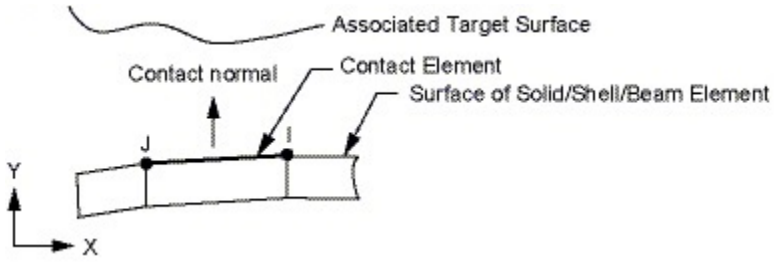

Figure 3-8. CONTA171 geometry

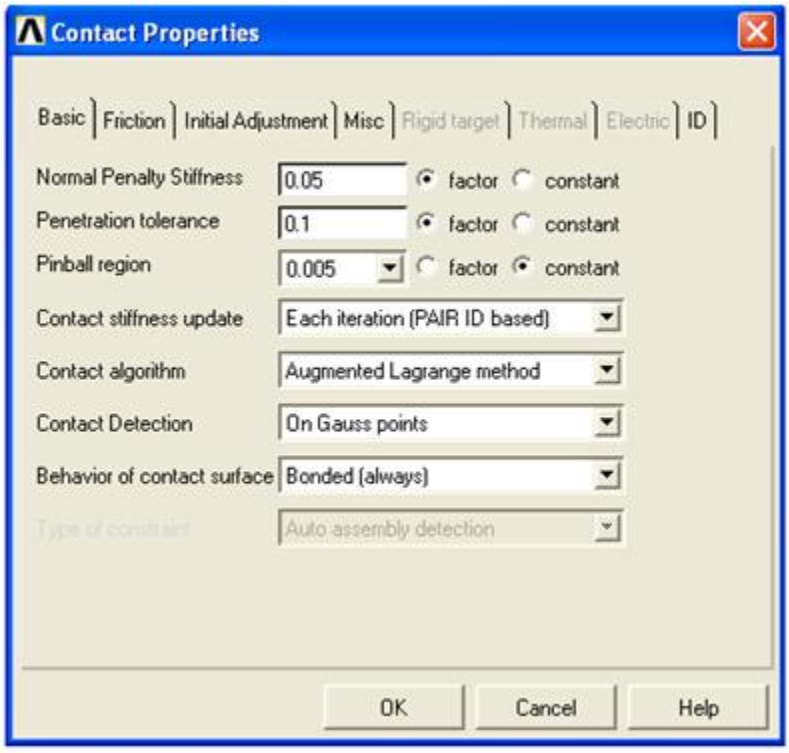

Figure 3-9. Contact properties

3.4 Command Files

ANSYS contains a coding environment known as the ANSYS Parametric Design Language (APDL). The language allows the user to automate simulations by inputting a text file with the appropriate ANSYS commands. It essentially performs all the tasks shown in the GUI without having to access each specific criteria manually. It allows for quicker results during instances where constant iterative simulations are required. The text file of choice is input by selecting File⇒Read Input from...⇒*File.txt* where *File.txt* is the desired text file to be input. A number of sample command files used for this thesis are attached in the appendix. Command descriptions can be found in the ANSYS command manual.

4. SIMULATION

The primary materials applied in the isotropic flywheels are metals, specifically, steel and AerMet. Heat treated AISI 4340 steel is used with $\rho = 7850$ kg/m^3, E = 200 GPa, Ultimate Tensile Strength (UTS) = 1014 MPa, and $\nu = 0.3$. AerMet 310 is also used in some simultations with the following properties: $\rho = 7970$ kg/m^3, E = 192 GPa, Ultimate Tensile Strength (UTS) = 2170 MPa, and $\nu = 0.31$.

4.1 Standard Steel Flywheel

Initially a solid disk flywheel is modeled to establish a base energy density. Figure 4-1 is the axisymmetric cross section of the flywheel with a radius of 0.5 m and thickness of 0.05 m. Analysis is conducted at operating failure speed to determine maximum specific energy and energy density (i.e. the angular velocity at which the stress in the flywheel is greater than the UTS). Figure 4-2 is the meshed model.

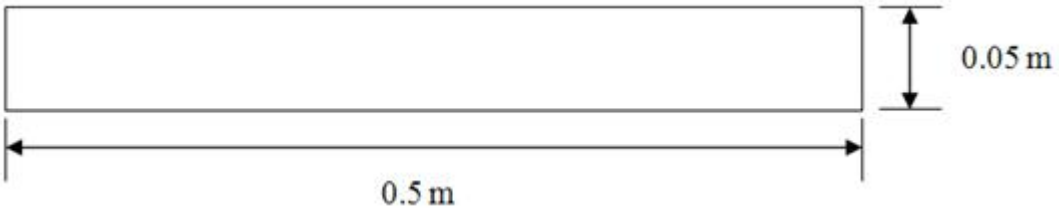

Figure 4-1. Solid disk steel flywheel diagram

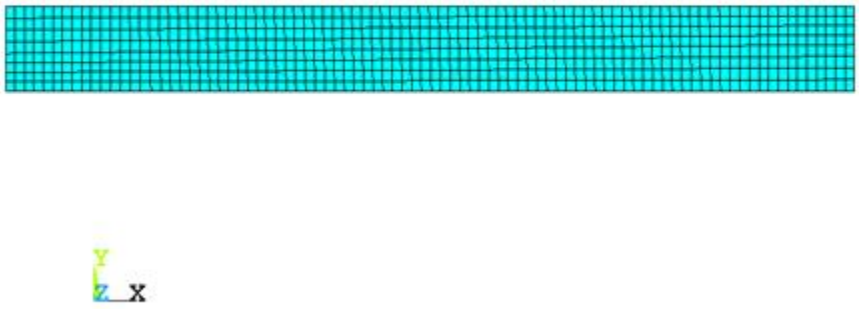

Figure 4-2. Solid disk steel flywheel model

The failure speed for the solid steel disk is determined to be 11000 rpm. Figures 4-3 to 4-6 show the stress distributions and displacement at the maximum operating speed. As seen in the figures, the maximum stresses occur at the center of the flywheel. These results correspond to the expected stress behavior from the literature. To further validate results, the stresses and displacements are compared with the analytical solutions from Eqs. (2.12) to (2.14). Table 4-1 lists the stress and displacement results obtained from ANSYS and analytical solutions. The percentage difference shows all values are within 10% and can be considered accurate. Maximum specific energy and energy density for the base model is 23.04 W/kg and 180.96 kW/m^3. Proceeding models are modified to improve upon these values.

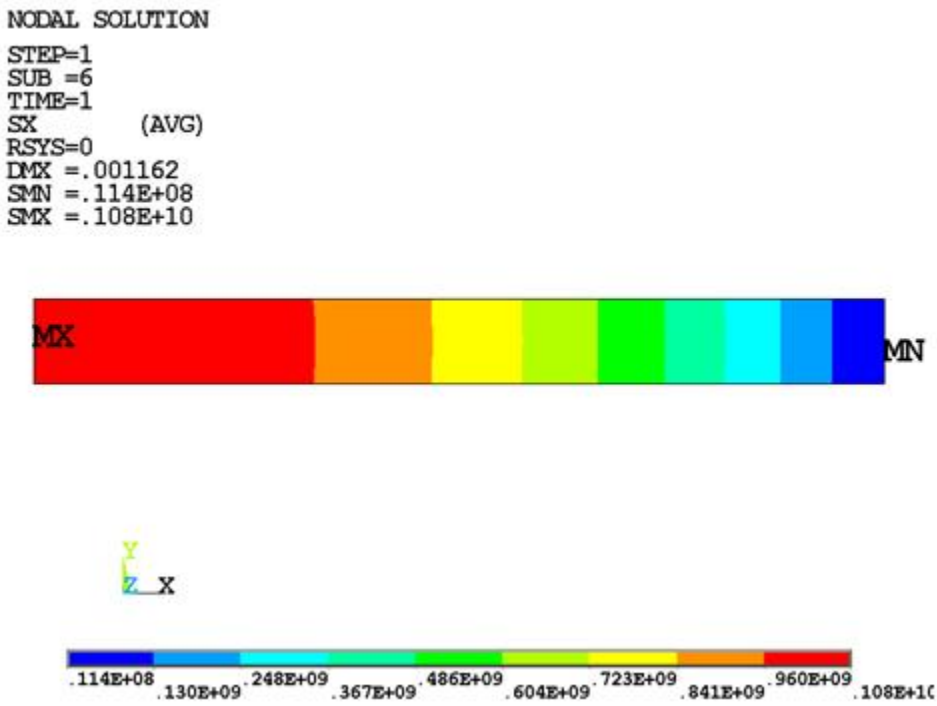

Figure 4-3. Standard flywheel radial stress

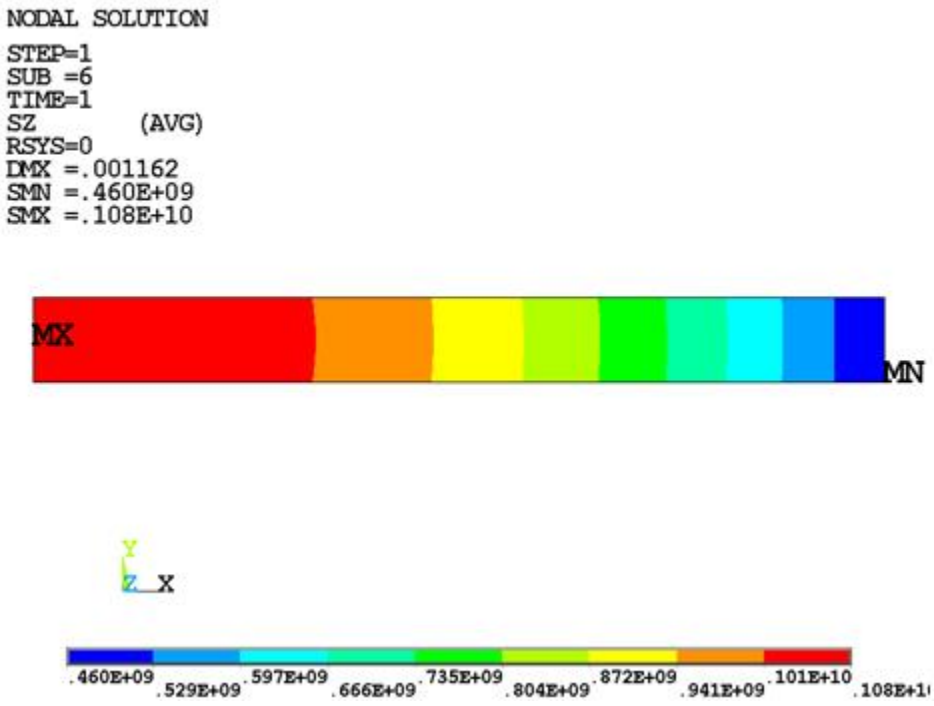

Figure 4-4. Standard flywheel tangential stress

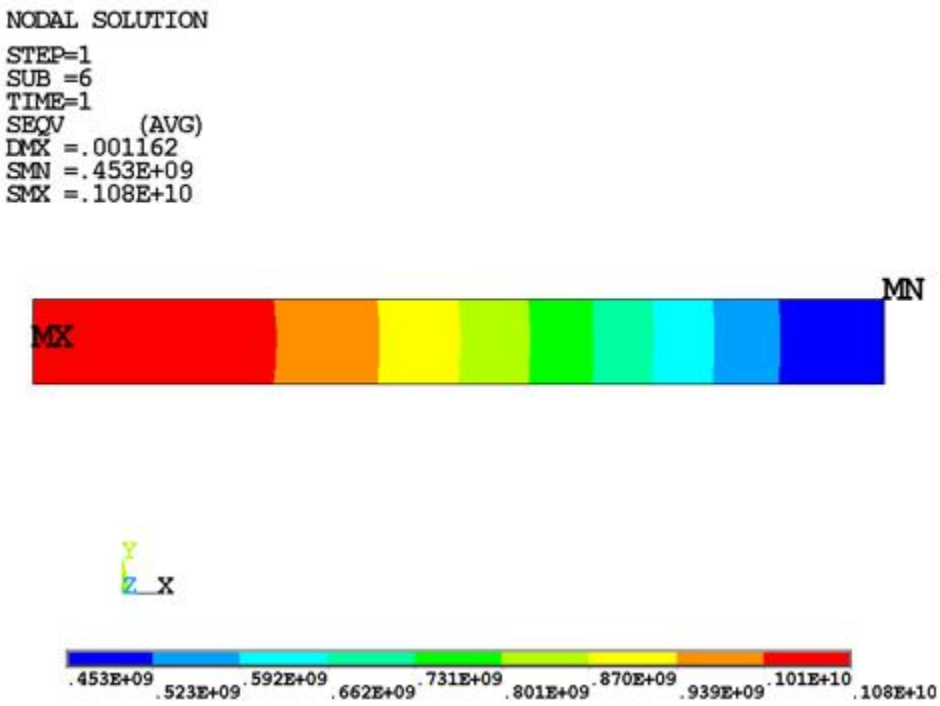

Figure 4-5. Standard flywheel Von Mises stress

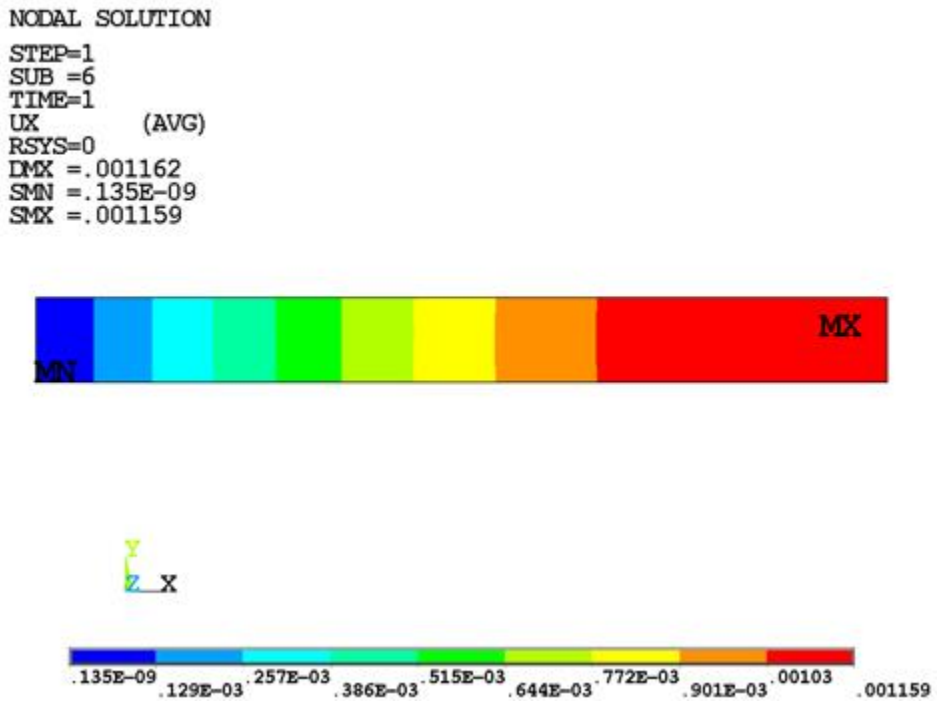

Figure 4-6. Standard flywheel radial displacement

Table 4-1. Max stresses and displacements for solid steel flywheel.

	σ_r (MPa)	σ_t (MPa)	u (mm)
ANSYS	1080	1080	1.12
Theoretical	1074	1074	1.14
% difference	0.56	0.56	1.75

4.2 Multi-Rim Steel Flywheel

Using the multi-rim concept seen in construction of composite rotors, a steel flywheel is simulated with multiple rims to determine if the compression caused by

the interference increases the allowable operating speed, which leads to a higher energy density. Several models are created with a solid steel wheel and a varying amount of rims. The size of the rims and steel disk are modified to maintain a flywheel with a radius of 500 mm.

Initially a flywheel with one steel rim at 0 rpm is modeled to ensure the contact pair is applied correctly. Interference between the disk and the rim is 1 mm as shown in Figure 4-7. Figure 4-8 plots the contact pressure between the disk and the rim with an average value of 90.8 MPa. From Eq. (2.6), the contact pressure is found to be 90 MPa which results in an error of 0.89%.

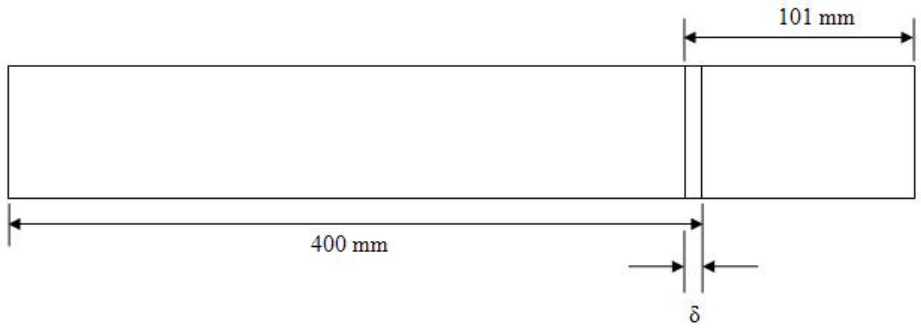

Figure 4-7. Steel flywheel with 1 steel rim

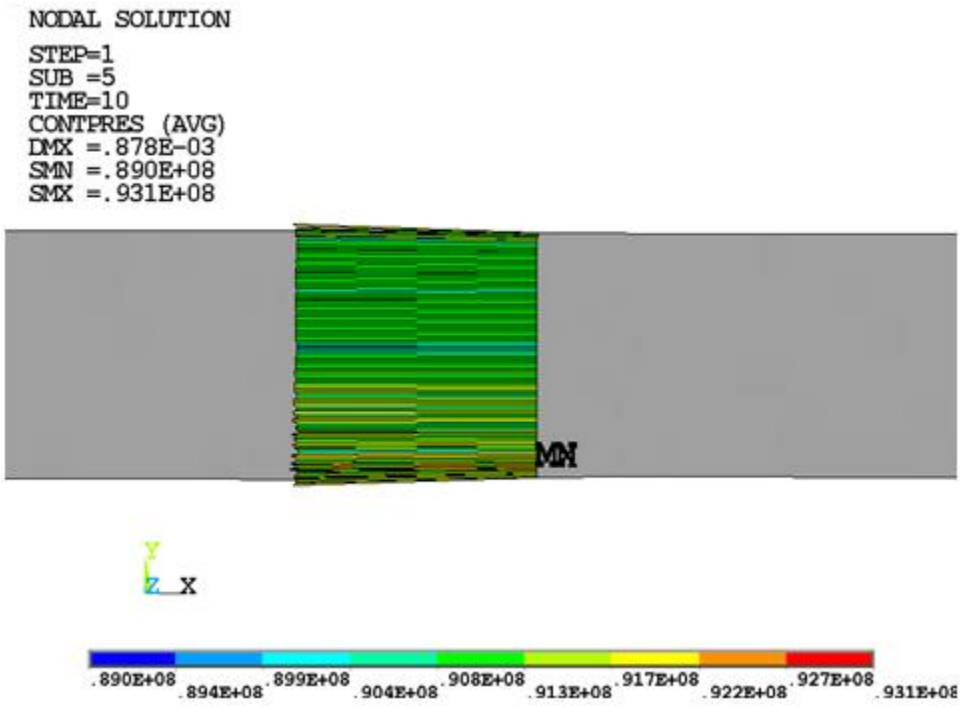

Figure 4-8. Steel wheel-1 steel rim contact pressure at 0 rpm

The maximum angular velocity of the solid steel flywheel, 11000 rpm, is applied to the model in order determine if there is an improvement in the energy density. From Figure 4-9 the simulation shows the tangential and radial stresses are greater than the frictional stress (i.e. the rim separates from the disk). Interference is increased from 1 mm to 3 mm. It is expected that the increased interference will increase the frictional stress and maintain the joint between the disk and the rim. The results show a similar situation occurs as in the previous case. A flywheel with 3 rims is modeled to determine if additional compression will maintain contact during operation. The interference between each rim is maintained at 3 mm. Contact pressure values, seen in Fig. 4-10, show that the rims remain attached to the disk at 11000 rpm.

Figure 4-9. Steel wheel-1 steel rim contact pressure at 11000 rpm

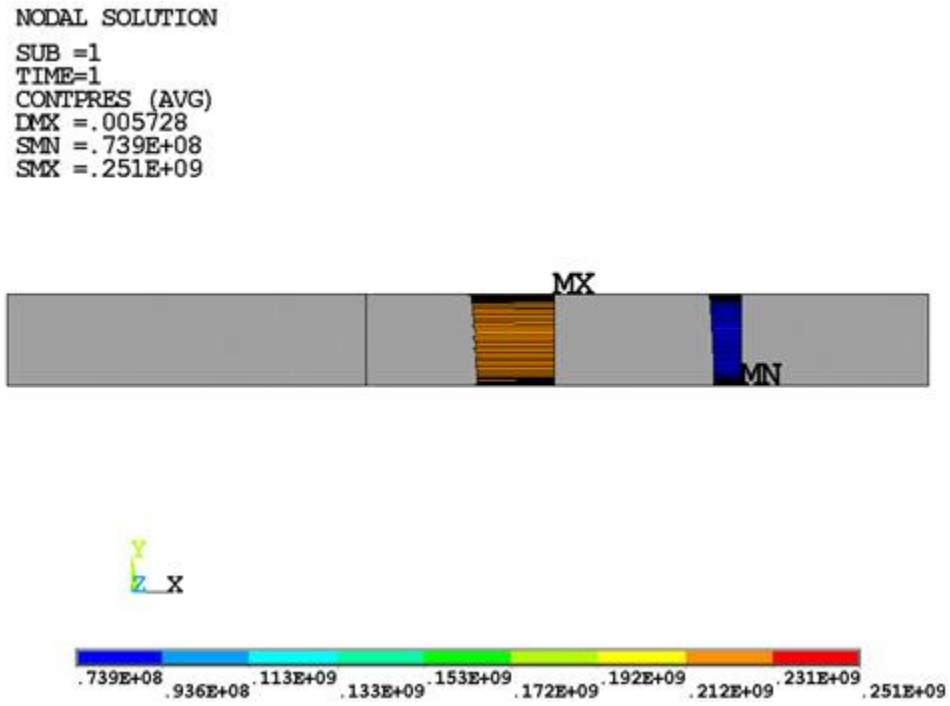

Figure 4-10. Steel disk 3 steel rim contact pressure

The Von Mises stress is then plotted to determine if the flywheel is still operable. From Fig. 4-11, it is shown that the steel disk and inner rim are well below the UTS, however, the stresses in the outer 2 rims are well above the limit with the maximum occurring near the inner radius of the outer rim. This value is 2890 MPa, which is almost 3 times the UTS, and initial failure is expected in the outer rim.

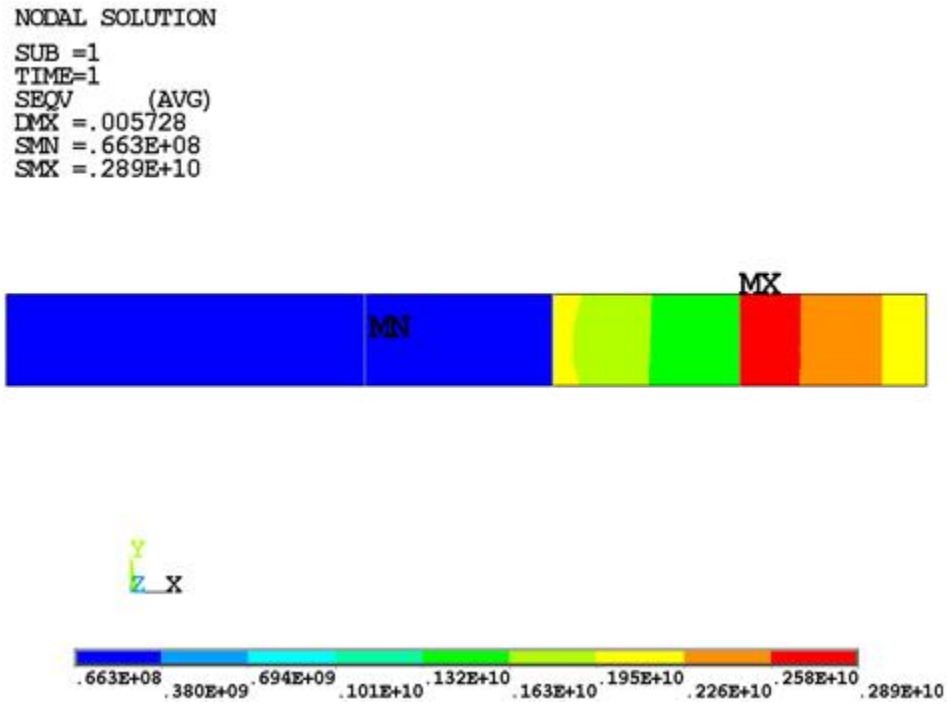

Figure 4-11. Steel disk-3 steel rim Von Mises stress

Previous results show a steel rim will fail due to the high stresses caused by the interference and high speed. In order to counteract the high tensile stress that occurs a composite rim is placed on the steel flywheel to provide compression to the steel wheel and allow for a high operating speed due to the composites high tensile strength. The failure speed for this particular flywheel design is determined to be 11500 RPM. Figure 4-12 plots the radial stress of the flywheel at the failure speed.

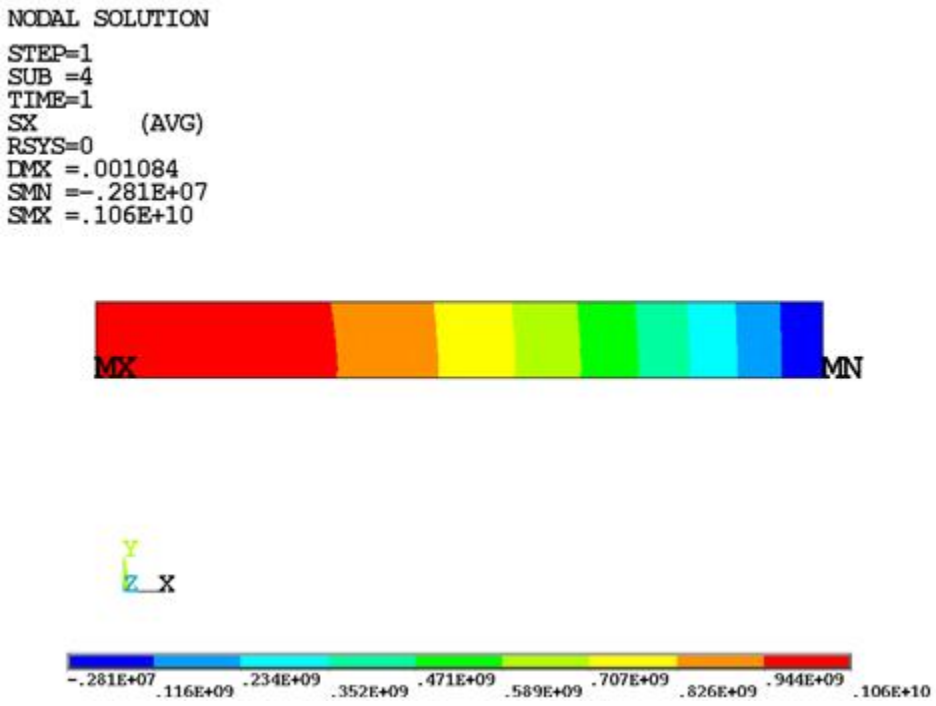

Figure 4-12. Hybrid flywheel radial stress

Figures 4-13 and 4-14 plot the tangential and Von Mises stress. As in previous simulations, the flywheel fails near the inner radius. However the composite rim remains operational at the current speed. The composite rim can operate at higher speeds, but the steel flywheel will fail. An increase in the compression through a greater interference or multiple rims will allow for the flywheel to operate at higher speeds.

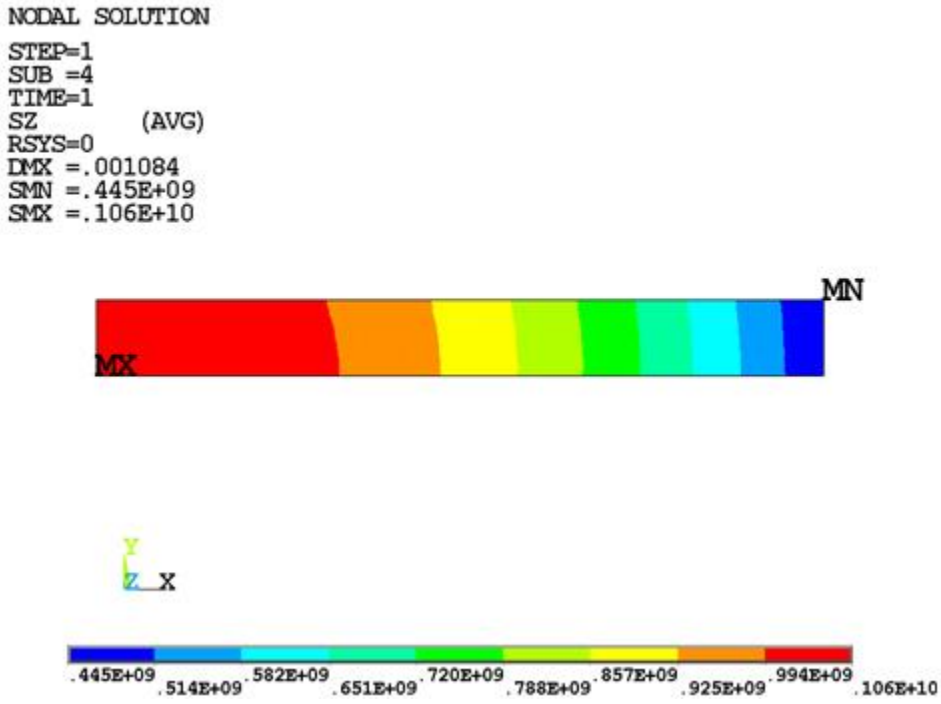

Figure 4-13. Hybrid flywheel tangential stress

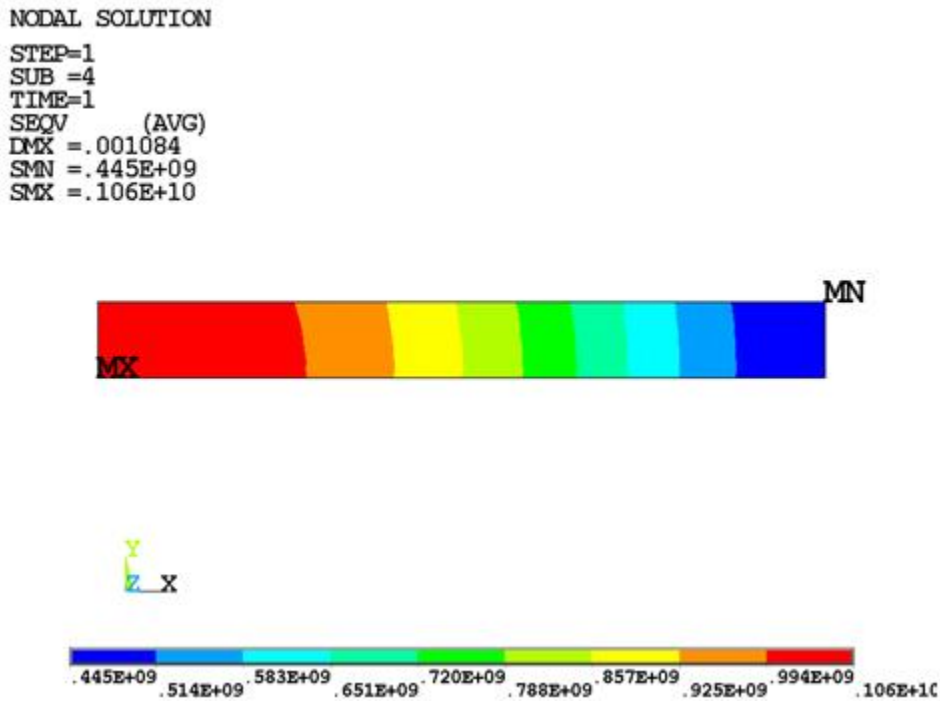

Figure 4-14. Hybrid flywheel Von Mises stress

4.3 Composite Flywheel

From the previous results, it appears the outer rim undergoes high tensile stresses caused by the compression of the inner rims. In order to design an operable flywheel, a high strength carbon-epoxy composite, AS4 3501-6, is applied to the rims with the following properties: $\rho = 1580$ kg/m^3, $E_{11} = 142.6$ GPa, $E_{22} = 9.4$ GPa, $\nu_{12} = 0.25$, $\nu_{23} = 0.365$, $F_{1t} = 1830$ MPa, $F_{1c} = 1440$ MPa, $F_{2t} = 57$ MPa, $F_{2c} = 228$ MPa, and $F_6 = 71$ MPa [20]. Due to the high tensile strength, it is expected the rims will allow for a higher operating velocity than the steel rims.

4.3.1 Solid Composite Flywheel

A model of a solid composite flywheel is simulated to compare its energy density to the standard steel flywheel. Its dimensions consist of a 1m diameter and 100 mm

thickness. Figure 4-15 plots the maximum tangential stress of the flywheel at 11000 rpm, which is 312 MPa and below the tensile strength of the composite. The radial stress is shown in Fig. 4-16. As seen in the figure, the maximum radial stress is 35 MPa and occurs at 3/4 of the radius. Since the tensile strength of the composite is 57 MPa in this direction, it is reasonable to assume that initial failure will occur in the radial direction.

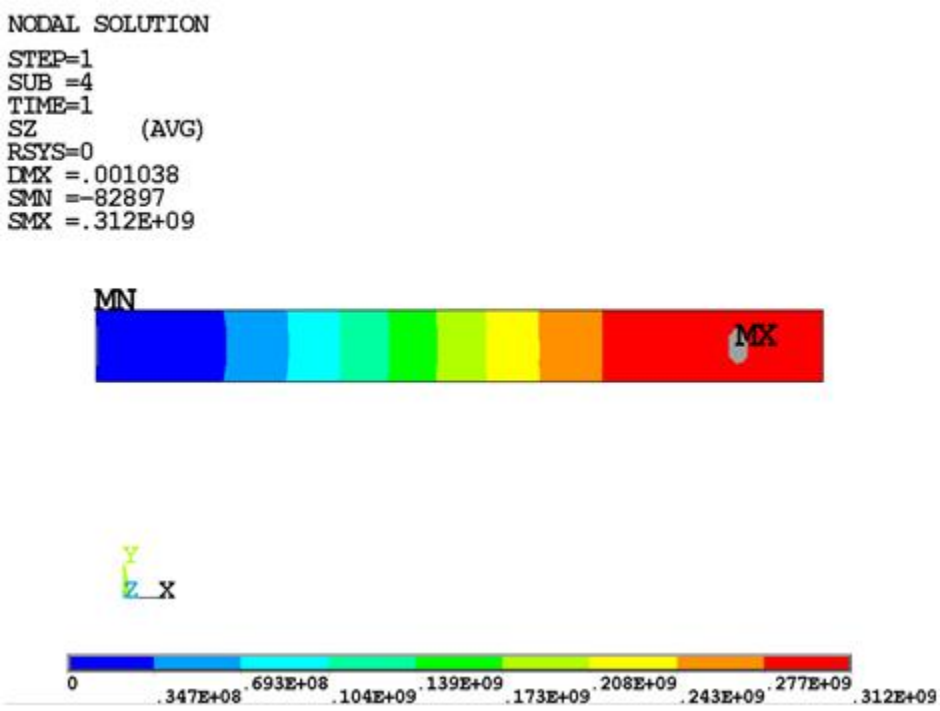

Figure 4-15. Solid composite flywheel tangential stress

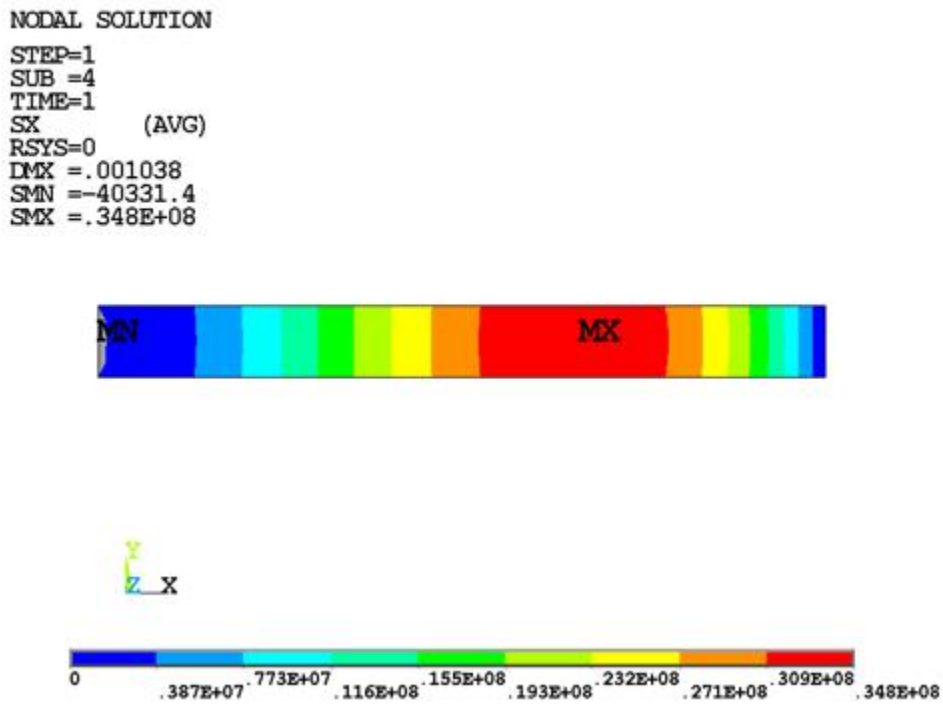

Figure 4-16. Solid composite flywheel radial stress

A plot of the displacements is shown in Fig. 4-17 where the maximum is 1.038 mm at the outer radius. All stresses and displacements are compared with values obtained from the analytical solutions to validate the finite element model. The results for the radial and tangential stress and displacement at the outer radius of the flywheel are listed in Table 4-2. As shown in the table, all percent differences between the ANSYS and analytical model are within 10%. There is a discrepancy in the difference between the displacements of the models which is close the 10%. This may be attributed to the thickness of the flywheel. The solutions derived are from a 2D analytical model.

Once validation of the results is established, the applied angular velocity is increased to determine the maximum specific energy and energy density of the flywheel.

The failure speed is determined to be 14000 rpm due to the resulting maximum radial stress of 56.3 MPa which is close to the tensile strength value of 57 MPa. At this same velocity, the maximum tangential stress is less than 4 times the tensile strength in the major direction at 506 MPa. As stated and shown previously, a solid flywheel of a composite winded in the hoop direction will fail initially in the radial direction due to the low tensile strength present in the material. In order to take advantage of the high tensile strength in the hoop direction and obtain a higher energy density than a conventional flywheel, the radial stresses that occur must be reduced.

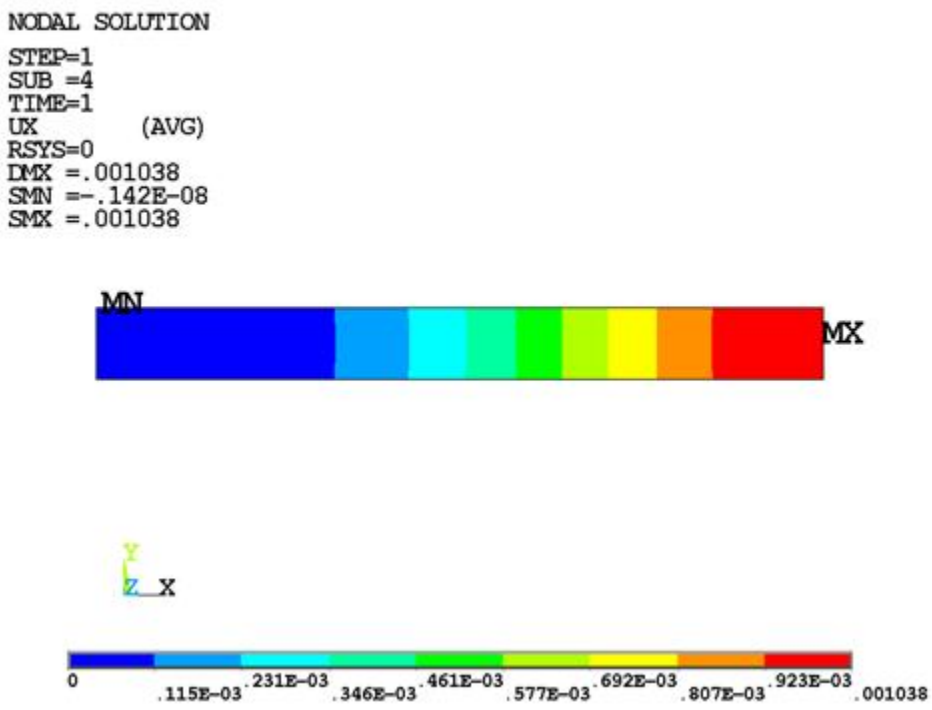

Figure 4-17. Solid composite flywheel radial displacement

Table 4-2. Max stresses and displacements for solid composite flywheel at r_o.

	σ_r (MPa)	σ_t (MPa)	u (mm)
ANSYS	0	279	1.03
Theoretical	0	272.8	0.941
% difference	0	2.27	9.78

4.3.2 Multi-Rim Composite Flywheel

As shown in the previous section, failure in a large solid composite flywheel is dominated by delamination in the radial direction due to the low radial strength of the material. The total diameter and thickness are equal to that of the standard steel flywheel. Due to the number of rims that are analyzed and the wide range in stresses throughout the flywheel, stress values are plotted on a graph versus the radius of the flywheel. All stress values are in Pascal. Figure 4-18 plots the tangential stress throughout the rims. The intial rim has a compressive tangential stress due to the compression it undergoes from each successive rim. Tangential stresses in the rims alternate between a rise in tensile stress and a sharp decline caused by the compression. This pattern continues up to halfway across the radius. Afterwards there is an overall increase in the tangential stress.

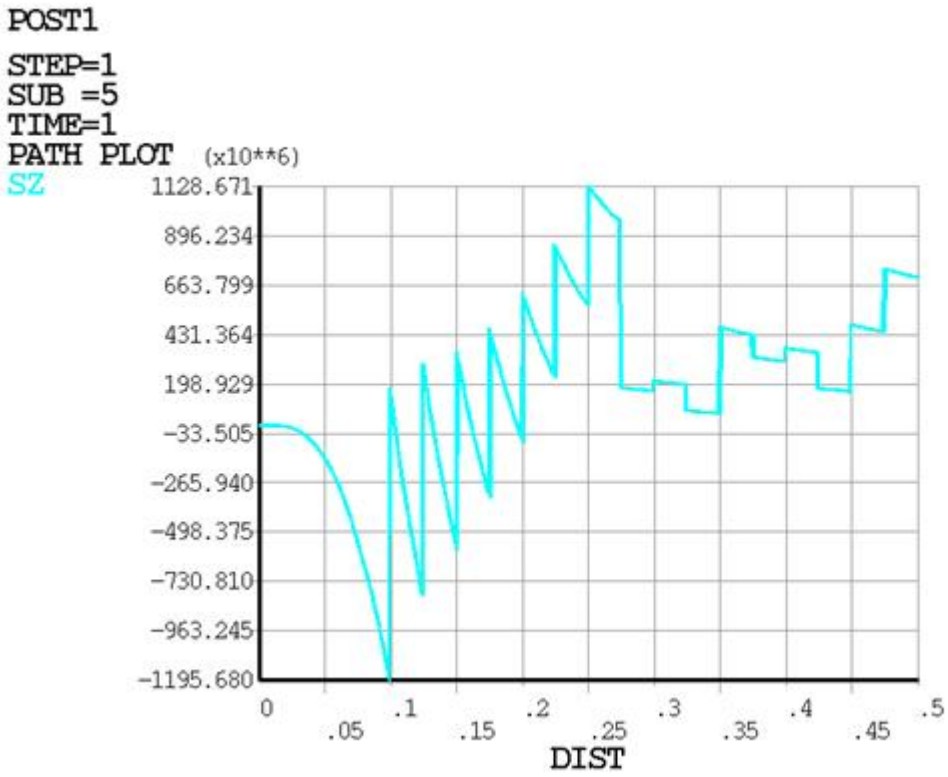

Figure 4-18. Multi rim composite flywheel tangential stress at 11000 rpm

The radial stresses,plotted in Fig. 4-19, show a more even profile and smaller amplitudes compared to the tangential values. As seen in the tangential stress plot, there is sharp decline in the stress for the first rim and each successive rim alternates between tensile and compressive stresses. However the change in stress occurs parabolically. Halfway across the flywheel the radial stresses throughout the rims remain relatively constant.

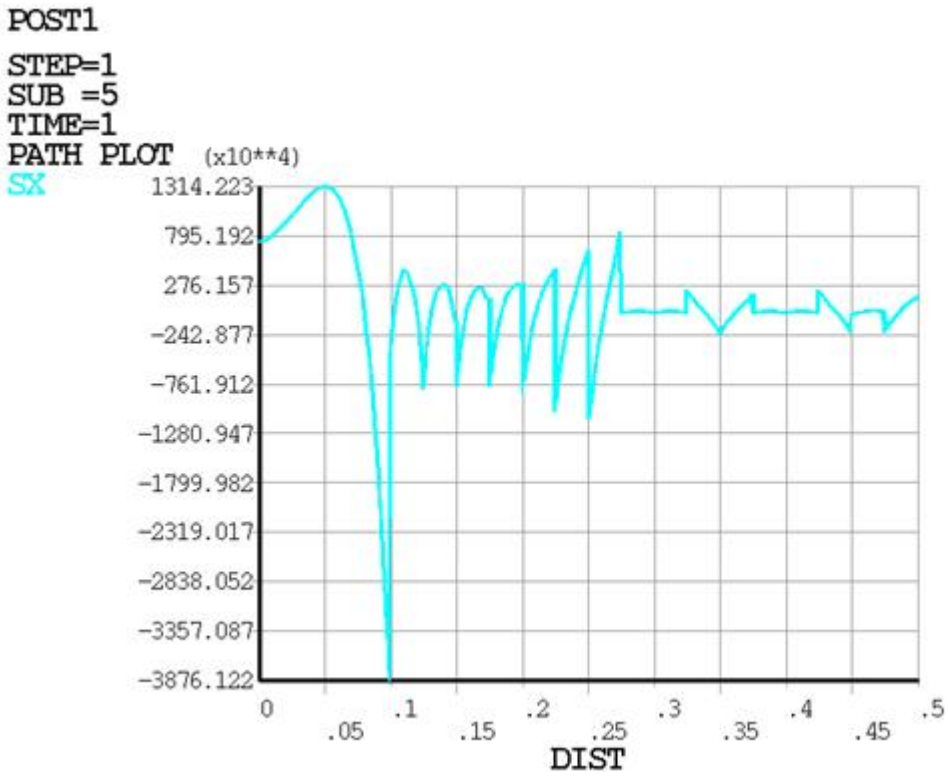

Figure 4-19. Multi rim composite flywheel radial stress at 11000 rpm

In order to determine areas of failure, the Tsai-Wu inverse strength ratio is applied to the rims and plotted in Fig. 4-20. A strength ratio greater than 1 signifies failure. From the figure, rims 2, 3 and 4 from the center of the flywheel fail at their inner radius. It appears the multiaxial stress caused by the compression from the outer rims and the tensile stress from the rotation is greater than the compressive strength of the composite.

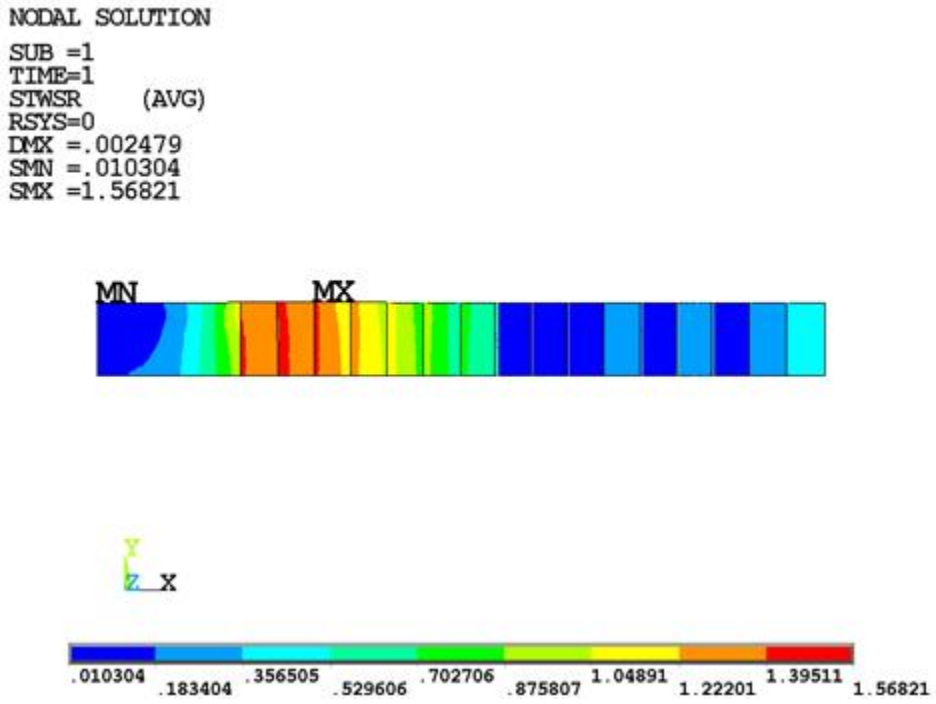

Figure 4-20. Composite rim flywheel Tsai-Wu inverse strength ratio index

4.4 Flywheel with Pressurized Cavity

Figure 4-21 presents the Von Mises stress of the flywheel at 11000 rpm with a pressure of 10 MPa applied at its edges. From the figure it is evident that the reduction in stress from the compression near the inner radius is negligible. Concentration stresses appear at opposite ends of the cavity. Figure 4-22 contains the same results as Fig. 4-21 with a focus on the areas of interest near the cavity. The stresses range from 996 MPa to 2050 MPa where the maximum stress is 2 times greater than UTS and will fail.

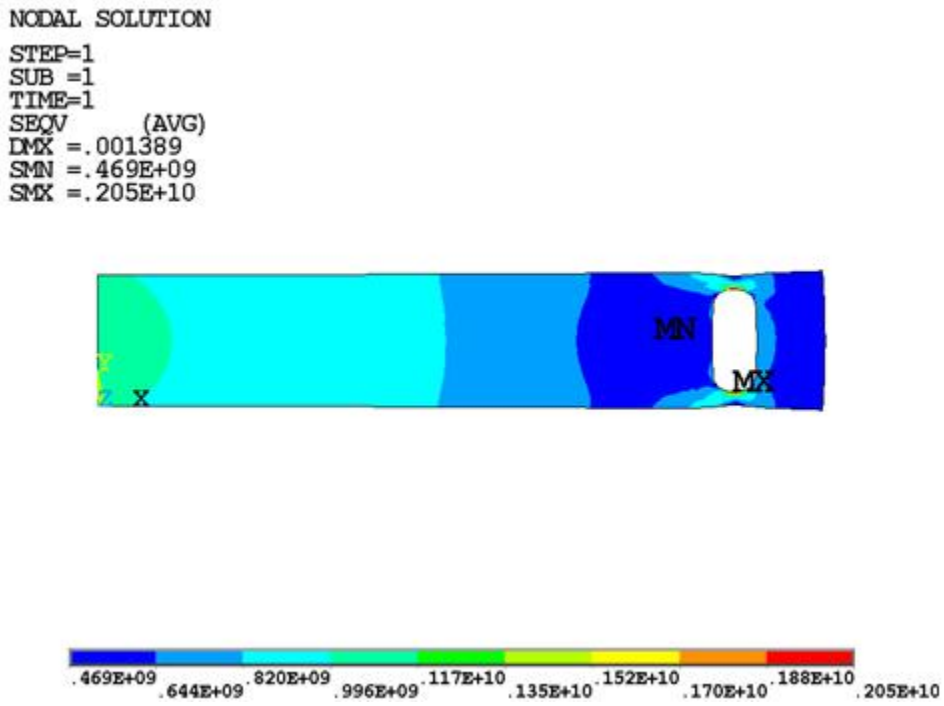

Figure 4-21. Flywheel with pressurized cavity Von Mises stress at 11000 rpm

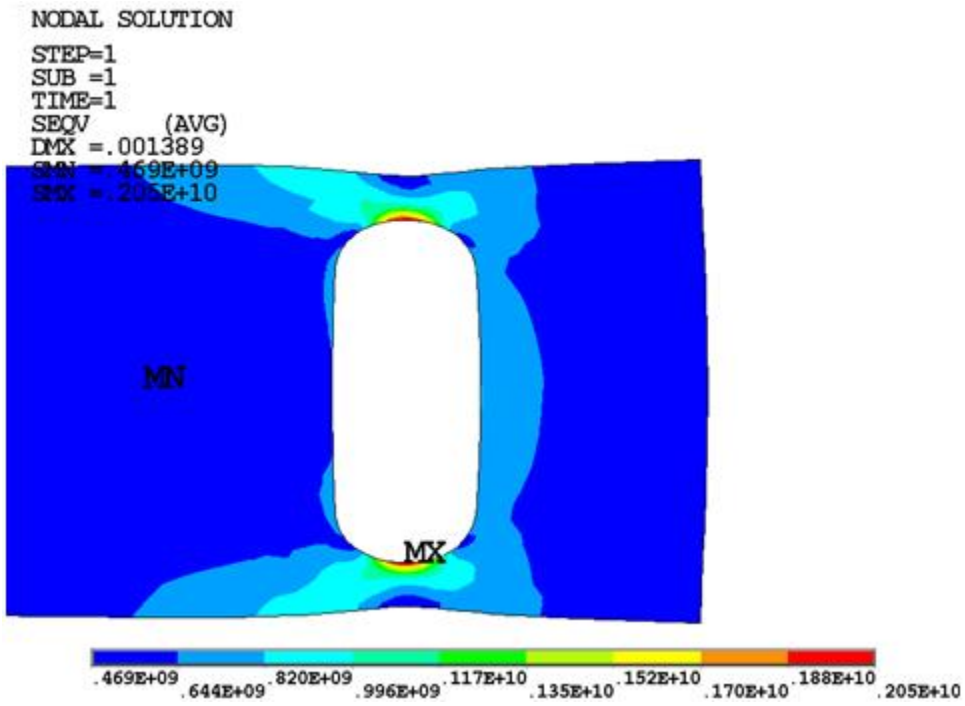

Figure 4-22. Flywheel with pressurized cavity Von Mises stress at 11000 rpm focus

The model is modified by making a smaller cavity closer to the outer radius. By making a smaller cavity and moving its location, it is expected for the nominal stresses to be lower since they are a function of radius. Results show that the concentration stresses decrease, but the pressure has no effect on reducing the stresses near the inner radius and the flywheel still fails. A final model is designed with the cavity close to the inner radius to determine if a higher speed is possible. While the stresses near the inner radius of the flywheel are well below the allowable stress, the concentrated stresses surrounding the ends of the cavity are beyond the failure limit. Employing a pressurized cavity in a flywheel provides the ability to apply the desired pressure without necessity for rims, but the concentration stresses that occur on the cavity are liable to lead to catastrophic failure of the system.

4.5 Welded Steel Wheel

As shown in previous analysis, a steel rim on a steel disk causes greater compression on the disk than a composite rim, but also results in tensile stresses greater than the UTS of the steel rim. It is thought that by imposing an interference fit between a section of the disk and rim and welding the remaining area the discontinuity in the stress can be reduced or eliminated.

Initially a disk with a rim is modeled with a bonded (always) contact to ensure the contact is creation is correct. If the modeling is accurate, the stress and results are expected to be the same as a solid steel flywheel. Figures 4-23 to 4-26 show the stresses and displacements for the welded flywheel. All the values are in accordance with those obtained from the simulations for a solid steel flywheel and the modeling of the welding is considered accurate.

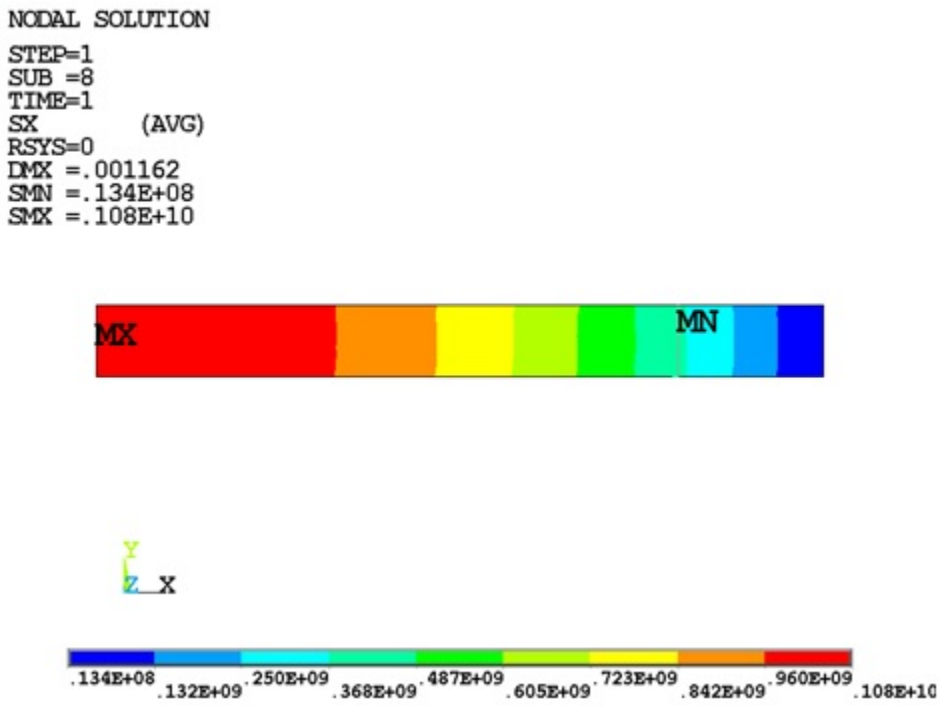

Figure 4-23. Welded flywheel radial stress

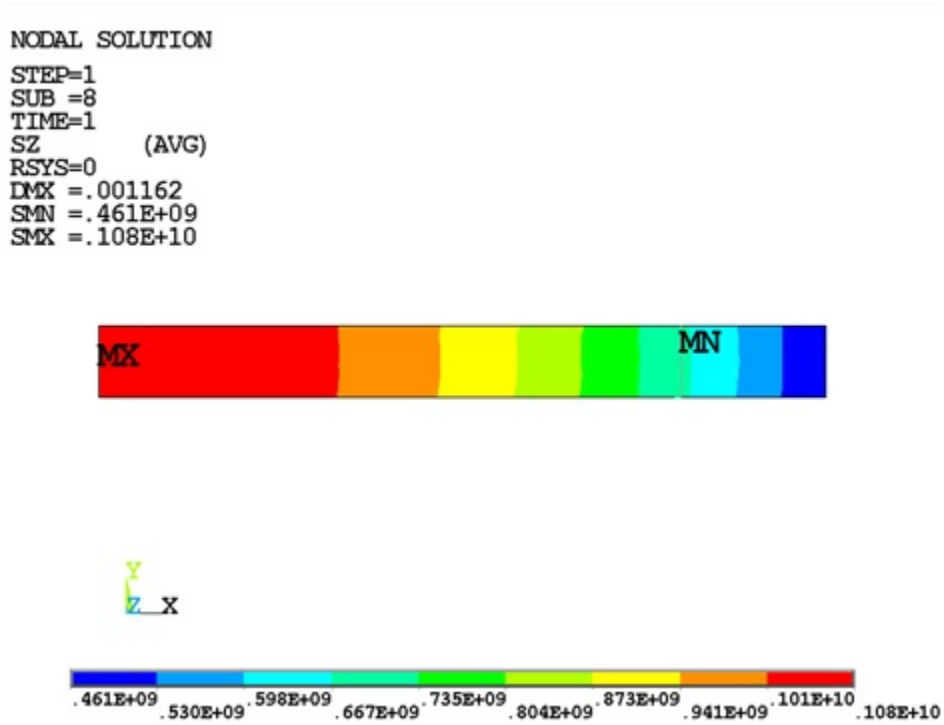

Figure 4-24. Welded flywheel tangential stress

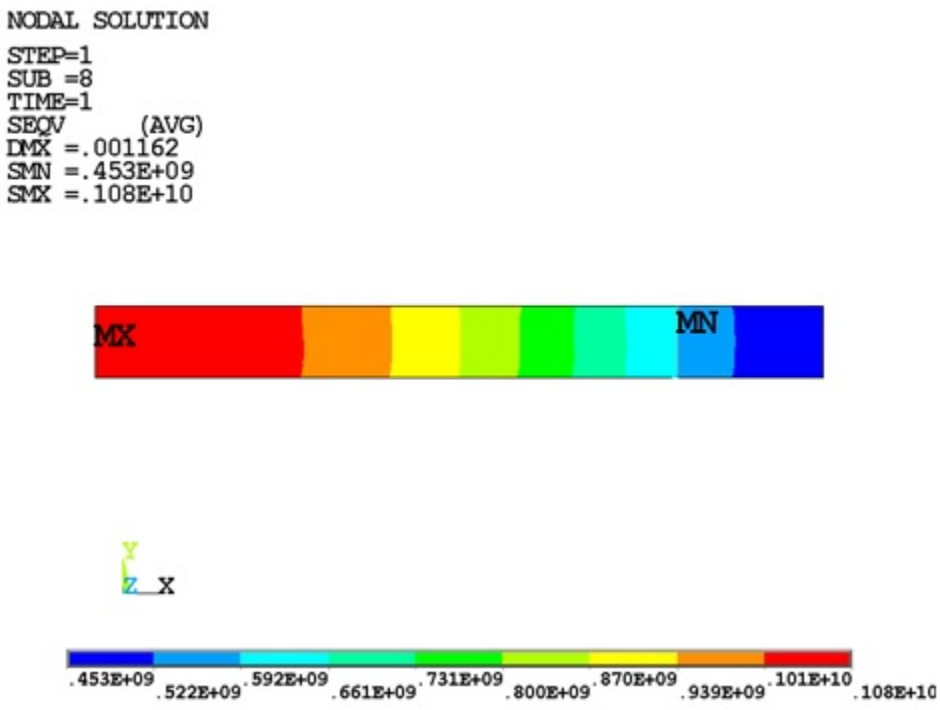

Figure 4-25. Welded flywheel Von Mises stress

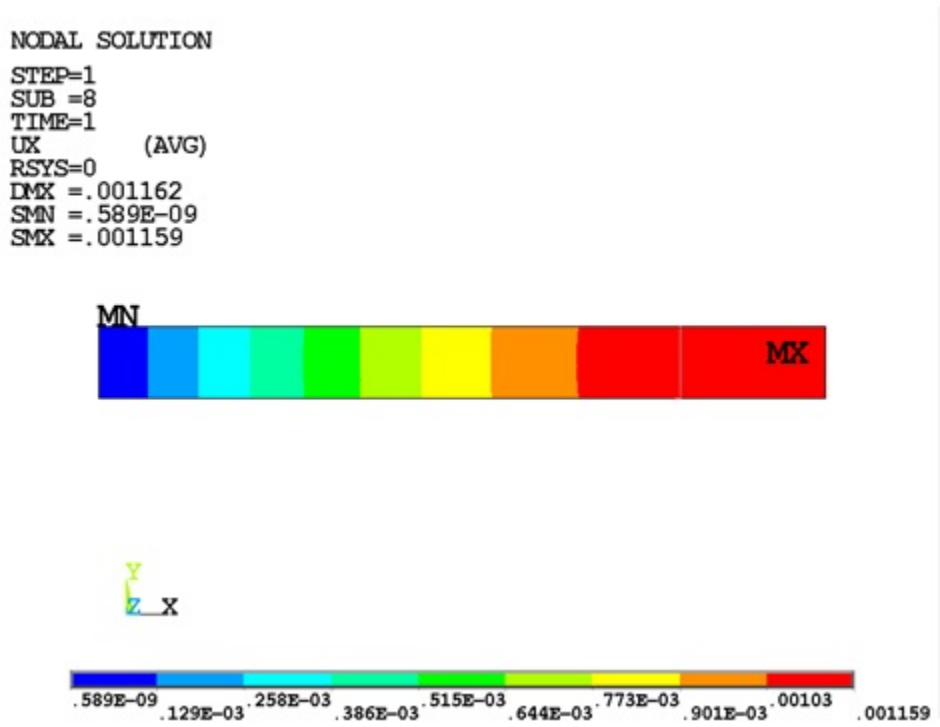

Figure 4-26. Welded flywheel radial displacements

Figure 4-27 shows the Von Mises stresses at 11000 rpm. The large stresses occur at the corners of the bonded contacts. This is due to the FEA software and the sharp corners and does not represent a realistic scenario. To determine if failure is likely to occur in the flywheel, the maximum stress is limited to 1080 MPa. Stresses above that value are considered to lead to failure in the components. Figure 4-28 shows the plot of the Von Mises stress with the limited maximum stress. It is evident that there is a large area of failure both in the bonded-interference section and the outer rim. The effect of the interference between the disk and rim shifts the failure area and high stresses from the inner radius to the outer.

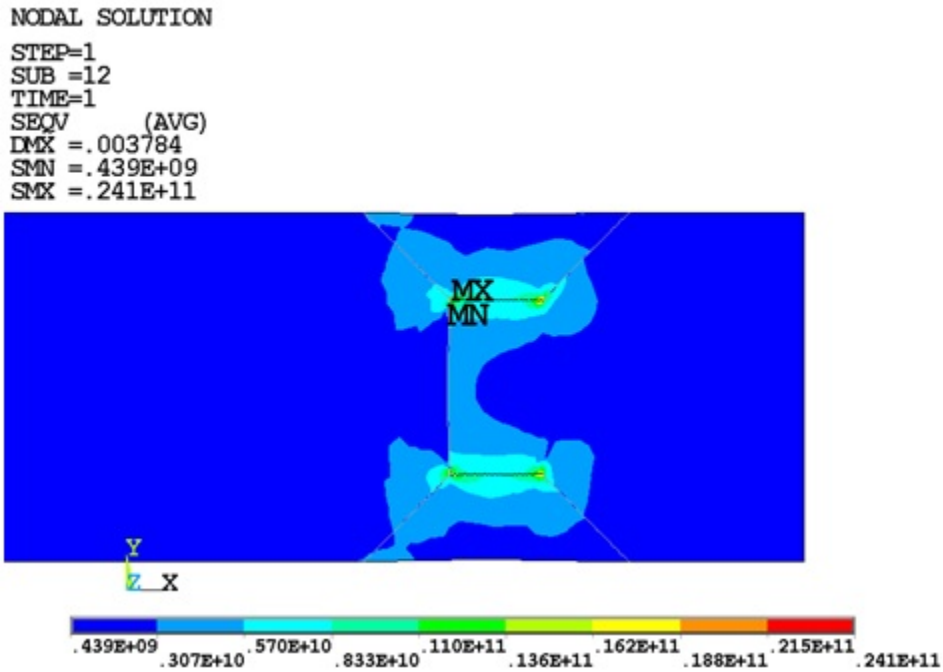

Figure 4-27. Welded steel flywheel with internal press fit 3 mm interference Von Mises stress

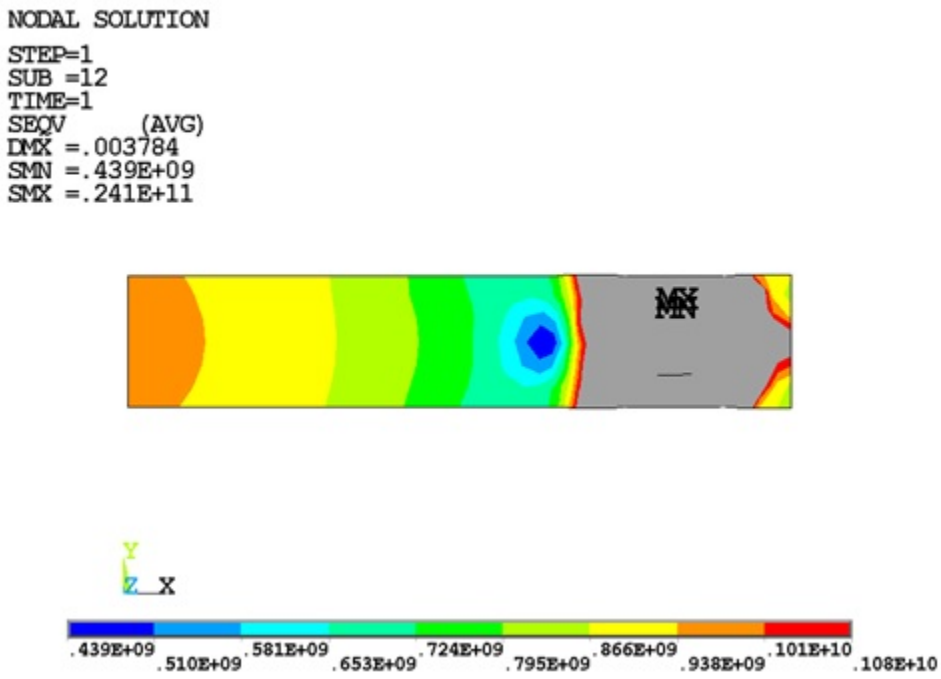

Figure 4-28. Welded flywheel with internal press fit 3 mm interference Von Mises stress (adjusted)

Further modifications are made to the model to determine if the stresses near the outer radius can be reduced while maintaining the compression. The models are designed with interferences of 1mm and 2 mm. Figure 4-29 plots the Von Mises stress for the flywheel with a 2 mm interference at 11000 rpm. As expected there is a reduction in the compression on the disk and the tensile stresses of the outer rim, but the same area fails as in the previous simulation. The same trend in the results occurs in the 1 mm interference simulation. While it is possible to further reduce the interference, the resulting compression would be negligible and the area of concern will still fail.

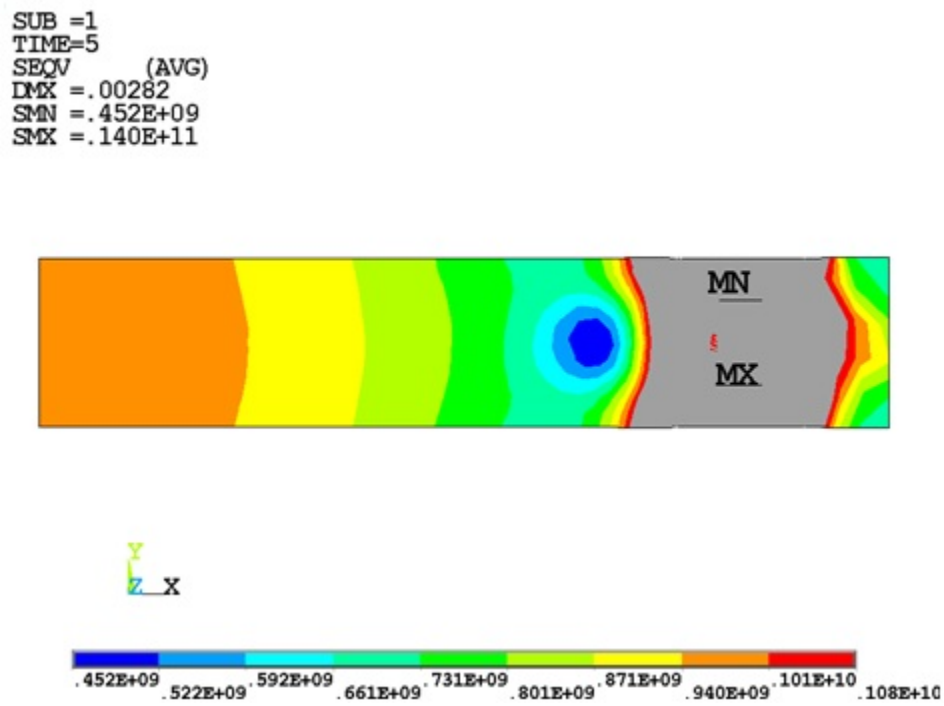

Figure 4-29. Welded flywheel with internal press fit 2 mm interference Von Mises stress (adjusted)

4.6 Shape Optimization

The geometry of a flywheel affects the stress magnitude and profile across its length. A higher energy density can be achieved by distributing the stresses evenly throughout the flywheel with a minimal increase in mass. Various flywheel designs are analyzed to determine if the energy densities can be increased by modifying the geometry of the standard flywheel. The energy, specific energy, and energy density are calculated and tabulated for ease of comparison.

The first shape modification consists of the conical flywheel shown in Fig. 4-30. Thickness values range from 0.075 m to 0.05 m with the largest thickness at the center of the flywheel. The transition from the center of the flywheel to the outer

radius is modeled as a linear taper. A thicker flywheel is expected to have lower stresses due to the presence of available additional material for load distribution.

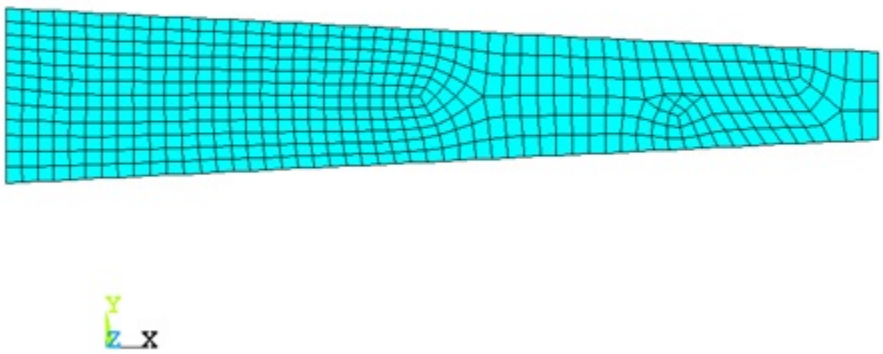

Figure 4-30. Conical flywheel model

Figures 4-31 to 4-33 are stress plots for the conical flywheel model at 11000 rpm. It is apparent that all the stresses have a significant reduction in their peak values relative to the standard flywheel geometry, as expected. The maximum stresses are 200 MPa below the stresses present in the standard flywheel. While the radial stress has a similar distribution as the standard geometry, the tangential and Von Mises show a different stress profile than the previous model. The high stress area decreases for both stresses with the Von Mises plot showing a particularly small area of concern. After calculating the specific energy and energy density for the conical

flywheel at 11000 rpm, the speed is increased until failure to determine its maximum operating speed, specific energy, and energy density.

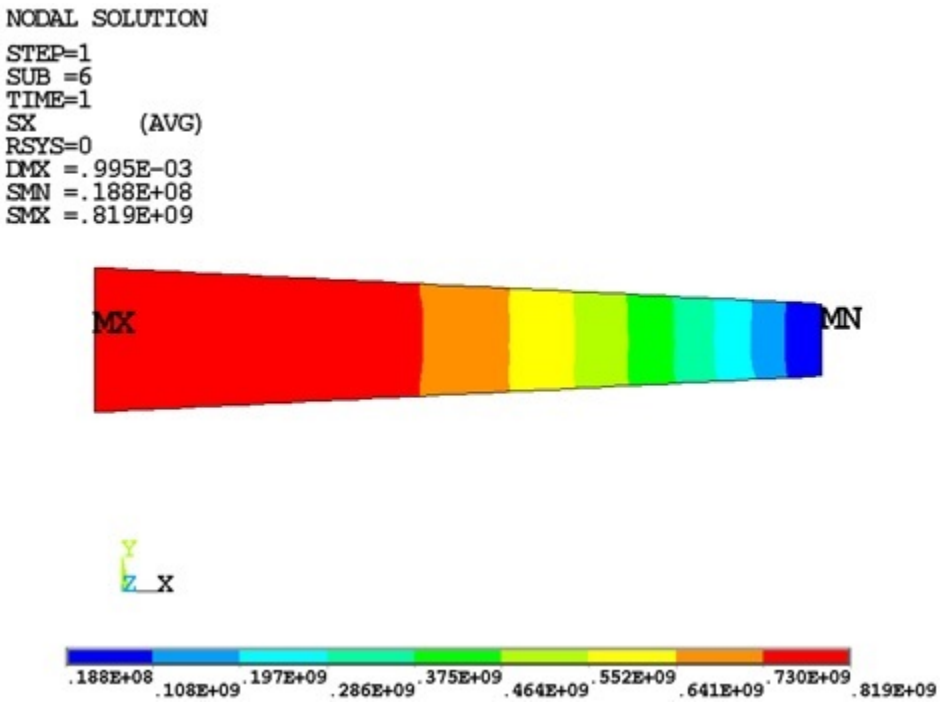

Figure 4-31. Conical flywheel radial stress at 11000 rpm

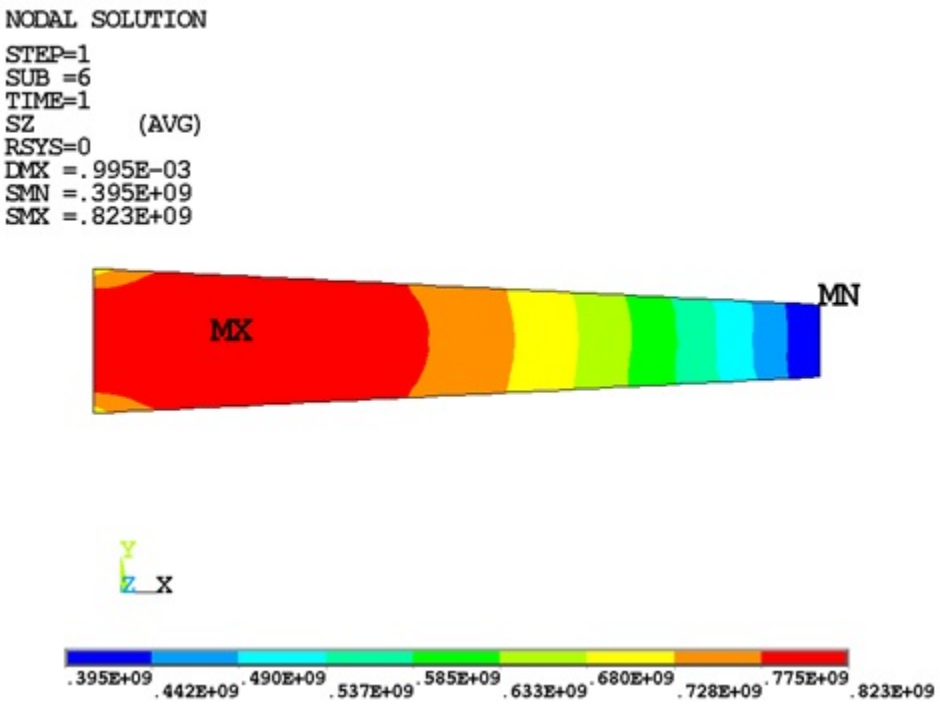

Figure 4-32. Conical flywheel tangential stress at 11000 rpm

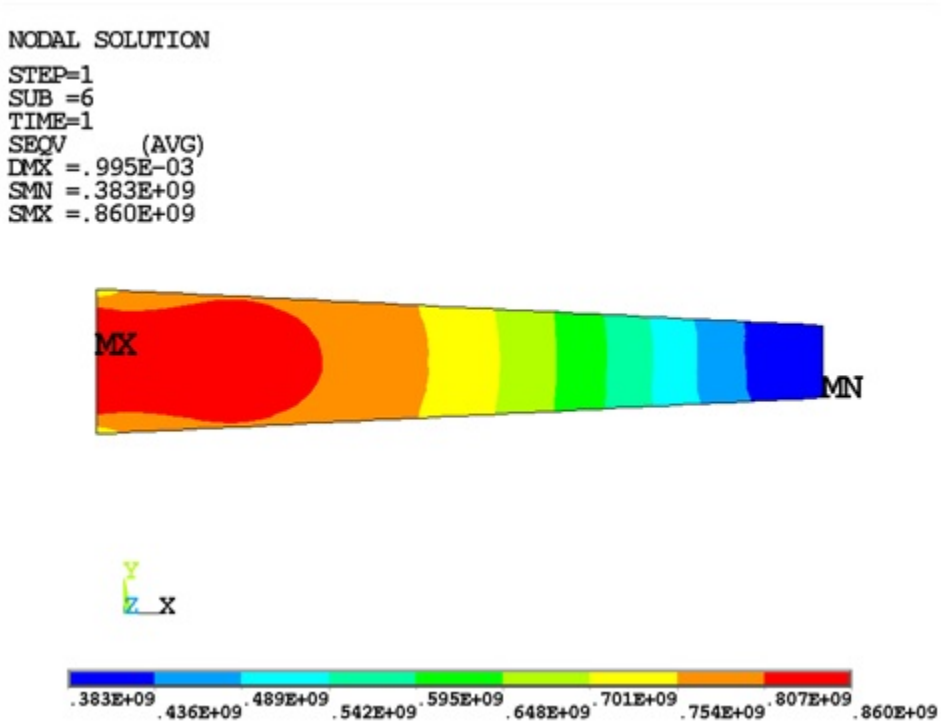

Figure 4-33. Conical flywheel Von Mises stress at 11000 rpm

12000 rpm is taken to be the maximum operating speed before failure occurs. The result for the conical flywheel Von Mises stress is plotted in Fig. 4-33 to compare with the results at 11000 rpm. There is an average increase in all the stresses of 100 MPa, but the peak stresses are at or below the UTS of the material. As in the previous results, the stress profile for the tangential and Von Mises stress is different than the standard geometry model.

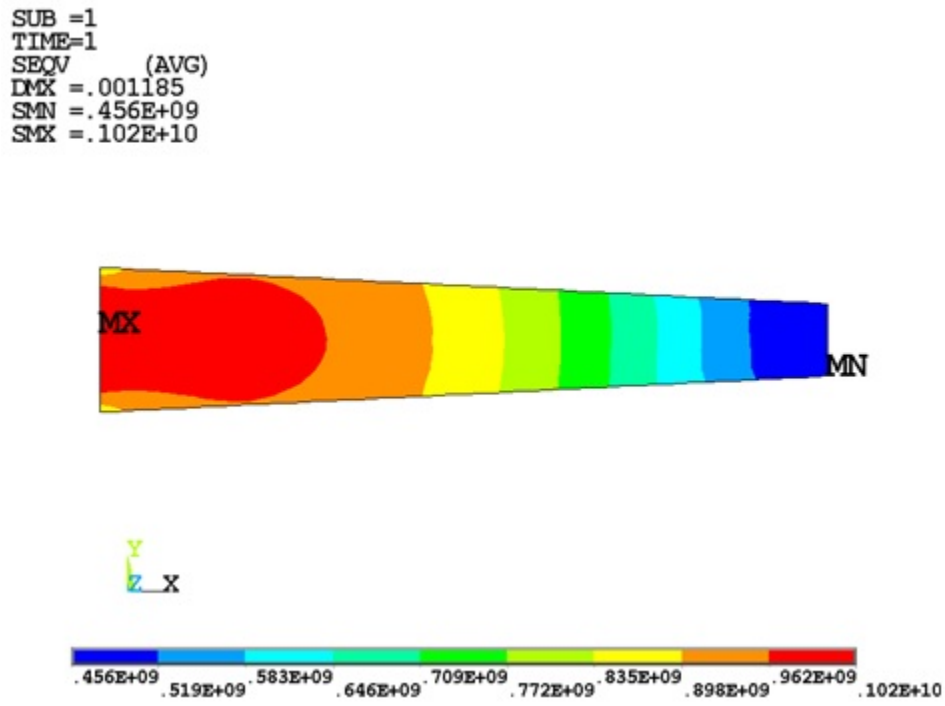

Figure 4-34. Conical flywheel Von Mises stress at 12000 rpm

Initially a model with a step in its geometry is made to determine the ideal transition location. The ideal location should have low nominal stresses in the transition area and provides compression to the center of the flywheel. After several simulations, the transition location is chosen to occur halfway across the flywheel radius. Figures 4-35 to 4-37 show the radial, tangential, and Von Mises stress for this particular model at an operating speed of 11000 rpm. As seen in the figures, the stresses at the center of the flywheel are lower than the standard flywheel. A stress concentration is visible at the corner of the transition edge and is attributed to the sharp corner present which will not exist in a true physical model. For the current analysis, the stress concentration is dismissed in order to test the viability of the application of pressure at the transition edge. In future designs, rounded corners

are applied to the model to reduce the concentration stress.

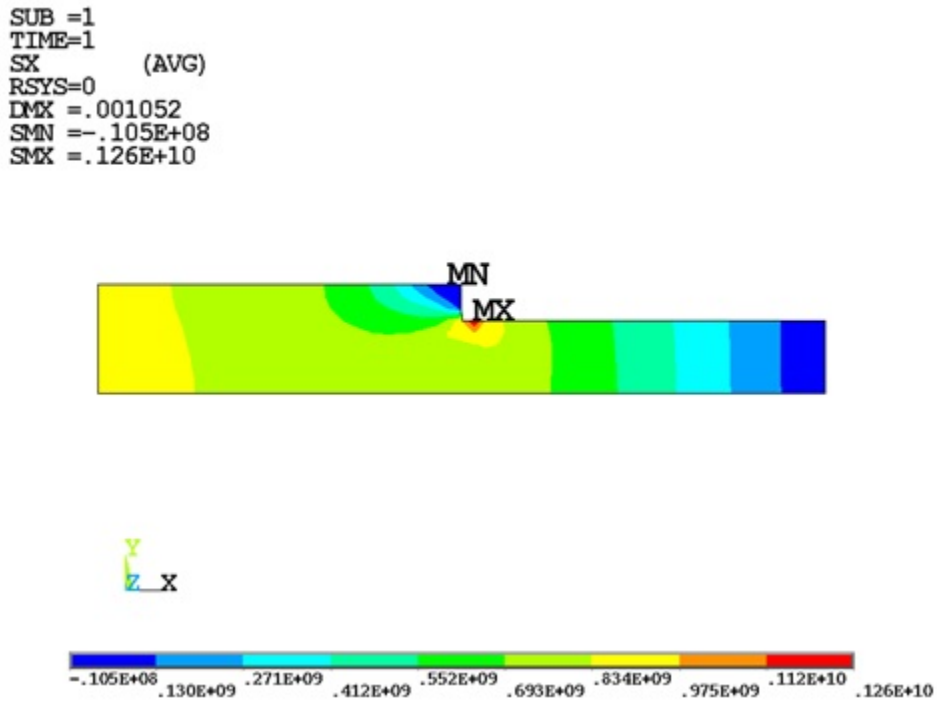

Figure 4-35. Stepped flywheel radial stress

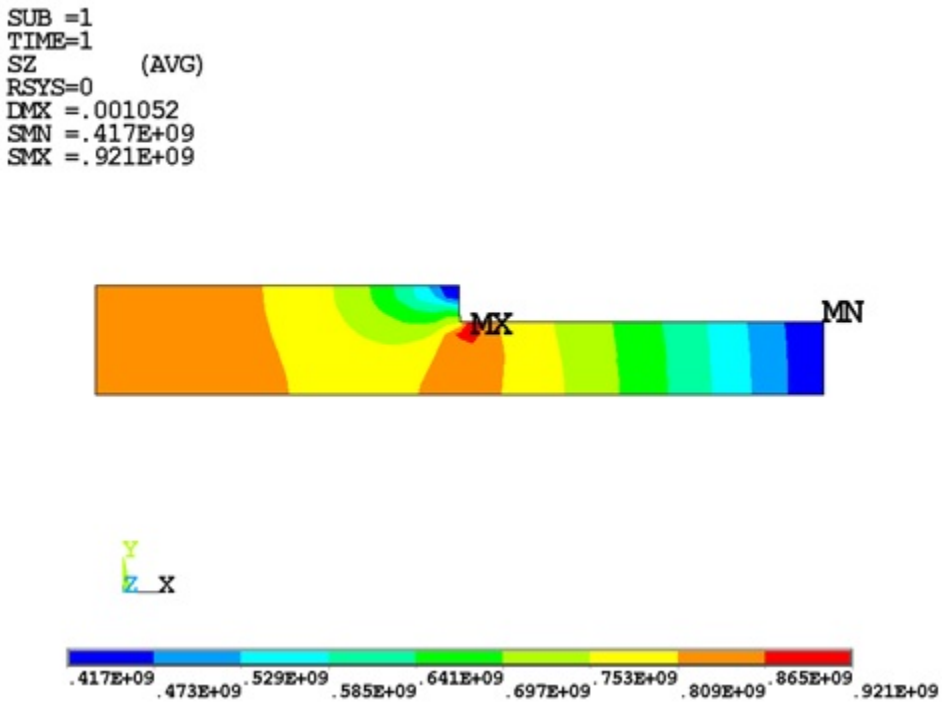

Figure 4-36. Stepped flywheel tangential stress

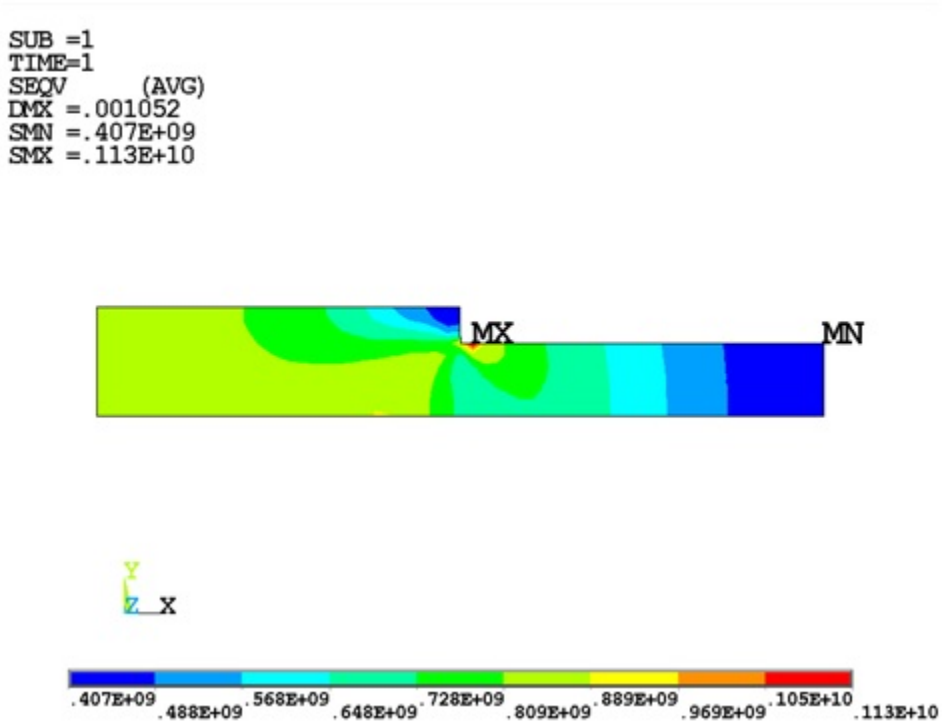

Figure 4-37. Stepped flywheel Von Mises stress

4.7 Stepped Flywheel with Pressure

Using the stepped flywheel model from the previous section, a pressure is applied at the transition edge to determine if the compression has a noticeable effect in reducing the high stresses at and around the center of the flywheel.

A pressure of 500 MPa is applied to the model operating at a speed of 11000 rpm. Results are shown in Figs. 4-38 to 4-40. The plots for all 3 stresses show the values at the initial area of concern to be greatly reduced. The stress concentration present at the transition corner is visible as in the previous section. However the intent of the current simulation is simply to establish if an applied pressure reduces the stresses at the center of the flywheel.

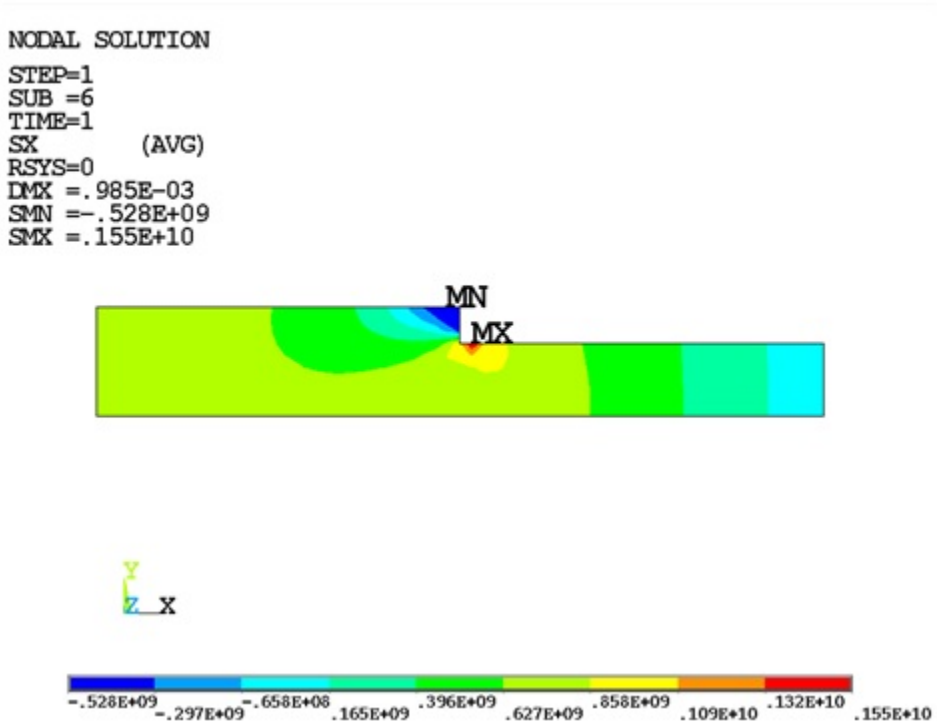

Figure 4-38. Stepped flywheel with pressure radial stress

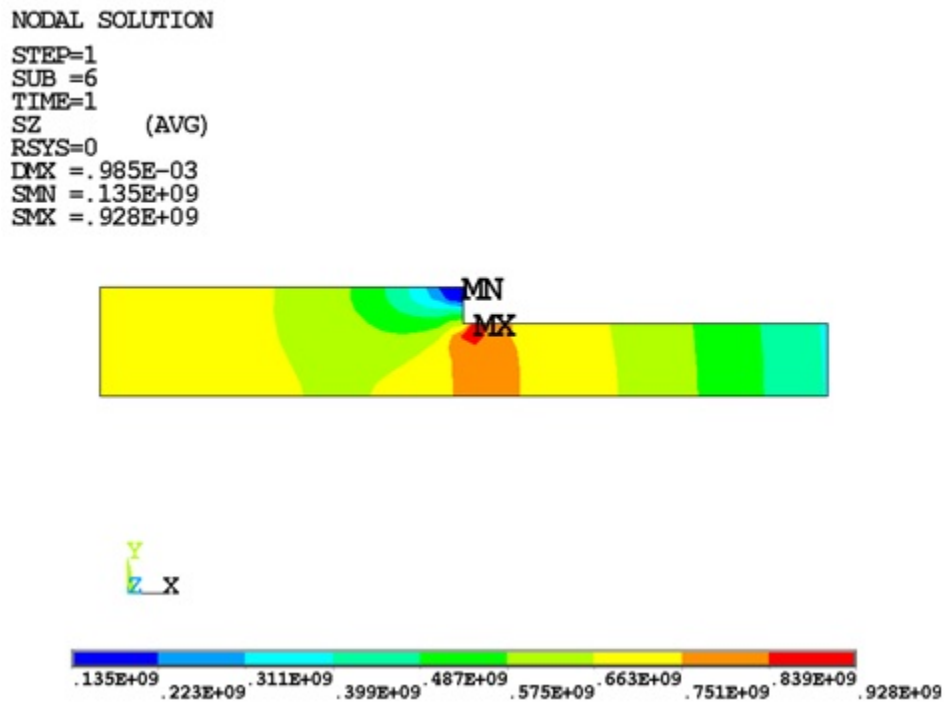

Figure 4-39. Stepped flywheel with pressure tangential stress

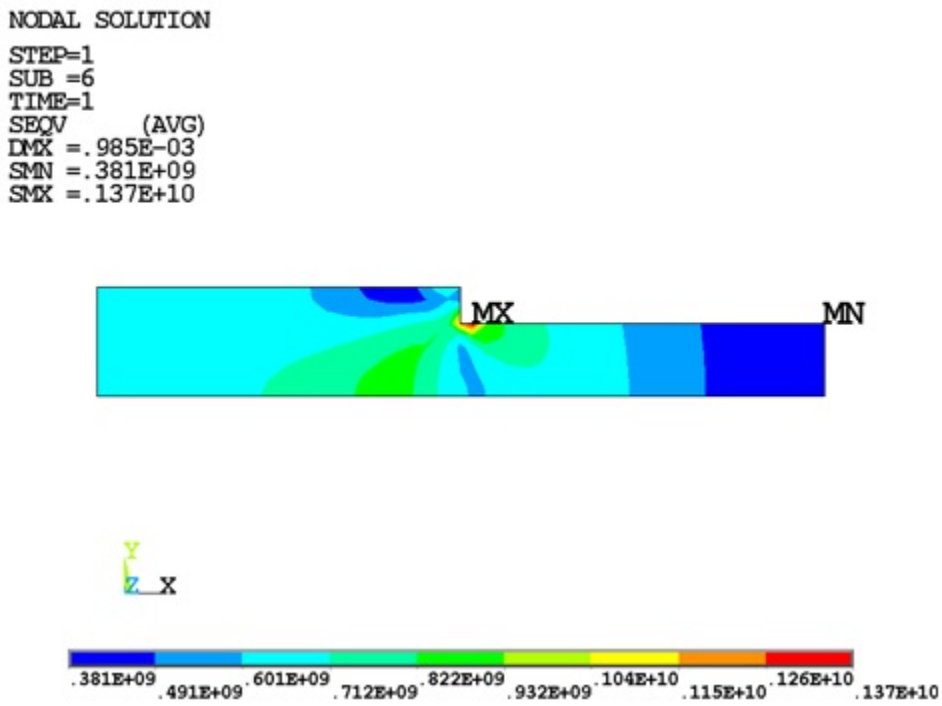

Figure 4-40. Stepped flywheel with pressure Von Mises stress

4.8 Rotor with Collar Flywheel

As shown in the previous section, a change in flywheel geometry leads to a change in the stress values that occur at a given speed. Depending on the modification, it may also lead to a reduction in stresses. The rotor-collar configuration employs both the geometry modification and compressive stress associated with interference from a rim. Figure 4-41 shows the diagram for the standard rotor-collar flywheel model. In the following sections various sections of both the rotor and collar are modified.

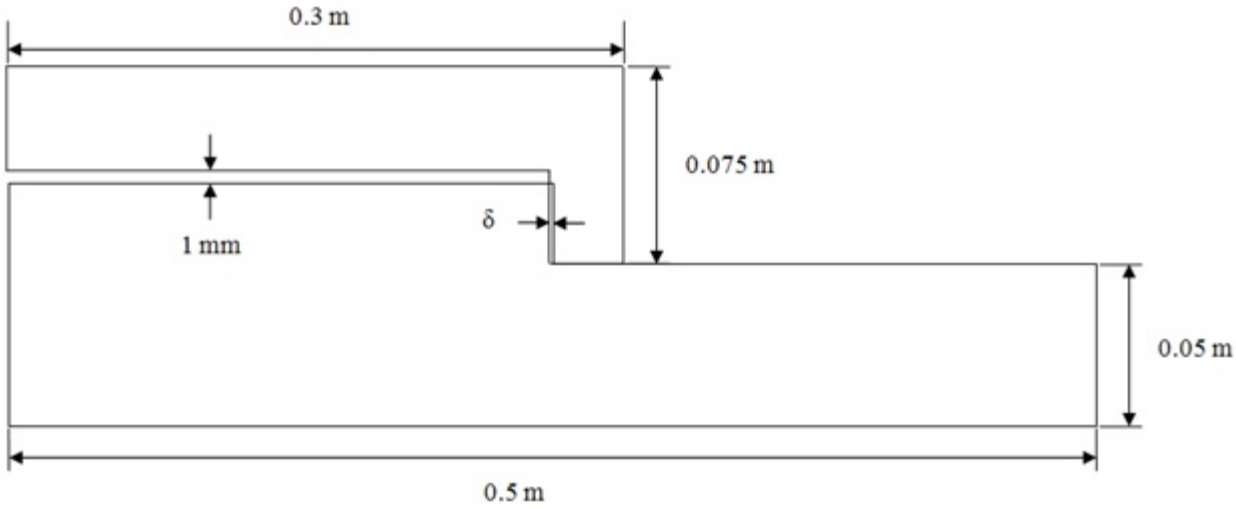

Figure 4-41. Rotor-Collar flywheel diagram

The initial simulation consists of a 1 mm interference between the collar and the rotor with no taper with an angular velocity of 11000 rpm. Results of the various stresses are shown in Figs. 4-42 to 4-44. The maximum stress of the displayed values is limited to 1080 MPa in order to highlight the areas of concern.

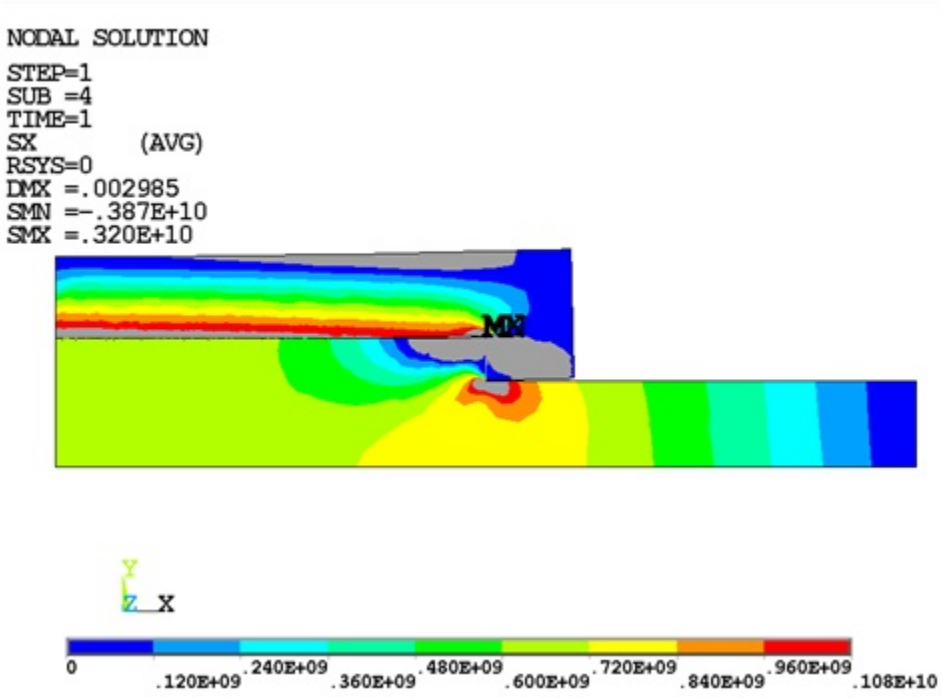

Figure 4-42. Standard rotor-collar flywheel radial stress

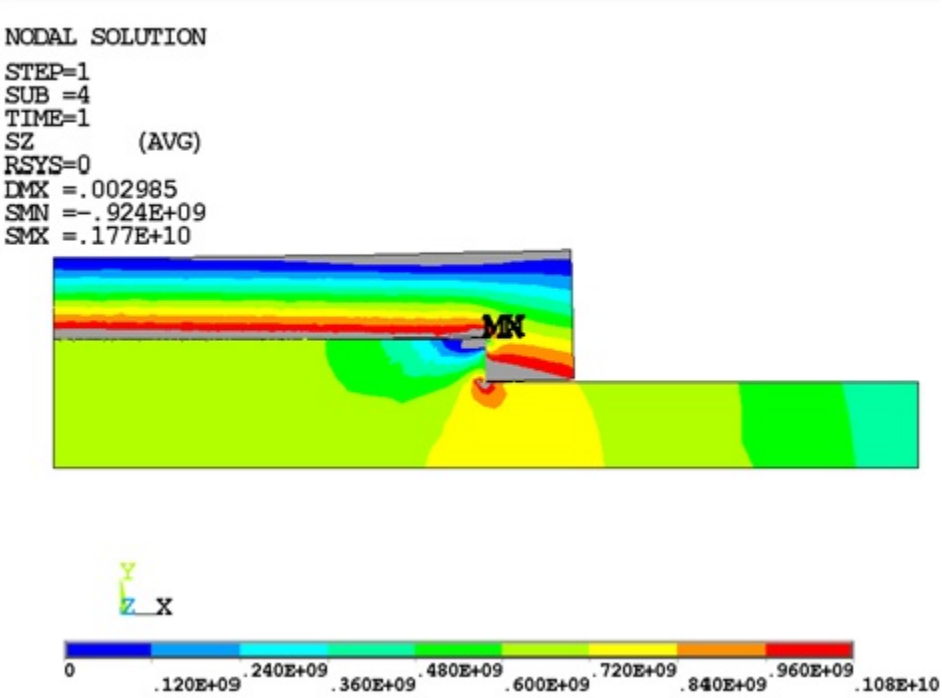

Figure 4-43. Standard rotor-collar flywheel tangential stress

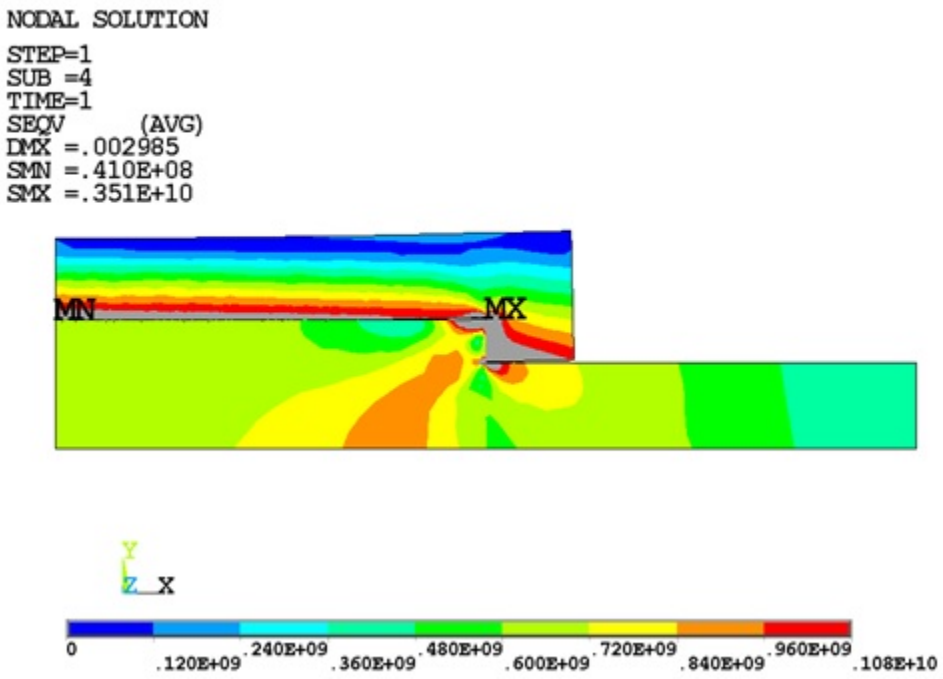

Figure 4-44. Standard rotor-collar flywheel Von Mises stress

Several stress concentrations are present in the components of the flywheel in all 3 stress plots. High stress magnitudes occur at the corners of the rotor transition edge. By applying rounded edges, the stress concentration should decrease or be removed entirely. The areas of the collar consist of the interference section and the edges adjacent to the rotor. These sections undergo stresses beyond the UTS of the steel. The sharp corners appear to cause high stress concentrations in both the collar and rotor. In order to determine the effect of the corners on the stresses, the contact pressure is analyzed and plotted in Fig. 4-45. From the figure it is evident that the radial growth and bending of the collar leads to a loss of contact in the lower half portion of the interference area and a large stress concentration at the upper corner. The maximum occurs and appears to be the largest contributor to failure in the collar. Following sections document the modifications applied to the interfering area

to improve the contact profile while reducing the stresses in the collar.

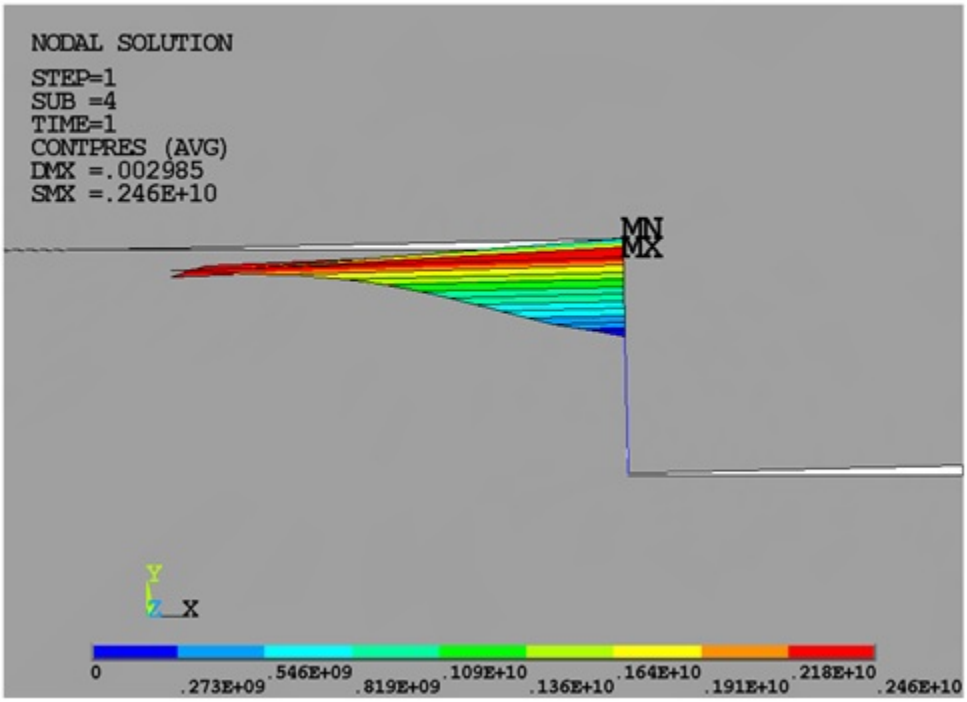

Figure 4-45. Standard rotor-collar flywheel contact pressure

4.8.1 Tapered Contact Area

The first attempt at obtaining a more preferable contact pressure profile consists of a linear taper applied to both the rotor and collar. Taper angles are varied to find the range and the maximum angle in which the collar retains the interference with the rotor during operation. The operating angle range is found to be 0°-45°. Angles larger than 45° result in the collar sliding off the rotor and loss of interference. As shown in the previous section, the collar tends to grow and bend outward. To counteract that effect while improving the contact pressure, the taper on the rotor and the collar are modeled at different angles. This is due to the tendency of the

collar to slide off when the angle is greater than 0 and similar to that of the rotor.

A parametric study is conducted for the taper contact area. The change in the rotor angle and interference length in regards to the normalized transition length is determined. The collar angle is maintained constant at 25°. Figure 4-46 plots the change of the rotor angle at various transition lengths for interferences between 0.25-1.5 mm. From the figure it is evident the angle changes are similar for all interferences up to a transition of 0.7. Afterwards the difference becomes more visible for the various interferences. The change in angle has an exponential growth with respect to the normalized transition length.

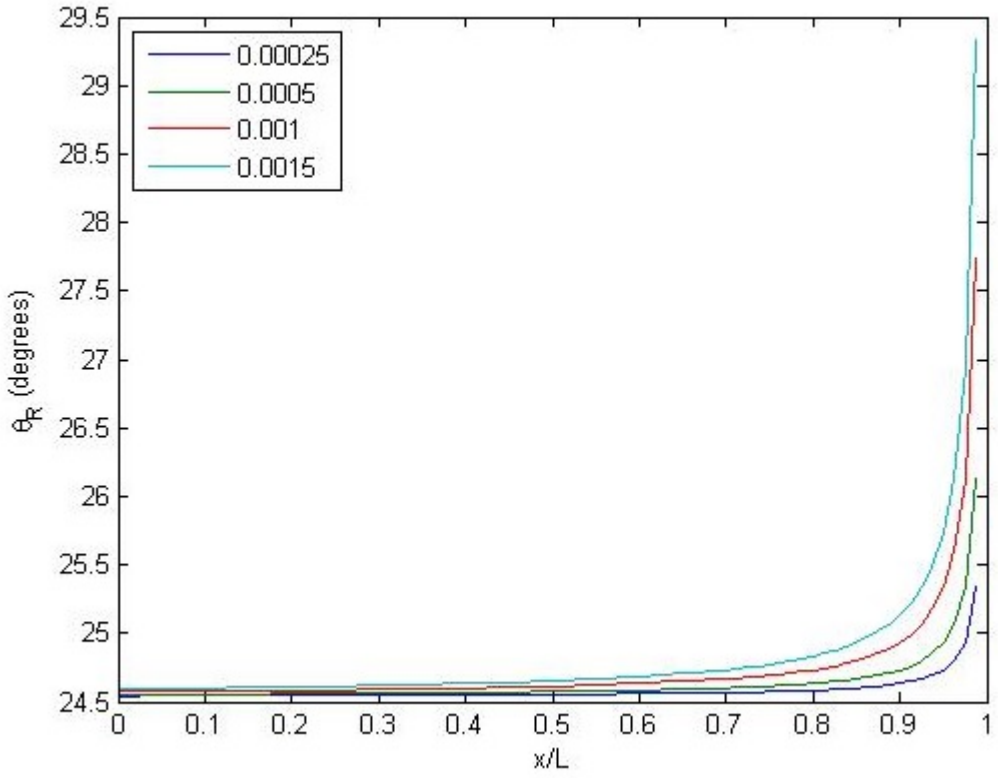

Figure 4-46. Collar angle vs transition length

The results for the parameterization study of the interference length with respect to the transition length are shown in Fig. 4-47. The change in the upper interference length occurs in a similar manner as the angle of the rotor. There is an exponential growth with respect to an increase in the transition length and the angles are close in values up to the 0.7 normalized transition length.

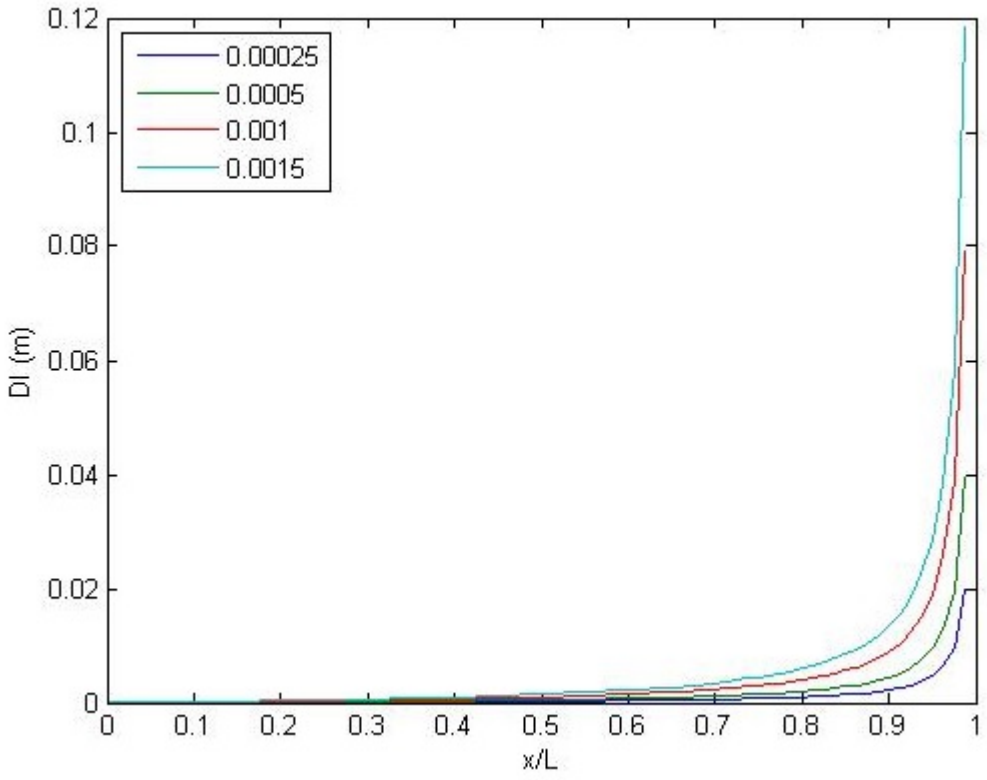

Figure 4-47. Interference length vs transition length

Using the parameterization model shown in a previous section, an interference of 1 mm is applied at the lower portion with that of the upper portion varied from 0.25 and 0.75. The interference pair that results in the most preferable contact profile is

found to be 0.5 to 1 mm. Figure 4-48 shows the resulting contact pressure at 0 rpm. While there a stress concentration exists at the bottom corner, the maximum value is about half the value of a 0 interference.

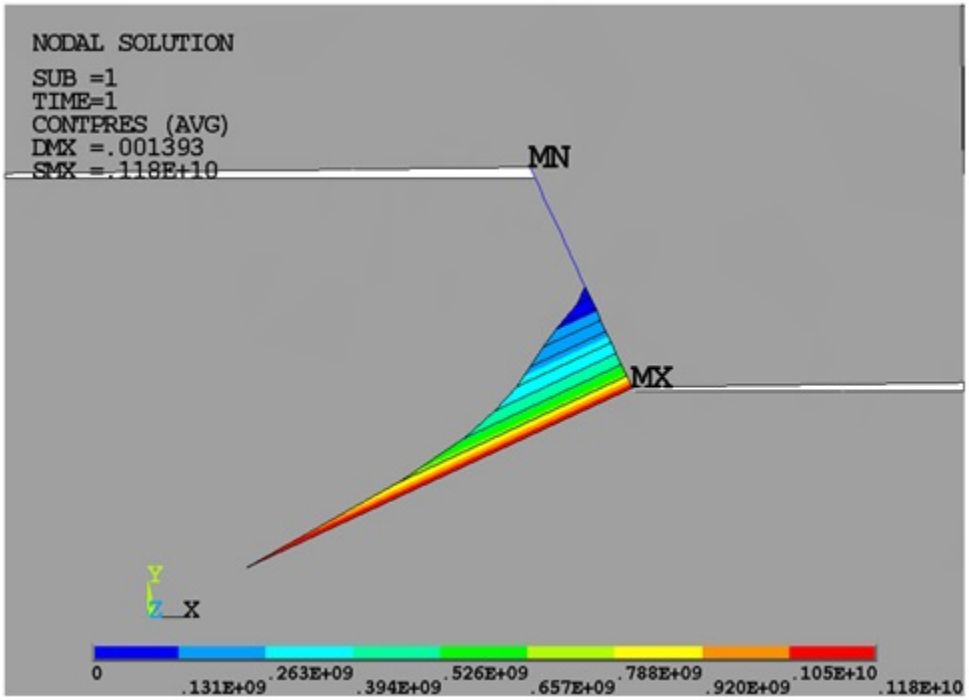

Figure 4-48. 25° Rotor and collar contact pressure at 0 rpm

An angular velocity of 12000 rpm is applied to the model to observe the contact profile during high speed operation. The resulting contact pressure is shown in Fig. 4-49. The bending of the rotor during operation causes the contact to occur across the entire contact area. However the contact pressure applied decreases from the corners to the center of taper area. This appears to occur to the reduced interference, outward growth, and bending of the collar. While the upper corner has a lower interference, it increases when bending occurs due to the upper corner of the rotor.

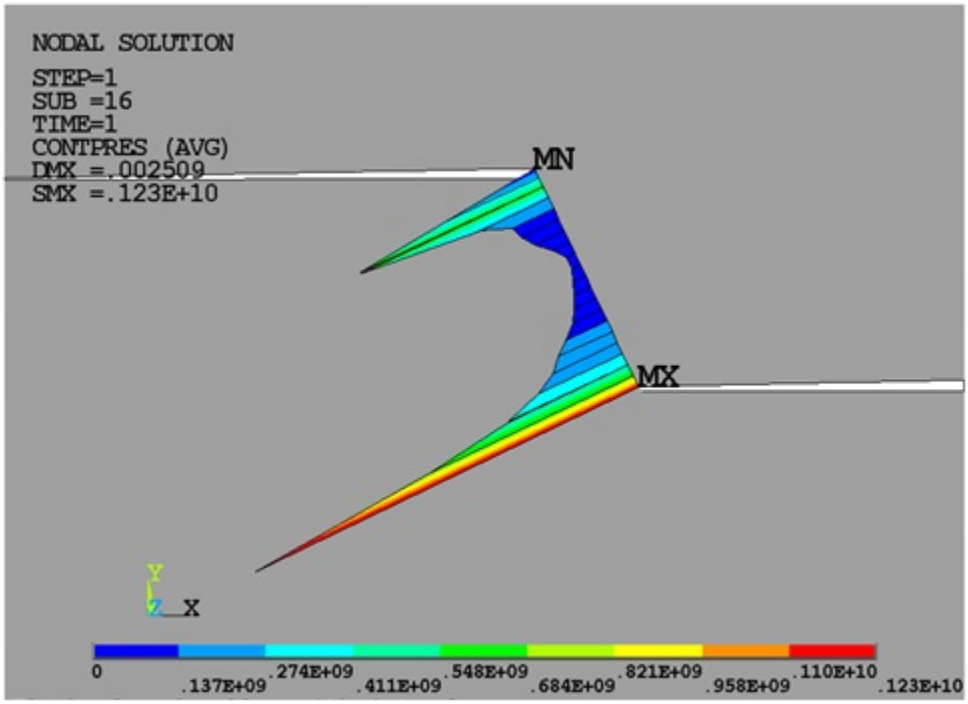

Figure 4-49. 25° Rotor and collar contact pressure at 12000 rpm

4.8.2 Curved Tapered Contact Area

Flywheel models with varied tapered contact areas show favorable contact profiles when static and during high speed operation. Results from the previous section show that contact increases with angular velocity, but the center of the contact area undergoes the minimum amount of compression. One proposed method to increase the pressure at the area of interest is to apply a slight curve to the tapers. It is expected for the pressure profile to be distributed more evenly during operation. Initially the tapers are made to curve inwards towards the rotor. However this leads to high concentration stresses beyond the UTS of the steel. A more favorable pressure profile is achieved by modeling the curved tapered surfaces outwards. In addition to varying the angle of the tapers, the curvature is increased from the standard

linear taper. The model chosen to investigate the effect of the curve on the contact pressure consists of a flywheel with a 30° taper and a collar with a 29° taper. Both sections have a similar curve applied. Figure 4-50 shows the resulting contact profile at 0 rpm. There appears to be a reduction in contact area and an increase in the compression from a linear taper. To further understand the effect of angular velocity on this particular contact profile, a velocity of 12000 rpm is applied to the model. The resulting contact profile is shown in Fig. 4-51. It is evident the contact profile increases in contact area with speed.

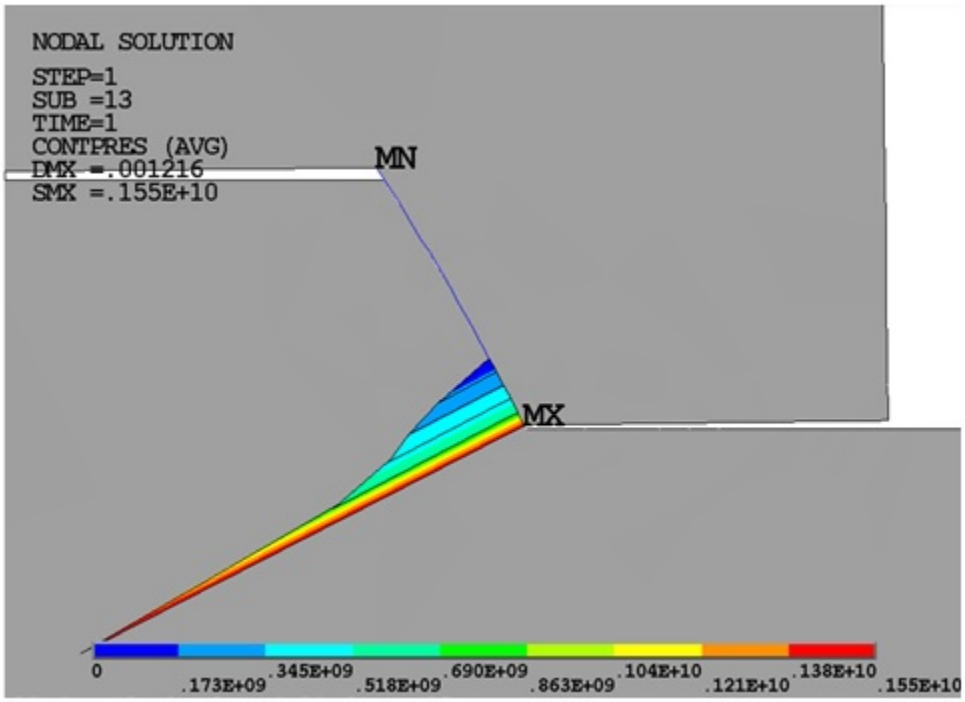

Figure 4-50. 30° rotor and 29° collar contact pressure at 0 rpm

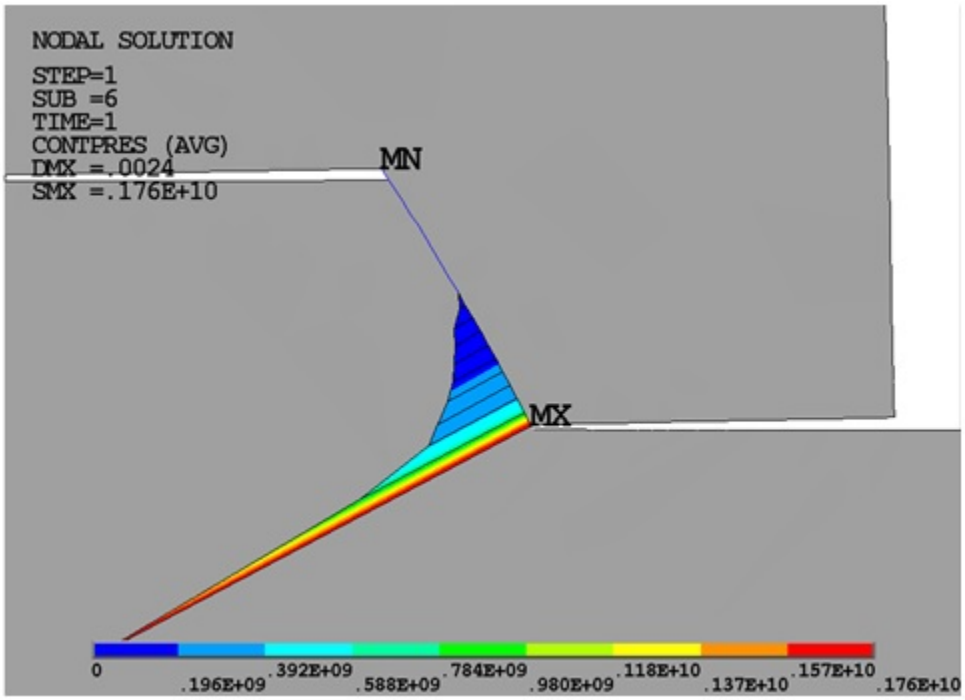

Figure 4-51. 30° rotor and 29° collar contact pressure at 12000 rpm

Further simulations are run for this particular model up to 14000 rpm. Results show the contact area continues to increase with an increase in speed. At 14000 rpm the contact exists across the entire taper. However operating at this speed causes failure in both the flywheel and the collar with the larger failure area occurring in the collar. Figure 4-52 plots the Von Mises stress of the collar and shows a similar failure area as in previous models. The stresses in the upper section of the taper remain below the UTS. Since the lower section undergoes the largest interference, it is the first area of failure while near the center it occurs due to the bending of the collar.

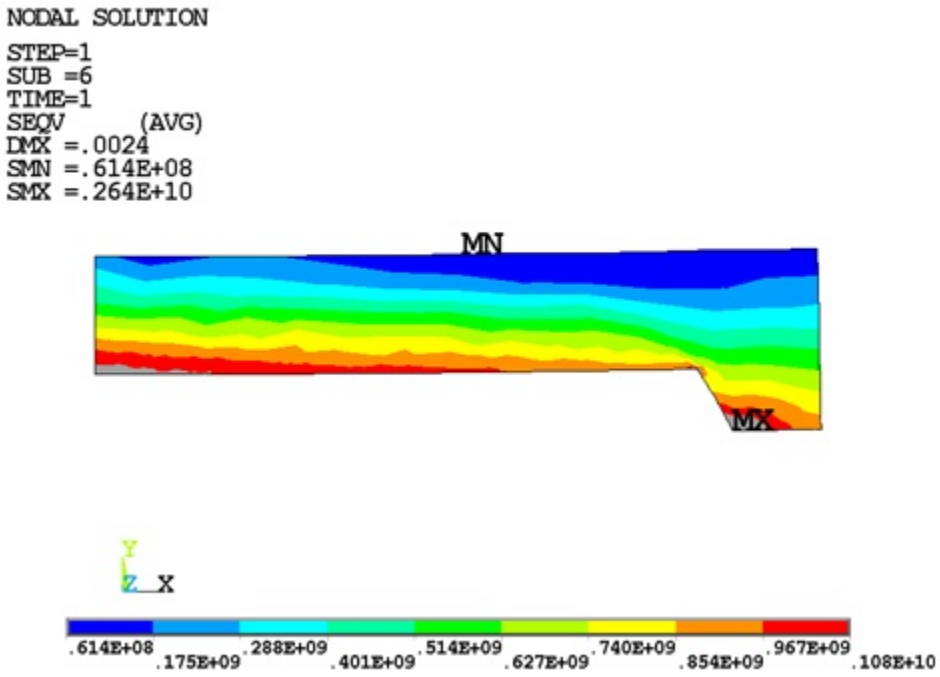

Figure 4-52. Collar Von Mises stress

4.9 Curved 0° Rotor 1° Collar

By combining the angle variation of the rotor and collar and the curved taper, it is found that a model with a 0° rotor and a 1° collar provides the maximum amount of compression to the rotor. One modification made to current model consists of applying curves to the tapers in order to reduce the high stresses that occur at the corners. Figure 4-53 shows the resulting contact pressure at 0 rpm. As seen in the figure, the compression appears to be evenly distributed throughout the center of the taper area with the maximum value being 70.3 MPa.

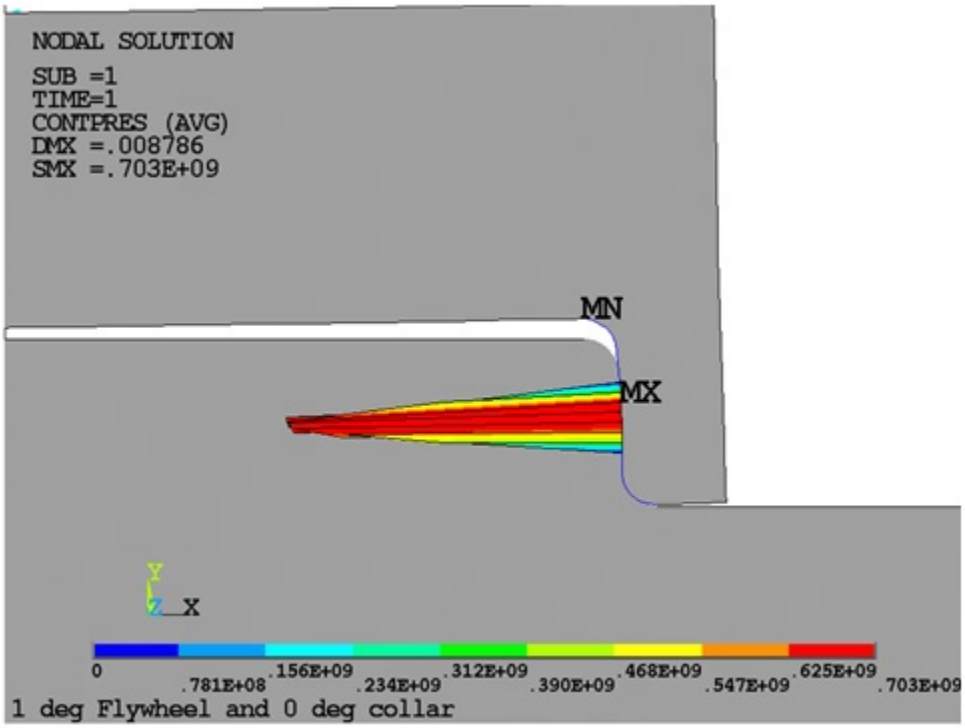

Figure 4-53. 0° Rotor 1° Collar contact pressure at 0 rpm

At 12000 rpm, the stresses in the rotor area at or below 1080 MPa. However the interfering section of the collar appears to fail as seen in Figs. 4-54 and 4-55. Increasing the interference lowers the stresses in the rotor but causes the collar to fail at lower speeds due to the increase in initial tensile stress. In order to lower the stresses in the collar, various modifications are applied. By lowering the stresses in the collar, it is expected for there to be an increase in the allowable interference and speed.

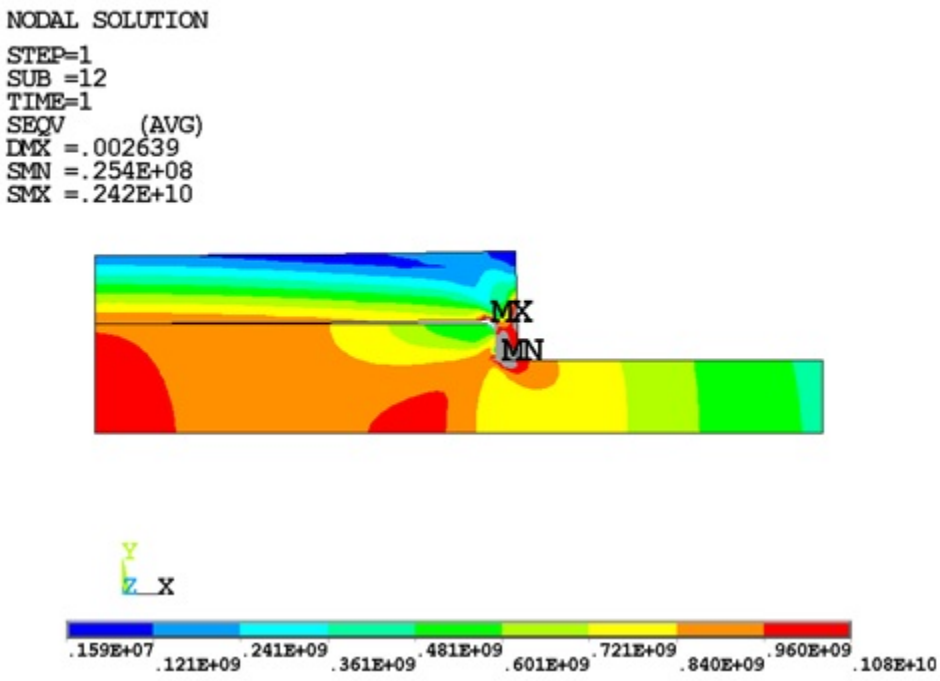

Figure 4-54. 0° Rotor 1° Collar Von Mises stress at 12000 rpm

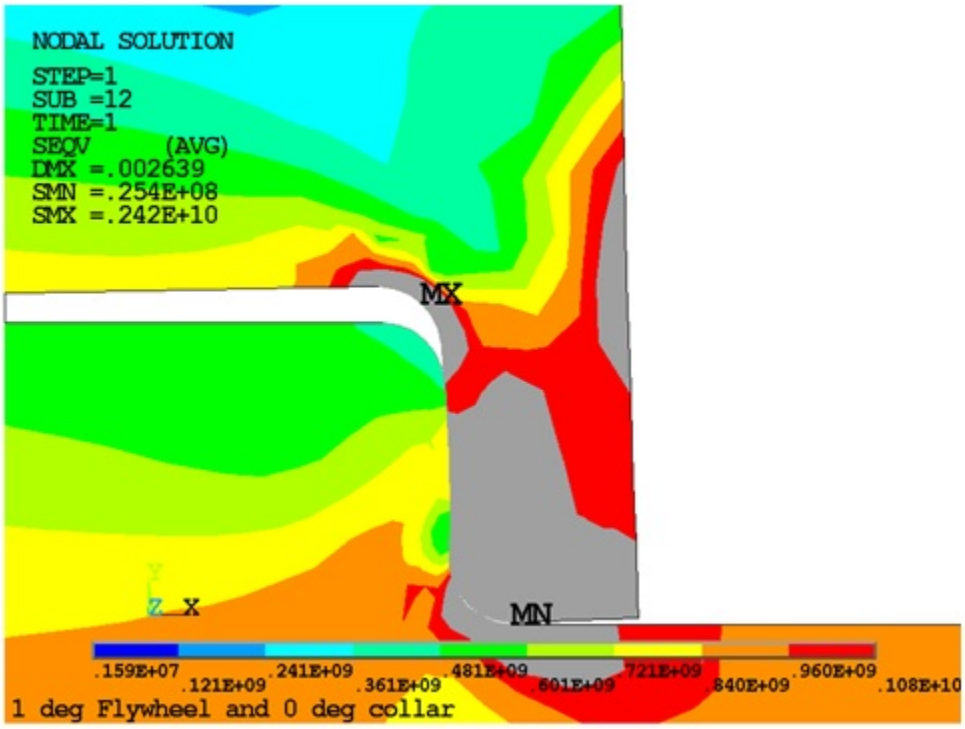

Figure 4-55. 1° Collar Von Mises stress at 12000 rpm

4.9.1 Collar Modifications

The first modification applied to the collar is an increase in the thickness from 125 mm to 150 mm. An increase in thickness is expected to lead to lower the stress due to the availability of the extra material for its distribution. The Von Mises stress plot in Fig. 4-56 shows a similar stress profile and area of failure as the standard collar.

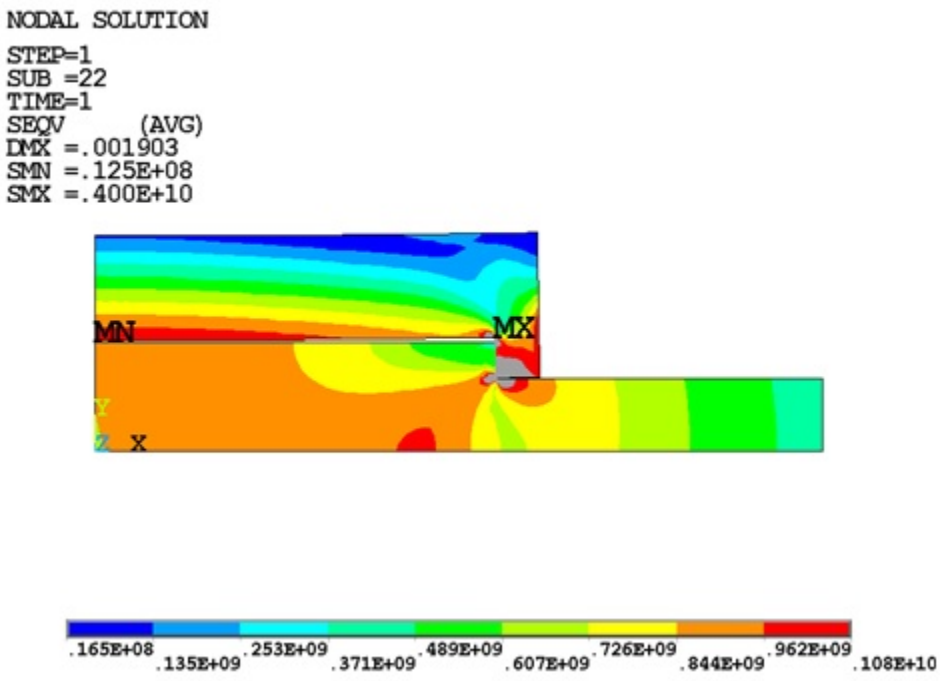

Figure 4-56. 0° Rotor 1° Collar increased thickness Von Mises stress at 12000 rpm

A further modification made to the collar is reducing the thickness of the interfering area by half. It is expected for the stresses to decrease due to the reduced outer radius of the rim. Figure 4-57 plots the resulting Von Mises stress. From the figure, it is evident the reduced radius of the collar causes a greater area of failure due to the loss of material. The collar also fails near the inner radius due to the increased bending that occurs from the interference.

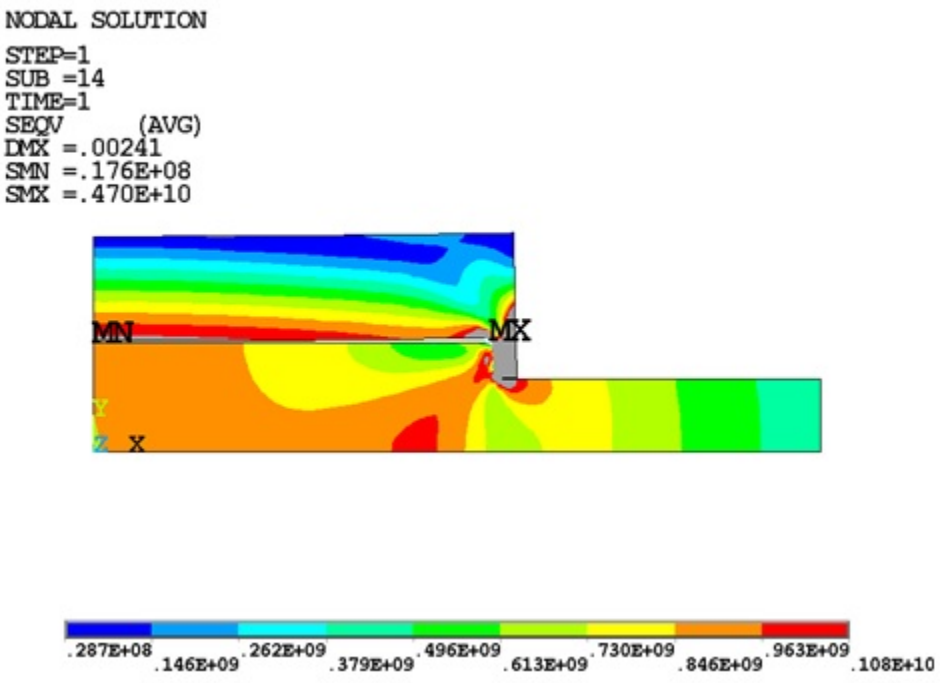

Figure 4-57. 0° Rotor 1° Collar half flange increased thickness Von Mises stress at 12000 rpm

For the proceeding simulation, the thickness of the collar was maintained at 150 mm while the flange area was doubled from the standard collar. With the additional material, it is expected for the magnitudes of the stress in the interfering area to decrease. Figure 4-58 plots the Von Mises stress of the rotor and collar at 12000 rpm. The figure shows the rotor stresses at or below 1080 MPa with the exception of the transition corner. Stresses in the collar show that the increased radius of the collar leads to lower stresses in the interfering area but higher stresses throughout the inner radius. An increase in the thickness of the collar does not have an advantageous effect on the stresses. Variation of the radius results in an inverse relationship between the stresses near the inner radius of the collar and the interfering surface.

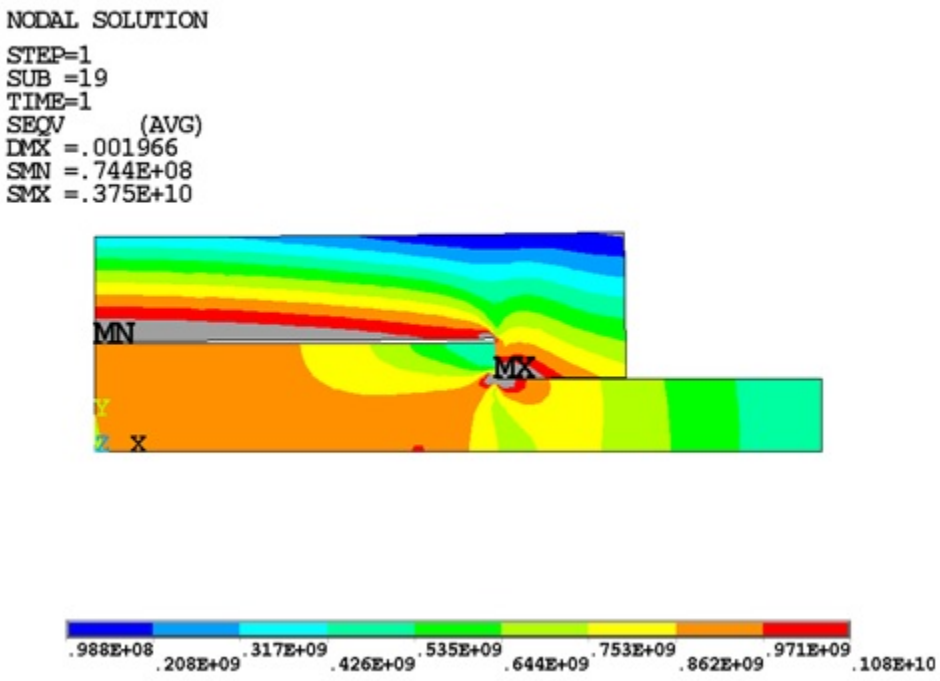

Figure 4-58. 0° Rotor 1° Collar doubled flange thickness Von Mises stress at 12000 rpm

4.10 Full Diameter Rim

Previous simulations show that a collar with interference undergoes the highest stresses in a flywheel configuration. A material with a high UTS is needed to prevent failure in the collar during high speed operation. Figure 4-59 shows the results for the rotor with an Aermet rim Von Mises stress at 13000 rpm with a 1 mm interference. Both the rotor and rim fail. The plot shows a loss of interference caused by the bending of the rim. The angular velocity is reduced to 12000 rpm to determine the resulting effect on the contact pressure and the stresses. At 12000 rpm, there is still a loss of interference and failure in both the rotor and collar. The results show that implementing a rotor spanning the entire diameter of a flywheel leads to loss in interference and failure in the rim.

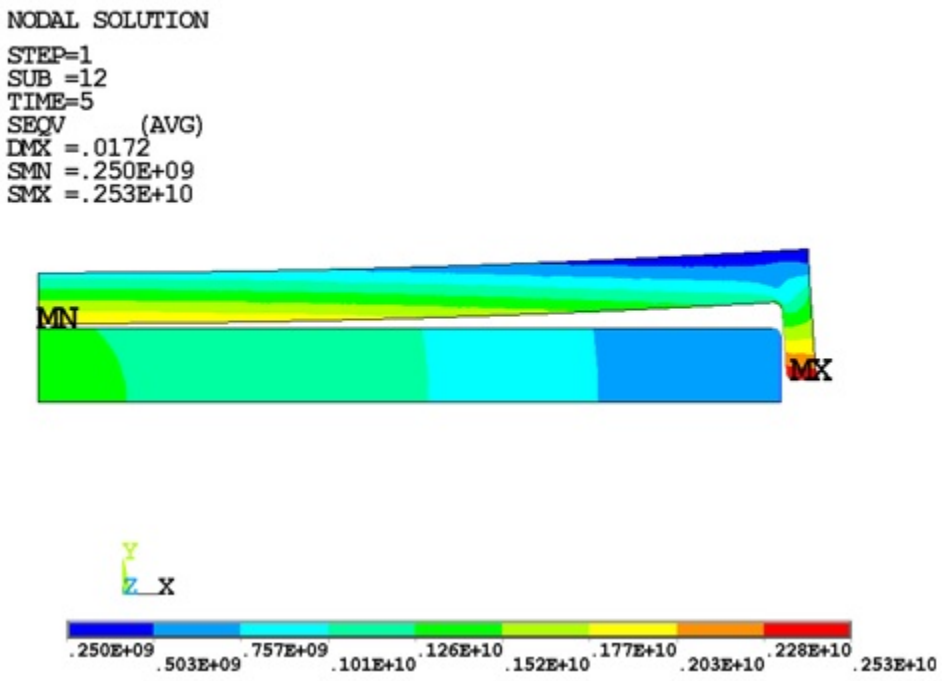

Figure 4-59. Rotor with Aermet rim Von Mises stress at 12000 rpm

4.11 Energy Storage Comparisons

A comparison of the energy densities between the various flywheel modifications is made to determine the overall success of each model. The energy and energy densities are listed in Table 4-3 along with the speed, mass, pressure (if applicable) and maximum Von Mises stress. The mass based and volume based energy density for the standard flywheel is 23.04 W*h/kg and 180876.4 W*h/m^3 respectively.

Table 4-3. Energy density table.

Description	Speed (rpm)	Mass (kg)	Pressure (MPa)	VMmax (MPa)	E (W*h)	E/m (W*h/kg)	E/V (W*h/m^3)
Basic Model	11000	616	0	1080	14206	23.04	181034
0.15 m Thickness	11000	925	0	1080	21308	23.04	180830
Hybrid Flywheel	11500	569	—	1060	12674	22.29	161370
Composite	11000	124	—	—	4630	37.31	58951
Linear Taper	11500	771	0	1060	19394	25.15	197461
0° Transition	12000	693	0	1020	17414	25.11	197258
0° Transition	12000	693	750	973	17414	25.11	197258
0° Transition	12500	693	1000	1090	18913	27.27	214238
Rotor with Collar	12000	949	—	1080	12400	13.1	102568

A study is conducted to determine the effect that the variation of the diameter of a solid steel disk has on both the specific energy and energy density. The flywheel has a thickness of 12.7 cm where the diameter is varied from 1.27 to 3.81 m with a Von Mises stress of 1.03 GPa. Figure 4-60 shows the results for both the specific energy and energy density for the different sized flywheels. The figure shows interesting results. While the energy density increases with the diameter, the specific energy remains constant throughout. This suggests that the specific energy is inherent to the system and the only manner to increase it is to use a material with a higher strength. The energy density plot shows a parabolic increase with an increase in flywheel diameter. If available space and cost are not a factor in the construction of a flywheel, building a large flywheel as possible results in a high energy density.

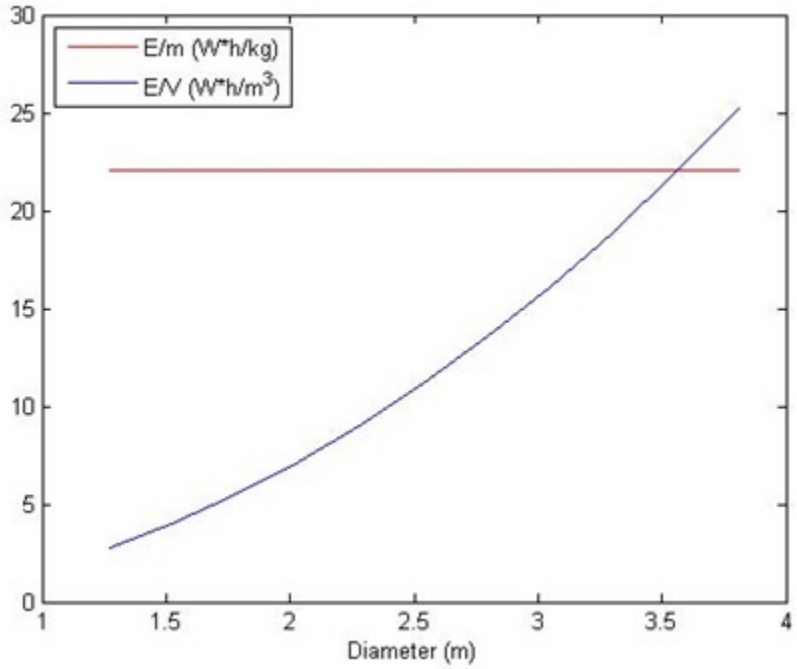

Figure 4-60. Specific energy and energy density vs flywheel diameter

Figure 4-61 plots the results for the allowable speed of the flywheel with respect to its diameter. It is shown that the larger diameter of the flywheel is the lower the allowable operating speed. This can be attributed to increase that occurs in the stresses throughout the flywheel with an increase in the diameter.

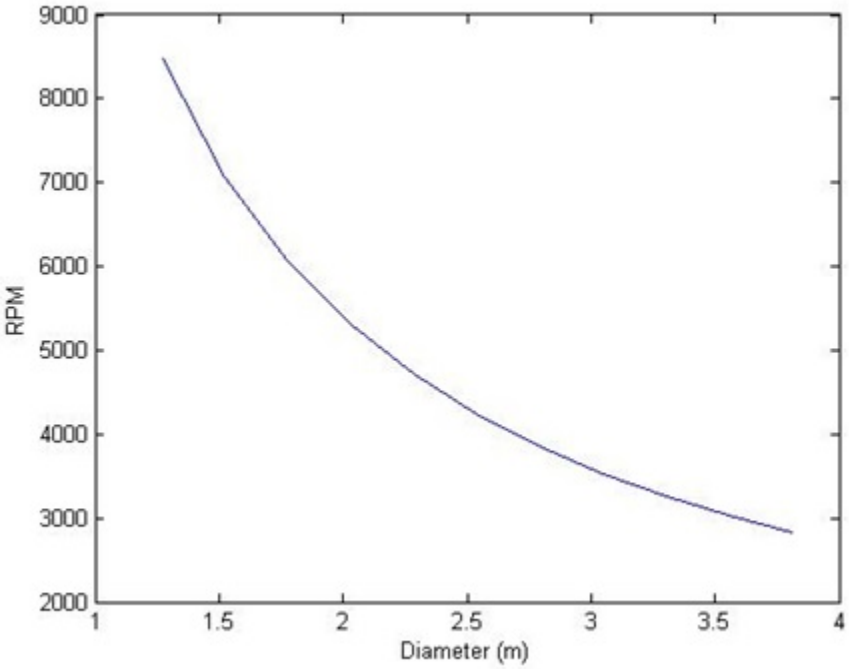

Figure 4-61. Allowable speed vs flywheel diameter

5. CONCLUSION AND FUTURE WORK

5.1 Conclusion

The primary objective of this thesis was to analyze the specific energy and energy density of various flywheels in order to increase the amount of storable energy by utilizing past and current materials and unique designs.

The following tasks have been accomplished:

- Unique designs were applied to steel flywheels that induced compression thereby reducing tensile stresses caused by high speed operation.
- Specific energy and energy density comparison was performed between steel and composite flywheels.
- Filament wound composite rim were modeled successfully through ANSYS and compared with analytical solutions.

The main problem encountered throughout modeling of the compressive designs for steel flywheels are the high stresses caused by the interference and tensile stresses during operation. Designs in which pressure is applied to a steel flywheel causes stress concentrations that increase in magnitude as the operating speed increases. It is shown in the simulations the optimum area to apply pressure is near the center of the flywheel for maximum compression. It is also important to apply a smooth transition and avoid sharp corners to reduce concentrated stresses in the flywheel. Collar stress concentrations can mainly be attributed to upward bending moment present in many of the simulations which is produced by both the high speed rotation and slippage from the rotor. In order for the current alternative compressive designs to prove viable, a stronger material would be needed than is currently available. Further

improvements to the geometry of flywheel may lead to successful increases in specific energy and energy density capabilities. The multiple concentric rim method of construction for composite materials does not appear to be as advantageous for isotropic materials due to the resulting high tensile stresses in the tangential direction.

For a solid steel flywheel increasing the diameter has no effect on the specific energy of the system unlike the energy density which increases quadratically. The maximum operating speed based on the allowable Von Mises stress of the flywheel decreases quadratically with an increase in diameter. It appears that scaling a specific flywheel geometry will have no effect on the total specific energy. This allows for greater freedom in optimizing the flywheel based on the available space for the system and retain a required specific energy.

From the energy table used for comparison of flywheel designs, several interesting conclusions are clear. It is evident variations in flywheel geometry can lead to higher specific energy and energy density. Both the flywheel with a linear taper and step transition have similar specific energies and energy densities. Shape optimization of steel flywheels is a simpler manner to increase the storable energy without including multiple parts. However construction of the flywheel (i.e. machining costs) may prove less economically feasible depending on the required geometry. It is clear a solid composite flywheel with similar dimensions as a steel flywheel will have a lower energy. However the specific energy of the composite flywheel is larger compared to a steel construction. In order to surpass the energy of the composite flywheel either the mass or operating speed must be increased. The current flywheel design does not allow for much improvement in either category. Optimization of the design is required to match current composite flywheel energy claims and requirements.

In summary, the findings of this study provide alternate flywheel designs to current steel flywheels with the intent of increasing the specific energy and energy den-

sity. This study may ultimately contribute to development of steel flyhweels with energy storage capabilities similar to that of composite flywheels leading to cheaper energy storage methods due to the reduced cost of the material.

5.2 Future Work

Continuing work will continue to focus both on composite and steel flywheels. Composite flywheel analysis will further explore their capacity for high energy storage. The following courses of further action include:

- Application of a constant strain as opposed to a constant interference between composite rims.
- Design and analysis of a multimaterial thick rim with a ballasted E-glass inner rim and Kevlar or carbon fiber outer rim.
- Analyze flywheels constructed with various fiber composite materials.
- Apply other failure criterion for composites for comparison.
- Shape optimization of steel flywheels from literature.

REFERENCES

[1] Ruddell, A. J., 2003. "Storage and Fuel Cells". EPSRC SuperGen Workshop: Future Technologies for a Sustainable Electricity System, University of Cambridge, Cambridge, UK.

[2] Anonymous, 2003. Emerging Energy Storage Technoligies in Europe. Tech. rep., Rapport Frost & Sullivan, London, UK.

[3] Anonymous, 2002. "Proceedings of the International Conference of Electrical Energy Storage Systems: Applications and Technologies". International Conference Electrical Energy Storage Systems, Vol. 323, EESAT.

[4] Grubler, M., 1906. "Ring Spannung and Zugfestigkeit". *ZDV Deutsch, Ing,* **50**.

[5] Donath, M., 1912. *Die Berechnung Rotierender Scheiben und Ringe: Nach Einem Neuen Verfahren.* Springer, New York City, NY.

[6] Stodola, A., 1945. *Steam and Gas Turbines.* Peter Smith, Gloucester, MA.

[7] Genta, G., 1985. *Kinetic Energy Storage: Theory and Practice of Advanced Flywheel Systems.* Butterworths, Oxford, UK.

[8] Kress, G., 2000. "Shape Optimization of a Flywheel". *Structural and Multidisciplinary Optimization,* **19**(1), pp. 74–81.

[9] van Rensburg, P. J., 2011. "Energy Storage in Composite Flywheel Rotors". Master's thesis, Stellenbosch University, Stellenbosch, ZA.

[10] Tzeng, J., Emerson, R., and Moy, P., 2006. "Composite Flywheels for Energy Storage". *Composites Science and Technology,* **66**(14), pp. 2520–2527.

[11] Ha, S. K., Han, H. H., and Han, Y. H., 2008. "Design and Manufacture of a Composite Flywheel Press-fit Multi-rim Rotor". *Journal of Reinforced Plastics and Composites,* **27**(9), pp. 953–965.

[12] Pardoen, G. C., Nudenberg, R. D., and Swartout, B. E., 1981. "Achieving Desirable Stress States in Thick Rim Rotating Disks". *International Journal of Mechanical Sciences,* **23**(6), pp. 367–382.

[13] Danfelt, E. L., Hewes, S. A., and Chou, T.W., 1977. "Optimization of Composite Flywheel Design". *International Journal of Mechanical Sciences,* **19**(2), pp. 69–78.

[14] Portnov, G., Bakis, C., and Emerson, R., 2004. "Some Aspects of Designing Multi-rim Composite Flywheels". *Mechanics of Composite Materials,* **40**(5), pp. 397–408.

[15] Bolund, B., Bernhoff, H., and Leijon, M., 2007. "Flywheel Energy and Power Storage Systems". *Renewable and Sustainable Energy Reviews,* **11**(2), pp. 235–258.

[16] Hartog, J. D., 1952. *Advanced Strength of Materials.* McGraw-Hill, NY.

[17] Hamrock, B. J., Jacobson, B. O., and Schmid, S. R., 1999. *Fundamentals of Machine Elements.* WCB/McGraw-Hill, Boston, MA. ID: 156930293.

[18] Wang, Z., 2011. "A Novel Flywheel and Operation Approach for Energy Recovery and Storage". PhD thesis, Texas A&M University, College Station, TX.

[19] Arnold, S., and Kruch, S., 1991. Differential Continuum Damage Mechanics Models for Creep and Fatigue of Unidirectional Metal-matrix Composites. Tech. rep., National Aeronautics and Space Administration Lewis Research Center, Cleveland, OH.

[20] Barbero, E. J., 2011. *Introduction to Composite Materials Design*. CRC Press, Boca Raton, FL.

APPENDIX

Ansys Mechanical APDL Input Files

```
FINISH
/CLEAR
/TITLE,Solid Steel Wheel
/PREP7
ET,1,PLANE182,,,1
TYPE,1
!!! Material Properties
! Steel
MP,EX,1,200e9
MP,PRXY,1,0.3
MP,DENS,1,7850
! Flywheel keypoints
K,1,0,0,0
K,2,0.5,0,0
K,3,0.5,0.05,0
K,4,0,0.05,0
!Create lines
L,1,2
L,2,3
L,3,4
L,4,1
ALLSEL
! Create areas
AL,1,2,3,4
ALLSEL
AATT,1,1,1
```

```
ALLSEL
! Mesh
SMRTSIZE,6
AMESH,ALL
AREF,ALL,,,2
ALLSEL
FINISH
/SOLU
!Solution settings
NLGEOM,ON
NSUBST,10,0,0
DK,1,UY,0,,0
!Apply angular velocity
OMEGA,0,1152,0
SOLVE
FINISH
```

```
FINISH
/CLEAR
/TITLE,Steel wheel with 1steel rim
/PREP7
ET,1,PLANE182,,,1
TYPE,1
ET,2,TARGE169
ET,3,CONTA171
KEYOPT,3,10,2
!!! Material Properties
! Steel
MP,EX,1,200e9
MP,PRXY,1,0.3
MP,DENS,1,7850
! Flywheel keypoints
K,1,0,0,0
K,2,0.4,0,0
K,3,0.4,0.05,0
K,4,0,0.05,0
! Rim keypoints
K,5,0.399,0,0
K,6,0.5,0,0
K,7,0.5,0.05,0
K,8,0.399,0.05,0
L,1,2
L,2,3
```

```
L,3,4
L,4,1
L,5,6
L,6,7
L,7,8
L,8,5
ALLSEL
! Create areas
AL,1,2,3,4
AL,5,6,7,8
ALLSEL
AATT,1,1,1
ALLSEL
! Mesh
SMRTSIZE,6
AMESH,ALL
AREF,ALL,,,2
! Generate the target surface
LSEL,S,,,2
NSLL,S,1
TYPE,2
REAL,1
ESURF
! Generate the contact surface
LSEL,S,,,8
NSLL,S,1
```

TYPE,3

REAL,1

ESURF

ALLSEL

FINISH

/SOLU

!Solution settings

NLGEOM,ON

NSUBST,10,0,0

DK,1,UY,0,,0

!Apply angular velocity

OMEGA,0,500,0

SOLVE

FINISH

```
FINISH
/CLEAR
/TITLE,Welded flywheel with internal press fit
/PREP7
ET,1,PLANE182,,,1
!!! Material Properties
! Steel
MP,EX,1,200e9
MP,PRXY,1,0.3
MP,DENS,1,7850
!!! Create keypoints
! Flywheel keypoints
K,1,0,0,0
K,2,0.375,0,0
K,3,0.4,0.025,0
K,4,0.4,0.075,0
K,5,0.375,0.1,0
K,6,0,0.1,0
! Rim keypoints
K,7,0.398,0.025,0
K,8,0.425,0.025,0
K,9,0.45,0,0
K,10,0.5,0,0
K,11,0.5,0.1,0
K,12,0.45,0.1,0
K,13,0.425,0.075,0
```

```
K,14,0.398,0.075,0
! Top weld keypoints
K,15,0.4,0.075,0
K,16,0.425,0.075,0
K,17,0.45,0.1,0
K,18,0.375,0.1,0
! Bottom weld keypoints
K,19,0.4,0.025,0
K,20,0.425,0.025,0
K,21,0.45,0,0
K,22,0.375,0,0
!!! Create areas
! Flywheel
A,1,2,3,4,5,6
! Rim
A,7,8,9,10,11,12,13,14
! Top weld
A,15,16,17,18
! Bottom weld
A,19,20,21,22
ASEL,S,AREA,,ALL
AATT,1,1,1
ALLSEL
! Mesh
SMRTSIZE,5
AMESH,ALL
```

```
FINISH
/SOLU
!Solution settings
NLGEOM,ON
NSUBST,5,0,0
DL,1,1,UY,0
!Apply angular velocity
OMEGA,0,1152,0
SOLVE
FINISH
```